PolyPublie
Polytechnique Montréal

POLYTECHNIQUE MONTRÉAL
UNIVERSITÉ D'INGÉNIERIE

Titre: Title:	Propriétés optiques des nano-trous périodiques dans une couche mince métallique : modélisation, fabrication et application comme biocapteur
Auteur: Author:	André-Pierre Blanchard-Dionne
Date:	2017
Type:	Mémoire ou thèse / Dissertation or Thesis
Référence: Citation:	Blanchard-Dionne, A.-P. (2017). Propriétés optiques des nano-trous périodiques dans une couche mince métallique : modélisation, fabrication et application comme biocapteur [Thèse de doctorat, École Polytechnique de Montréal]. PolyPublie. https://publications.polymtl.ca/2817/

Document en libre accès dans PolyPublie
Open Access document in PolyPublie

URL de PolyPublie: PolyPublie URL:	https://publications.polymtl.ca/2817/
Directeurs de recherche: Advisors:	Michel Meunier
Programme: Program:	Génie physique

Ce fichier a été téléchargé à partir de PolyPublie, le dépôt institutionnel de Polytechnique Montréal
This file has been downloaded from PolyPublie, the institutional repository of Polytechnique Montréal

https://publications.polymtl.ca

UNIVERSITÉ DE MONTRÉAL

PROPRIÉTÉS OPTIQUES DES NANO-TROUS PÉRIODIQUES DANS UNE COUCHE MINCE MÉTALLIQUE : MODÉLISATION, FABRICATION ET APPLICATION COMME BIOCAPTEUR

ANDRÉ-PIERRE BLANCHARD-DIONNE
DÉPARTEMENT DE GÉNIE PHYSIQUE
ÉCOLE POLYTECHNIQUE DE MONTRÉAL

THÈSE PRÉSENTÉE EN VUE DE L'OBTENTION
DU DIPLÔME DE PHILOSOPHIÆ DOCTOR
(GÉNIE PHYSIQUE)
OCTOBRE 2017

© André-Pierre Blanchard-Dionne, 2017.

UNIVERSITÉ DE MONTRÉAL

ÉCOLE POLYTECHNIQUE DE MONTRÉAL

Cette thèse intitulée :

PROPRIÉTÉS OPTIQUES DES NANO-TROUS PÉRIODIQUES DANS UNE COUCHE MINCE MÉTALLIQUE : MODÉLISATION, FABRICATION ET APPLICATION COMME BIOCAPTEUR

présentée par : BLANCHARD-DIONNE André-Pierre
en vue de l'obtention du diplôme de : Philosophiæ Doctor
a été dûment acceptée par le jury d'examen constitué de :

M. PETER Yves-Alain, D. Sc., président
M. MEUNIER Michel, Ph. D., membre et directeur de recherche
M. GODBOUT Nicolas, Ph. D., membre
M. CHARETTE Paul, Ph. D., membre externe

DÉDICACE

À mes parents,
Georges Dionne et Danielle Blanchard

REMERCIEMENTS

J'aimerais d'abord remercier mes collègues du groupe de recherche LP^2L, à commencer par ceux du groupe de plasmonique Mathieu Maisonneuve, Anne-Marie Dallaire, Olivier d'Allivy-Kelly, Laurent Guyot, Vincent Latendresse, Laurent Doré-Mathieu, Sergiy Patskovsky et ceux du groupe laser Nicolas Le Hir, Adrien Dagallier, Bastien St-Louis, Étienne Boulais David Rioux, Sébastien Besner. Les gens du Laboratoire de MicroFabrication Marie-Hélène Bernier, Alireza Hajhosseini-Mesgar et Christophe Clément. Notre super technicien Yves Drolet. Les stagiaires qui m'ont aidé Alexia Bouchard Saindon, Francis Marcogliese et Éric Bridet. Aux professeurs avec qui j'ai collaboré Yves-Alain Peter, Maksim Skorobogatiy et Oussama Moutanabir. Aux professeurs et étudiants du réseaux Biopsys du CRSNG avec qui j'ai collaboré Reuven Gordon, Alex Brolo, Pierre Berini, Chiara Valsecchi. Merci à ma blonde Catherine Ouellet-Dupuis. Merci aux membres de ma famille Jean-Francois, Anne-Pier, Noah, Mila et Zoé. Et bien sur à mon superviseur de thèse Michel Meunier !

RÉSUMÉ

Dans cette thèse de doctorat, les réseaux de nano-trous périodiques dans des films métalliques sont étudiés. Leurs dimensions sont de l'ordre de la centaine de nanomètres, autant pour la taille du trou que l'espacement entre chacun et l'épaisseur du film. Ils possèdent des propriétés optiques remarquables : à certaines longueurs d'onde, la lumière qui diffracte à la surface de cette structure peut se coupler avec l'onde de propagation à l'intérieur du trou. Lorsque ces conditions sont rencontrées, un phénomène de résonance est excité et une forte transmission optique est observée de l'autre côté du film. On parle alors de transmission optique extraordinaire ou EOT pour "Extraordinary Optical Transmission". Le terme extraordinaire provient du fait que, si on considère la transmission optique des trous individuellement, l'intensité observée serait plusieurs ordres de grandeur inférieure à celle mesurée pour le réseau. De plus, même si on réunissait tout les trous en un seul grand trou (avec les proportions avec la partie métallique conservée), la transmission optique serait encore inférieure à celle observée pour le réseau. Le réseau possède donc la propriété de canaliser la lumière vers les indentations et ainsi de concentrer l'onde électromagnétique vers l'intérieur de l'indentation. Ces structures permettent de manipuler la lumière à l'échelle du nanomètre et ainsi de construire des matériaux avec des propriétés optiques remarquables.

Dans une première partie de cette étude de ces structures, la modélisation des propriétés optiques est abordée en utilisant la théorie des modes couplés ou CMT pour "Coupled Mode Theory". Cette méthode consiste en une expansion des champs électromagnétiques des modes possibles dans chacun des milieux de la structure ainsi qu'un calcul des coefficients de couplages de l'onde d'un milieu à l'autre. Bien que d'autres méthodes de modélisation analytique existent, la CMT a été choisie car elle permet de minimiser les approximations employées dans la modélisation, tout en offrant un développement analytique typique des problèmes de transmission optique. De plus, sous certaines approximations, la méthode permet d'écrire les équations sous une forme simple qui décrit directement l'origine de la résonance. Une compréhension approfondie des mécanismes en jeu de la transmission optique est donc obtenue grâce à cette modélisation.

Dans le cadre de ce travail de modélisation, une contribution originale a été effectuée afin d'approfondir la méthode lorsque l'on considère plusieurs modes possibles à l'intérieur des indentations. Effectivement, uniquement des approches approximatives sont disponibles dans la littérature, ou des approches utilisant uniquement le mode fondamental guidé à l'intérieur du trou, qui sont des approximations valides uniquement dans le cas sous-longueur d'onde ou

dans le cas de petites indentations. Un système matriciel a donc été mis en place afin de relever la contribution de chaque mode ainsi que le couplage d'un mode à l'autre. Cette méthode a été présentée dans le papier "Optical transmission theory for metal-insulator metal periodic nanostructures". La méthode a été démontrée pour un réseau périodique plus complexe en 3 couches métal-diélectrique-métal afin de démontrer l'utilité et l'étendue de la méthode.

Puisque l'objectif de ce travail de doctorat est d'utiliser ces structures afin de développer des biocapteurs optiques, l'utilisation de la méthode de modélisation a été mise de l'avant afin de déterminer leur potentiel comme biocapteur. Généralement, les papiers de littérature utilisent l'équation de résonance des plasmons de surface (ou SPP) afin d'expliquer le phénomène et afin de calculer la sensibilité théorique ainsi que la distribution de champs électromagnétiques. Le phénomène de résonance avec les réseaux de nano-trous fait effectivement intervenir des ondes de surface, mais le mécanisme de résonance est plus complexe et plus subtil. Il n'est donc pas juste d'utiliser l'équation des SPPs. Puisqu'il n'existait aucune référence valable faisant une étude de l'utilisation des nano-trous comme biocapteurs d'un point de vue théorique, un article de revue ainsi qu'un tutoriel sur la modélisation et son utilisation pour déterminer les performances pour la biodétection a donc été réalisé. Une analyse en détail des effets de chaque paramètre ainsi qu'une optimisation du design sont présentés également dans cet article intitulé "Sensing with periodic nanohole array".

En terme de réalisation expérimentale, nous débutons la présentation des travaux effectués dans un chapitre dédié à la nanofabrication des réseaux périodiques. Il s'agit de la partie la plus difficile à mettre en place et qui est essentielle pour mettre en place un capteur fiable et précis. Un bref survol des techniques de fabrication rencontrées dans la littérature est présenté dans le chapitre "Approche et justification de la méthode". Ensuite, une contribution originale est présentée. Il s'agit d'une méthode de lithographie par faisceau d'électrons sur une bi-couche de résine négative afin d'obtenir la structure désirée par la technique de "lift-off". Cette méthode possède l'originalité d'être une des seules méthodes mises en place pour les lift-offs avec résine négative et utilise une résine conventionnelle, soit la PMMA.

Finalement, la réalisation expérimentale de biodétection à l'aide des nanostructures est présenté dans les derniers chapitres. Les projets réalisés portent sur l'optimisation des performances de ce type de capteur. En effet, bien que ces capteurs mettent de l'avant des avantages considérables pour le développement de biocapteurs au niveau du multiplexage et de la miniaturisation, ceux-ci offrent des performances de biodétection bien en deça des biocapteurs SPR reposant sur la configuration Kretchmann. Les projets s'attardent donc à développer des stratégies afin d'améliorer les performances de ces capteurs d'un point de vue de l'ingénierie. Dans un premier temps la nature bidimensionnelle des capteurs est exploitée afin d'effectuer

une méthode auto-référencée de détection du signal basée sur le signal de chacune des polarisations. En effet, la structure proposée possède des périodes différentes dans les directions -x et -y. Un changement d'indice de réfraction résulte en une augmentation de signal pour une polarisation et une diminution pour l'autre. La détection balancée entre les deux signaux permet donc de doubler la sensibilité du capteur et permet une nette diminution du bruit grâce à l'auto-référencement des signaux de détection.

Bien que cette méthode présentait de bons avantages au niveau de la performance du capteur, sa mise en place pour une détection multiplexée n'était pas optimale. Une autre structure fut donc mise de l'avant. Il s'agit d'un réseau multipériodique de nanotrous : chaque rangée de trous possède une période différente, qui va en augmentant. Cette structure permet d'effectuer un scan du vecteur d'onde de l'onde diffractée et permet donc une détection basée sur la position du maxima du pic de résonance. Elle permet également une meilleure précision du capteur comparativement aux capteurs qui se basent uniquement sur le signal d'intensité d'une seule période et qui sont donc assujettis à des sources de bruit parasites, tel le bruit de la source ou le signal de contaminants. Elle permet de conserver un montage optique simple qui ne se base pas sur un monochromateur et qui permet donc une fréquence d'acquisition bien supérieure, ce qui est essentiel pour effectuer le multiplexage.

ABSTRACT

In this Ph.D thesis, periodic nanohole arrays built in metallic films are studied. These arrays consist in an arrangement of holes, spaced apart periodically, in thin metallic films. The structures are all of the order of the nanometer. These structures have extraordinary optical properties : for certain wavelengths, light can diffract at the surface of the metal and couple to the propagation wave inside the holes. When these conditions are met, a resonant phenomenon is excited and a strong transmission is observed. This phenomenon was termed extraordinary optical transmission or EOT. The term extraordinary comes from the fact that, if we consider the transmission of the sum of the isolated holes, the transmitted intensity would be orders of magnitude lower than the one observed from the array configuration. Furthermore, even if we were to assemble all the holes in one big hole (with hole/metal ratio conserved), the optical transmission would still be lower. These structure have the capacity to channel light inside the holes and concentrate electromagnetic radiation at the surface. They can thus manipulate light at the nanoscale level to create optical components with remarkable properties.

In the first part of this thesis dedicated to the study of these structures, modelling of the optical properties of these structures is presented, using the method of Coupled Mode Theory (CMT). This method consists in an expansion of the electromagnetic fields in modes in the different regions of the structure and in a calculation of the coupling coefficients of the modes from one region to another. This method has several advantages compared to other methods, namely that is can minimize the approximations used, while offering an analytical development typical of problems in optics. Furthermore, under certain approximations, the method can describe the equations under a simple form which highlights the origin of the resonance. A deeper understanding of the mechanism involve in the resonance property of these structures can thus be achieved.

One of the original contribution of this thesis was made in order to develop further the understanding of this method. Indeed, when considering the region inside the holes, most articles in the literature use only the fundamental mode. This approximation is good in the subwavelength case and for holes of small dimension, but becomes imprecise otherwise. Since the interesting dimensions of nanohole arrays for sensing might make use of all dimensions it was important to use a more complete model. A matrix formalism has thus been written in order to assess the contribution of each mode and the coupling of the modes between them. This method was presented in the paper entitled "Optical transmission theory for

metal-insulator-metal periodic nanostructures". It was done for a more complex structure of 3 layers in a metal-dielectric-metal structure in order to demonstrate the utility of the method.

Since the objective of this thesis is to use the structures as optical biosensors, the model was used in order to evaluate the overall potential of these arrays for sensing. Most papers in the literature quote the surface plasmon resonance (SPP) relation in order to describe the properties of the array or the field distribution, which is incorrect. The resonance phenomenon in nanohole arrays is more complex and more subtle. Since no article was available on the theoretical study of the potential of these structure for sensing, a review article and tutorial on the modelling method was written. A detailed analysis of the effect of each parameters as well as an optimization of the design is also presented in the article entitled "Sensing with Periodic Nanohole Array".

In terms of experimental realizations, we begin the presentation of the work in a chapter dedicated to the fabrication methods of nanohole array. It is the most unique aspect of fabrication and is essential to conceive a reliable sensor. A brief overview of the different fabrication techniques is presented. It is followed by an original contribution of the fabrication technique based on electron beam lithography on a negative bilayer resist for lift-off.

Finally, the experimental achievement of biosensing with nanohole arrays is presented. The two projects presented have to do with improving experimental methods for the performance and the reliability of the sensor. Indeed, nanohole array sensors offer great advantages in terms of multiplexing, miniaturization and high through-put sensing but usually have low resolution on refractive index measurements. In a first project, the 2-D nature of the nanohole array was exploited in order to build a sensor based on the balanced detection of the signal in the x-axis polarzation with the signal in the y-axis polarization. This method doubled the sensitivity while rejecting spurious noise contribution to the signal.

While the preceding method gave interesting performances for sensing, the implementation of the technique in order to build a miniaturized multiplexed system wasn't achievable. Another approach, using a multiperiodic nanohole array, was developed. These structures consisted in a series of rows of nanohole arrays with incrementally ascending period. The diffraction of light is thus different for each row and will thus consists in a wavevector scan. The transmission image gives the resonance profile based on the spatial position of the transmission peak maxima. This method of detection requires a simple optical setup while achieving a sensing measurement which considerably reduces noise and allows to performs high resolution measurements. It also provides a sensor which is more accurate and reliable.

TABLE DES MATIÈRES

DÉDICACE iii

REMERCIEMENTS iv

RÉSUMÉ v

ABSTRACT viii

TABLE DES MATIÈRES x

LISTE DES TABLEAUX xiv

LISTE DES FIGURES xv

LISTE DES SIGLES ET ABRÉVIATIONS xxvii

LISTE DES ANNEXES xxviii

CHAPITRE 1 INTRODUCTION 1
- 1.1 Éléments de la problématique 4
- 1.2 Objectifs de recherche 4
  - 1.2.1 Objectifs de modélisation 4
  - 1.2.2 Objectifs de fabrication 4
  - 1.2.3 Objectif de développement du biocapteurs 5
- 1.3 Plan de la thèse 5

CHAPITRE 2 APPROCHE ET JUSTIFICATION DE LA MÉTHODE 6
- 2.1 Analyse de l'approche au niveau de la modélisation 6
  - 2.1.1 Méthodes Numériques 7
  - 2.1.2 Méthodes analytiques 8
- 2.2 Analyse de l'approche au niveau de la fabrication 10
  - 2.2.1 Faisceau d'ions focalisés 10
  - 2.2.2 Lithographie par faisceau d'électrons 11
  - 2.2.3 Lithographie par nanoimpression 13
  - 2.2.4 Lithographie par nanosphère 13
  - 2.2.5 Lithographie par interférence 14

2.2.6 Transfert par pelage de motif 14
2.2.7 Sommaire des méthodes et comparaison 15

CHAPITRE 3 ARTICLE 1 : SENSING WITH PERIODIC NANOHOLE ARRAY (REVUE DE LITTÉRATURE) 18
3.1 Auteurs 18
3.2 Introduction 18
3.3 Experimental results of sensing with nanohole arrays 21
3.3.1 First reports of sensing with nanohole arrays 21
3.3.2 Resolution Improvement Methods 22
3.3.3 Report of multiplexed detection 25
3.3.4 Improvement in surface roughness 26
3.3.5 Delivery of analytes towards the surface 26
3.3.6 Fully integrated systems 28
3.3.7 Nanohole array as a diagnostic tool 28
3.3.8 Survey of the performances of nanohole array sensors 29
3.4 Performances of nanohole array sensors 31
3.5 Coupled mode theory 34
3.5.1 Field Equations 35
3.5.2 Overlap integrals 38
3.5.3 Scattering coefficients 39
3.5.4 Connecting Matrix 41
3.5.5 Dispersion relation and zero-order approximation 42
3.6 1-D Nanoslit arrays 43
3.6.1 Case of a perfect electrical conductor 43
3.6.2 Case of real metal 51
3.6.3 Case $n_1 \neq n_3$ 56
3.6.4 Nanoslit arrays - Conclusions 58
3.7 2-D Square Nanohole array 59
3.7.1 Case of perfect electrical conductor 60
3.7.2 Case of real metal 66
3.7.3 Case $n_1 \neq n_3$ 71
3.7.4 Square hole arrays - Conclusion 74
3.8 Conclusion 74

CHAPITRE 4 ARTICLE 2 : OPTICAL TRANSMISSION THEORY FOR METAL-INSULATOR-METAL PERIODIC NANOSTRUCTURES 76

4.1 Auteurs . . . 76
4.2 Abstract . . . 76
4.3 Introduction . . . 77
4.4 Theoretical model . . . 78
4.4.1 Scattering Coefficient . . . 78
4.4.2 Multiple path calculation . . . 80
4.5 Results . . . 83
4.5.1 Transmission in the subwavelength regime with a thick dielectric layer 83
4.5.2 Transmission in the subwavelength regime with a thin dielectric layer 85

CHAPITRE 5 ARTICLE 3 : ELECTRON BEAM LITHOGRAPHY USING A PMMA/P(MMA 8.5 MAA) BILAYER FOR NEGATIVE TONE LIFT-OFF PROCESS . . . 88
5.1 Auteurs . . . 88
5.2 Introduction . . . 88
5.3 Experiment . . . 89
5.4 Results and discussion . . . 92
5.5 Summary and Conclusion . . . 95
5.6 Acknowledgement . . . 95

CHAPITRE 6 ARTICLE 4 : INTENSITY BASED SURFACE PLASMON RESONANCE SENSOR USING A NANOHOLE RECTANGULAR ARRAY . . . 96
6.1 Auteurs . . . 96
6.2 Abstract . . . 96
6.3 Introduction . . . 96
6.4 Basic Idea and Approach . . . 98
6.5 Fabrication, design and optimization of the nanohole rectangular array . . . 98
6.6 Instrumental Methodology . . . 100
6.7 Results and Discussion . . . 101
6.8 Conclusion . . . 103
6.9 Acknowledgements . . . 103

CHAPITRE 7 ARTICLE 5 : MULTIPERIODIC NANOHOLE ARRAY FOR HIGH PRECISION MULTIPLEXED SENSING . . . 104
7.1 Auteurs . . . 104
7.2 Abstract . . . 104
7.3 Introduction . . . 104
7.4 Approach and Experimental Setup . . . 106

7.5 Results and discussion 107

CHAPITRE 8 DISCUSSION GÉNÉRALE 110
8.1 Discussion sur la méthode de modélisation employée 110
8.2 Discussion sur les méthodes de fabrication employées 111
8.3 Discussion sur la conception des biocapteurs 112

CHAPITRE 9 CONCLUSION ET RECOMMANDATIONS 113
9.1 Synthèse des travaux 114

RÉFÉRENCES 116

ANNEXES 130

LISTE DES TABLEAUX

Tableau 2.1	Avantages et inconvénient des différentes méthodes de fabrication . .	15
Tableau 2.2	Répertoire des méthodes employées pour la fabrication de nanotrous pour la conception de biocapteurs	16
Tableau 3.1	Sensitivity and resolution of nanohole array	32

LISTE DES FIGURES

Figure 1.1 a) Un réseau de nanotrou. b) Transmission optique du réseau. Les maximas de transmission correspondent aux résonances de la structure. Tiré de (Ebbesen et al., 1998). 1

Figure 2.1 Schéma des différentes sphères de développement abordées dans ce travail de doctorat. 6

Figure 2.2 a) Représentation de l'espace discrétisé de simulation. b) Pas de temps de propagation de l'onde à l'intérieur du domaine de simulation. Clichés obtenus à l'aide du logiciel *Lumerical*. 7

Figure 2.3 a) Maillage des éléments du domaine de simulation. b) Solution représentant $|E|$. Clichés obtenus à l'aide du logiciel COMSOL. 8

Figure 2.4 Exemple d'un milieu décrit à l'aide d'une expansion de Fourier d e la constante diélectrique. 9

Figure 2.5 (a)Représentation en dipôle des réseaux de nanotrous et représentation du champ. p représente la polarisation des dipôles, α_e est la polarisabilité de la géométrie considérée, et G_E est le terme d'interaction dipolaire. Tiré de (De Abajo, 2007) 9

Figure 2.6 a) Station de travail du faisceau d'ions focalisés. Tiré de *FEI* b) Principe de pulvérisation de la matière. Tiré de (Utke et al., 2008) 11

Figure 2.7 a) Station de travail de lithographie par faisceau d'électrons.Tiré de *Raith*b) Simulation Monte Carlo de l'absorption et de la diffusion des électrons à travers la résine. 11

Figure 2.8 a) Procédure pour un transfert de motif par lift-off. b) Procédure pour un transfert par gravure. Tiré de (Zhou, 2005) 12

Figure 2.9 Procédure pour la lithographie par nano-impression. Tiré de (Malyarchuk et al., 2005). 13

Figure 2.10 a) Procédure pour la lithographie par nano-sphère. Tiré de (Wu et al., 2008). 14

Figure 2.11 a) Procédure pour la lithographie par interférence 14

Figure 2.12 a) Procédure pour la lithographie par interférence 15

Figure 3.1 Principle of sensing with nanohole array. As molecules bind to the surface of the structure the resonant wavelength shifts and the change in intensity or of the position of the maxima is used as the signal. . . 19

Figure 3.2 1- (A and B) Scanning electron microscopy images of a typical array of sub-wavelength holes. The image in part B is an enlargement of the array presented in part A. (C) Normalized transmission spectra of white light through three arrays of sub-wavelength holes. All arrays were patterned in a 100-nm-thick gold film deposited on the glass slide, and the diameters of the holes were about 200 nm. The lattice parameters (periodicities) of arrays a-c were 618, 545, and 590 nm, respectively. 2- Normalized transmission spectra of normally incident white light through an array of sub-wavelength (200 nm diameter) holes on a 100-nm-thick gold substrate deposited on a glass slide. (a) Bare (clean) Au surface ; (b) Au modified with a monolayer of MUA ; (c) Au-MUA modified with BSA. Reprinted with permission from Brolo et al. (2004). Copyright 2004 American Chemical Society. 21

Figure 3.3 (a) The optical image of a 10×10 microarray on a glass slide (b) The SEM image of a 600nm-period gold nanohole array. (c) The SEM image of a 600nm - period gold nanoslit array. Reprinted with permission from Lee et al. (2009). Copyright 2009 Optical Society of America. 22

Figure 3.4 1-Conceptual diagram of the 2-D nanohole-array-based SPR sensor. The input and output polarization states of a tunable laser are controlled, providing variable spectral or angular Fano-type profiles. A microfluidic channel is used to transport the analyte fluid to the surface of the sensing area and can be used to control the refractive index on the metal-dielectric interface to tune the SPP resonance frequency. Also shown is a scanning electron microscopy image of a representative sample. 2-Normalized transmission as a function of a) energy (wavelength). Reprinted with permission from Tetz et al. (2006). Copyright 2006 Optical Society of America. 23

Figure 3.5 1.a) Scanning electron microscopy (SEM) image of a 16×16 nanohole array with a 200 nm hole size and 380 nm periodicity. b) A bright-field microscope image of 5×3 microarray of nanohole arrays (partially shown). Each sensing element, a 16×16 nanoholes array as in (a), is separated by $50\mu m$. c) The PDMS chip, shown with microfluidic flow cells and tubing. Reprinted with permission from Lesuffleur et al. (2008). Copyright 2008 Optical Society of America. 25

Figure 3.6 Flow-through nanohole arrays. (a) Schematic of the optical and fluidic test setup employed for both fluorescence tests and transmission spectroscopy. (b) comparison of response to surface adsorption achieved with flow-over and flow-through formats as indicated inset. Measured peak shift (625 nm peak) is plotted as a function of time during flow through/over of an ethanol/MUA solution. As indicated in the inset, the flow-through sensor is operated with flow from the nonparticipating silicon nitride side to the active gold surface. The flow-through case results in a characteristic rate constant of k_{abs}) $3.8 \times 10^{-2} min^{-1}$ as compared to k_{abs}) $6.4 \times 10^{-3} min^{-1}$ for the flow-over case. Adapted with permission from Eftekhari et al. (2009). Copyright 2009 American Chemical Society. 27

Figure 3.7 a) Real picture of the portable biosensing device, weighing 60 g and 7.5 cm tall designed for point-of-care applications. In the picture, the hand of the author highlights the compactness of the device. Reprinted with permission from Cetin et al. (2014). Copyright 2014 Nature Publishing Group. b) A prototype miniaturized nPLEX imaging system developed for multiplexed and high throughput analysis of exosomes. The system uses a complementary-metal-oxide semiconductor (CMOS) imager to record the transmitted light intensity from a nPLEX chip. Reprinted with permission from Im et al. (2014). Copyright 2014 Nature Publishing Group. 29

Figure 3.8 a)An example of antibody O4 binding to the surface of a live immature rat oligodendrocyte b) SPR kinetic curves for IgM autoantibodies binding to SLBs. (a) O4 binding to SLBs containing 2% Sulf. Reprinted with permission from Wittenberg et al. (2012). Copyright 2012 American Chemical Society. c) SEM indicates specific exosome capture by functionalized nPLEX d)Putative ovarian cancer markers (EpCAM, CD24, CA19-9, CLDN3, CA-125, MUC18, EGFR, HER2), immune host cell markers (CD41, CD45) and a mesothelial marker (D2-40) were profiled on exosomes (b, using nPLEX sensor). Reprinted with permission from Im et al. (2014). Copyright 2014 Nature Publishing Group. 30

Figure 3.9 a) Definition of the Full Width at Half Maximum (FWHM) and depth of the resonant peak. b) Definition of the different sensitivities used in this article : bulk sensitivity (S_b) is relative to a change of refractive index in medium 1 and 2, surface sensitivity S_s is relative to a change if refractive index in medium 1 only and the layer sensitivity S_l is relative to a change of refractive index occurring in a layer of thickness L at the surface of the structure. These section define the volume of the field integral involved in Eq 3.3 32

Figure 3.10 a) A schematic representation of a unit cell of a periodic nanoslit (or square nanohole) array 34

Figure 3.11 Electric field definition for each medium of the structure. Tangential part of the fields are contained in the braket factor. The fields in region 1 and 3 are represented as a sum of diffracted plane waves, while in region 2 the fields are given by the waveguide mode, which depends on the geometry. 35

Figure 3.12 a) Electric field inside a PEC and a real metal waveguide b) Principle of the effective index method for rectangular waveguides, which are separated into the modes of 2 parallel plates waveguides. The propagation constant of the TM modes of the 1st waveguide is introduced as an effective dielectric constant $\epsilon_{eff} = \beta_1/k_w$ into the TE modes of the second waveguide. 38

Figure 3.13 Schematic representation of a nanoslit array. 44

Figure 3.14 a) Transmission spectra of nanoslit arrays obtained using the model based on CMT (black line) and a numerical simulation using FEM (red dotted line) for period of $0.55\mu m$ with slit size $a = 0.1\mu m$ for 3 different thickness b) Dispersion relation of a slit array with parameters $d = 0.55\mu m$, $a = 0.1\mu m$ and $h = 0.4\mu m$. The red lines correspond to the zero-order approximation (ZOA) dispersion relation given by Eq 3.44 for the symmetrical and asymmetrical cases. The black lines are resonance conditions given by Eq 3.42. 44

Figure 3.15 a) Sensitivity and b) FWHM of the slit array obtained using CMT as a function of period with slit width $a = 0.2d$ and thickness $h = 0.2d$. The sensitivity equation given by the zero-order approximation of Eq 3.46 is given by the dashed black lines. 47

Figure 3.16 a) Transmission spectra and b) Reflection coefficient for a nanoslit array of period $d = 0.45\mu m$ and thickness $0.2\mu m$ for 3 different slit widths. 48

Figure 3.17 Resolution of the array (Eq 3.2) for 3 different cases. 1- The slit width and thickness $a = 0.4h = 0.2d$ are kept proportional to the period. 2- Thickness is kept proportional $h = 0.4d$ while slit width is constant $a = 0.1\mu m$. 3- Slit width is kept proportional to the period $a = 0.2d$ while the thickness is kept constant $h = 0.2\mu m$ 49

Figure 3.18 a) Electric fields norm $|E|$ obtained using CMT for a nanoslit of period $d = 0.55\mu m$, slit width $a = 0.1\mu m$ and thickness $h = 0.2\mu m$. b) Fields in region 1-3 given by the diffraction orders (+1), (+2) and (+3) and fields inside the slit for TM modes 0,2 and 4. These last 3 graphs have been cropped for improved visualization. 50

Figure 3.19 a) Transmission spectra for slit period $0.55\mu m$ and slit opening $a = 0.1\mu m$ the 3 different thickness and different refractive index for the different regions. The red line corresponds to a refractive index of 1.33 for all region. The black dashed line are the transmission with a change of refractive index to 1.43 for the surfaces of the slit only. The black line represents the shift for a change of refractive index in all region. b) Black line - Percentage of the shift in resonance peak position due to the change of refractive index at the surface as a function of thickness. Red dashed line - Field integral percentage of the field contained on the surfaces of the array. 50

Figure 3.20 a) Transmission spectra of nanoslit arrays obtained using CMT for period of $0.55\mu m$ with slit size $a = 0.1\mu m$ with gold as the metallic layer (black lines) for 3 different thickness. The red dashed line corresponds to numerical simulations using FEM. b)Dispersion relation of nanoslit array of dimensions $d = 0.55\mu m$, $h = 0.4\mu m$ and $a = 0.1\mu m$. The red lines are the dispersion relation obtain under the ZOA (Eq 3.50). The black lines are resonance conditions given by Eq 3.42. The red dashed line corresponds to the dispersion of an SPP on a flat surface, and coincides with the Wood anomaly following Eq 3.48. 51

Figure 3.21 a) Sensitivity of the nanoslit array as a function of period for a slit width of $0.2d$ and thickness of $0.2d$. The Red lines accounts for the total sensitivity (change of refractive index in all regions) and the red dashed-dotted line for bulk sensitivity only (change of refractive index in region 1-2). The black dashed curve represents the perfect conductor sensitivity case of λ/n. 53

Figure 3.22 Transmission spectrum and b) Reflection coefficients as a function of wavelength for nanoslit array of period $0.45\mu m$ and thickness $0.2\mu m$ for 3 different slit width. 53

Figure 3.23 Real and Imaginary values of the propagation constant as a function of wavelength for nanoslit array of period $0.45\mu m$ and thickness $0.2\mu m$ for 3 different slit width. The dashed line corresponds to the value for a PEC of width $a = 0.025\mu m$. 54

Figure 3.24 a) Resolution of the array at the optimal thickness and slit width. *Inset* Resolution as a function of slit width and array thickness for a period of $0.7\mu m$ b) Optimal thickness and slit width as a function of the period. 55

Figure 3.25 a) Electric field norm $|E|$ for a nanoslit array of period $0.55\mu m$ and slit opening $0.1\mu m$ for 3 different thickness $h = 0.1\mu m$, $0.2\mu m$ and $0.4\mu m$. b)Field percentage contained within a layer of thickness L on the top surface of the array for 3 different thickness of the metal film considered. The dashed line corresponds to the field percentage for the whole surface. 55

Figure 3.26 a) Transmission spectra obtained with CMT for a nanoslit array of period $0.55\mu m$ and slit width $0.1\mu m$ for 3 different thickness with the refractive index of glass ($n_3 = 1.51$) for region 3. The dotted red line is the result obtained with numerical simulation based on FEM. b) Dispersion relation for a nanoslit array of dimensions $d = 0.55\mu m$, $a = 0.1\mu m$ and $h = 0.4\mu m$ with gold as the metal and glass as the substrate. The black line corresponds to the resonance condition given by Eq 3.42. The red dashed lines corresponds to the dispersion of an SPP on a flat surface with the index of region 1 and 3, and coincides with the Wood anomaly following Eq 3.48. 56

Figure 3.27 a) Bulk sensitivity as a function of period of a nanoslit array with gold as the metal for the case of matching refractive index (red line) and glass as the substrate (black line) for a slit array of thickness $0.4d$ and slit width$0.2d$. b) Reflection coefficient product ρ_{21} and ρ_{23} as a function of wavelength for a slit array of period $d = 0.55\mu m$, slit width $a = 0.2d$ and thickness $h = 0.4d$ 57

Figure 3.28 a) Resolution of the array at the optimal thickness and slit width *Inset* Resolution as a function of slit width and array thickness for a period of $0.7\mu m$ b) Thickness and slit width that gave the optimal resolution. 58

Figure 3.29 a) Electric field norm $|E|$ for a nanoslit array of period $0.45\mu m$ and slit opening $0.1\mu m$ for 3 different thickness $h = 0.1\mu m$, $0.2\mu m$ and $0.4\mu m$ with glass as a substrate.
b)Field percentage contained within a layer of thickness L on the top surface of the array for 3 different thickness of the metal film considered. 58

Figure 3.30 Schematic representation of a square nanohole array 60

Figure 3.31 a) Transmission spectra of square nanohole arrays obtained using CMT (black lines) for period of $0.55\mu m$ with hole size $a = 0.20\mu m$ for 3 different thickness. The red dotted lines correspond to numerical results obtained using FEM. b) Dispersion relation of a square hole array with parameters $d = 0.55\mu m$, $a = 0.25\mu m$ and $h = 0.075\mu m$. The red lines corresponds to the ZOA dispersion relation given by Eq 3.54. The black lines are resonance conditions given by Eq 3.51 60

Figure 3.32 a) Sensitivity and b) FWHM of the square nanohole array obtained as a function of period with constant opening of the slit $a = 0.45d$ and thickness $h = 0.2d$. The sensitivity equation given by the zero order approximation of Eq 3.46 is given by the dashed black lines. 62

Figure 3.33 a)Transmission spectra and b) Reflection coefficient for a square hole array of period $d = 0.55\mu m$ and thickness $h = 0.075\mu m$ for 3 different hole sizes 63

Figure 3.34 a) Resolution of the square hole array (Eq 3.2) for 3 different cases. 1- The hole size and thickness $a = 0.5h = 0.25d$ are kept proportional to the period. 2- Thickness is kept proportional $h = 0.25d$ while the hole size is constant $a = 0.1\mu m$. 3- Hole size is kept proportional to the period $a = 0.5d$ while the thickness is kept constant $h = 0.2\mu m$ . . . 64

Figure 3.35 a) Electric Field Norm $|E|^2$ at plane coordinate $Y = 0$ of a square hole array of period $0.55\mu m$, thickness $h = 0.075\mu$ and hole width $a = 0.225\mu m$. b) Fields at the upper interface of the hole ($Z = -h/2$). c) Fields inside the hole ($Z = 0$) which corresponds to the summation of rectangular waveguide TM and TE modes. 64

Figure 3.36 a) Transmission spectra for square nanohole period $0.55\mu m$ and slit opening $a = 0.2\mu m$ for 3 different thickness and different refractive index for the different regions. Red line is for a refractive index of 1.33 for all region. Black dashed line is the transmission for a refractive index to 1.43 inside the holes only (Region 2) and the dotted black line for this change for the surfaces of the holes only (Region 1 and 3). The black line represents the shift for a change of refractive index in all regions. b) Black line - Percentage of the shift in resonance peak position due to the change of refractive index at the surface as a function of thickness. Red dashed line - Field integral percentage of the field contained on the surface of the array. 65

Figure 3.37 a) Transmission spectra of square nanohole arrays obtained using CMT for period of $0.55\mu m$ with hole size $a = 0.2\mu m$ for the case of gold metal (black lines). Results of FEM simulation is plotted in red dashed lines b)Dispersion relation of nanoslit array of dimensions $d = 0.55\mu m$, $h = 0.075\mu m$ and $a = 0.2\mu m$. The red dashed line is the dispersion relation obtained using the ZOA (Eq 3.50). The black lines are resonance conditions given by Eq 3.51. The red dashed line corresponds to the dispersion of an SPP on a flat surface, and coincides with the Wood anomaly following Eq 3.48. 66

Figure 3.38 Sensitivity (black line) of a square hole array as a function of period for a hole size of $a = 0.35d$ and thickness $h = 0.3d$. The comparison with the perfect conductor case equation λ_r/n (red dashed line) and the SPP sensivitiy for a flat surface (blue dotted line). The bulk sensitivity, corresponding to a change of refractive index in region 1 and 2 only, is in the black dotted-dashed line. 68

Figure 3.39 a) Transmission spectrum and b) Reflection coefficients for a gold square hole array of period $0.55\mu m$ and thickness $h = 0.150\mu m$ for 3 different hole width. 68

Figure 3.40 Imaginary and real components of the propagation vector inside the holes for 3 different hole width. These values are compared with the propagation constant of a square hole of $0.225\mu m$ for a PEC (magenta). 69

Figure 3.41 a) Resolution of the square hole array at optimal thickness and hole size as a function of the period of the array for the case of a matching index substrate. *inset* Resolution of the array as a function of hole size and thickness for a periodicity of $d = 0.45\mu m$. b) Value of the optimal thickness and hole width for each period of the square hole array. . . 70

Figure 3.42 a) Electric field norm $|E|$ for a nanosquare hole array of period $0.55\mu m$ and hole opening $0.225\mu m$ for 3 different thicknesses $h = 0.075\mu m$, $0.15\mu m$ and $0.3\mu m$ with an index matching substrate. b) Field percentage contained within a layer of thickness L on the top surface of the array for 3 different thicknesses of the metal film considered. 70

Figure 3.43 a) Transmission spectra of square nanohole array with a glass substrate obtained using CMT. The period is $0.55\mu m$ with a hole size of $a = 0.2\mu m$ and the case of gold metal (black lines) is plotted. The red dashed line correspond to numerical calculation made using FEM b)Dispersion relation of nanoslit array of dimensions $d = 0.55\mu m$, $h = 0.1\mu m$ and $a = 0.20\mu m$ with glass as the substrate. The black line is the resonance condition given by Eq 3.51. The red dashed lines corresponds to the dispersion of an SPP on a flat surface (on interface 1 and 2), and coincides with the Wood anomaly following Eq 3.48. . . 71

Figure 3.44 Bulk sensitivity (black line) of square hole array as a function of the period for a hole size of $a = 0.3d$ and thickness of $h = 0.25d$. The values are compared to the sensitivity of a PEC given by λ/n (red dashed line) and the sensitivity of a SPP on a flat surface (blue dotted line) 72

Figure 3.45 a) Resolution of the square hole array at optimal thickness and hole size as a function of the period of the array for the case of a glass substrate. *inset* Resolution measurements as a function of the hole size and metal thickness for the period $d = 0.7\mu m$. b) Optimal values of the thickness and hole size for each period considered. 73

Figure 3.46 a) Electric field norm $|E|$ for a nanosquare hole array of period $0.55\mu m$ and hole opening $0.2\mu m$ for 3 different thickness $h = 0.075\mu m$, $0.15\mu m$ and $0.3\mu m$ with glass as the substrate. b) Field percentage contained within a layer of thickness L on the top surface of the array for 3 different thickness of the metal film considered. 73

Figure 4.1 Unit cell representation of the periodic MIM structure. The dashed rectangle represents the structure with periodicity d ; slit width a ; and thicknesses h_1, h_2, and h_3 for the top metal, dielectric, and bottom metal layers, respectively. 78
Figure 4.2 Field definition for each region of the structure. 79
Figure 4.3 (A) The different loops inside the MIM structure. (B) The expansion of loop f_{23} by taking into account the first diffraction orders. 81
Figure 4.4 Transmission of the MIM periodic structure for dimensions $a = 0.25d$, $h_1 = h_3 = 1.6d$, and $h_2 = 2d$. 84
Figure 4.5 Dispersion curves of the MIM structure with dimensions $h_1 = h_3 = 1.6d$, $a = 0.25d$, and $h_2 = 2d$. The dashed black line represents the resonance condition for the f_{12} loop and the gray dashed line for the f_{13t} loop. 85
Figure 4.6 (A) Dispersion relation for MIM structure with $h_1 = h_3 = 1.6d$, $a = 0.25d$, and $h2 = 0.5d$. Discontinuities in the dispersion curves can be found for the upper branches. Subpanel : transmission coefficient with diffraction order (B) 0 and (C) –1 considered for the direct transmission term t^d. 86
Figure 5.1 Process flow of the lift-off procedure based on the negative tone PMMA/P(MMA 8.5 MAA) resist bilayer. 90
Figure 5.2 (a) Relative height and (b) width of the patterned features as a function of exposure dose with silicon as the substrate. The implemented width of the features was 200 nm. 91
Figure 5.3 AFM measurements of the cross-section of the PMMA 495 resist on silicon for several doses (dashed line represents the implemented cross-section of the feature). Inset : 3D plot of the AFM measurement of the PMMA 495 k features on silicon. 92
Figure 5.4 (a) Nanohole array and (c) nanoslits array after metal deposition showing an undercut profile. (b) and (d) Nanoholes and nanoslits after lift-off. (e) and (f) Cross-section of the nanoslits configuration before and after lift-off. The final slit structure is 100nm wide, 100 nm thick ; the slits are 400 nm apart. 93
Figure 5.5 (a) Nanoslits of 51 nm and (b) nanoholes of 58 nm dimension both with a 200nm pitch and 100nm thickness of gold. 94

Figure 5.6 Experimental and simulated transmission spectrum of nanohole arrays of 475nm period, 190nm diameter and 100 nm thick gold layer with water as the medium. 95

Figure 6.1 Principle of the proposed technique using a nanohole rectangular array with different periodicities ax and ay along the two main axes. The transmission spectrum of such a structure is shown with resonant peaks at different wavelength for the two orthogonal polarizations. The point of intersection (Point A) corresponds to the initial calibration point. The change in refractive index (red curves) shows an increase of intensity for one polarization (point B) and a decrease for the other polarization (point C). 99

Figure 6.2 (a) Scanning electron microscopy image of an example of a nanohole rectangular array 380 nm x 420 nm (b) Transmission spectra of nanohole rectangular arrays with period 380 x 415nm (solid line), 390 x 425 nm (dashed line) and 395 x 435 nm (dotted-dashed line). The positions of the peaks are red-shifted of (from left to right 28 nm, 27 nm, 29 nm, 28 nm, 29 nm, 26 nm in comparison to the dispersion relation (square dots). 100

Figure 6.3 (a) Schematics of the optical setup used for the sensing experiment. (b) Adjustment of the initial calibration point by rotating the second polarizer from 45° to 35°. The intensities for both polarizations intersect at the source's wavelength. 101

Figure 6.4 (a) Transmission spectra of the nanohole array with 380 x 420 nm as periods in water and ethanol. (b) Responses of the sensing system for small increase of ethanol. Insert : Noise levels from the signal of the balanced detection and from the signal of a single polarization. 102

Figure 7.1 a) Multiperiodic nanohole array. Each column has a periodicity equal to $d_0 + ni$, where d_0 is the initial period, n is the number of the column and i is the increment. b) The transmission image of the structure will exhibit a bright fringe for column with periods that match the resonant condition of the array. Changing the refractive index will move the fringe and the position of the maxima is the sensing signal. 106

Figure 7.2 *Reflection* image of the multiperiodic nanohole array under white light illumination, using crossed polarizers. The sample reflects a different color which is dependent of the periodicity. c) Nanohole array with changing period (the total sample goes from 500-600nm) in the x axis and a 700 nm period in th y axis. The hole size is 180 nm and the thickness of the gold film is 100 nm. 106

Figure 7.3 The optical setup consists in a home made microscope with a monochromatic laser diode source, a spatial filter and polarizer. The microscope objective was 25x. b) The PDMS microfluidic chip with 3 parallel channels. 107

Figure 7.4 Transmission image of the multiperiodic nanohole array sample with 1) water and 2) ethanol as the surrounding medium. b) *top* Measured transmission profile of the images of the arrays. The intensity was integrated along the y-axis and plotted as a function of the x-axis. *bottom* Transmission intensity of the nanohole array as a function of the period as calculated using coupled mode theory. 108

Figure 7.5 108

Figure A.1 Interface utilisateur Matlab pour obtenir les spectres de transmission et de réflexion de réseaux de nanotrous périodiquespour nimporte quelle dimension et indice de réfraction pour la structure. La distribution de champ électrique est aussi incluse 130

LISTE DES SIGLES ET ABRÉVIATIONS

FIB	"Focused Ion Beam" pour Faisceau d'Ions Focalisés
EBL	"Electron Beam Lithography" pour Lithographie par Faisceau d'Électrons
FDTD	"Finite Difference Time Domain" pour méthode des Différences Finies dans le domaine temporel
FEM	"Finite Element Method" pour méthode des éléments finis
CMT	"Coupled Mode Theory" pour Méthode des modes couplés
ELISA	Enzymed-Linked Immunosorbent Assay
SPP	Surface plasmon polariton

LISTE DES ANNEXES

Annexe A	Guide Matlab CMT pour les réseaux de nano-indentations	130
Annexe B	Code Matlab pour les structures 1-D Nanoslit Metal-Insulator-Metal	131
Annexe C	Publications et Conférence	132
Annexe D	Performances des capteurs	134

CHAPITRE 1 INTRODUCTION

Le sujet de la thèse porte sur les nano-réseaux d'indentations métalliques, de leur fabrication, de la modélisation de leurs propriétés optiques ainsi que de leurs applications comme biocapteurs. La structure d'intérêt consiste en un réseau périodique de trous dans un film métallique d'épaisseur fine, soit de dizaines à quelques centaines de nanomètres. Ces structures possèdent des propriétés optiques remarquables. Tel qu'observé par Ebbesen en 1998 (Ebbesen et al., 1998) et publié dans *Nature*, la lumière peut entrer en résonance avec la structure pour être transmise de manière "extraordinaire". Ce terme fut utilisé dans le papier d'origine pour identifier une transmission optique qui dépassait largement ce qui était attendu d'une simple somme de la transmission des trous individuels. Effectivement les pics de résonance se manifestait pour des fréquences inférieures à la fréquence de coupure des ouverture dans le métal, et les théories classiques d'interaction entre une onde et un trou d'aussi petite dimension donnait des facteurs très faibles de couplage (Bethe, 1944). L'arrangement des trous en réseaux périodiques contribuait donc à modifier les propriétés de transmission. Puisque la résonance se manifestait pour des longueurs d'ondes supérieur à la période du réseau, le terme employé fut la transmission optique extraordinaire de réseau sous longueur d'onde (ou "subwavelength hole array"). Une particularité de ce régime est que les ordres de diffraction sont évanescents et donc liés à la surface.

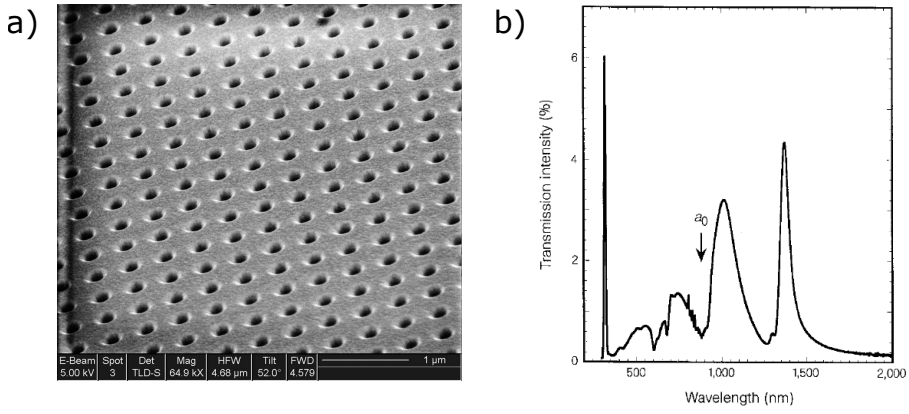


Figure 1.1 a) Un réseau de nanotrou. b) Transmission optique du réseau. Les maximas de transmission correspondent aux résonances de la structure. Tiré de (Ebbesen et al., 1998).

La compréhension de l'origine de cette propriété optique remarquable ne s'est pas fait directement. Bien qu'il était clair que la transmission résultait d'un couplage avec une onde de surface, l'hypothèse de départ utilisant les conditions de résonance des plasmons de sur-

face (ou SPP) ne s'avérait pas exacte. Cette hypothèse consistait en un matching du vecteur d'onde de l'onde plasmonique avec le vecteur d'onde diffracté (et évanescent) du réseau. La position de la résonance était cependant toujours légèrement décalée vers le rouge comparativement à la théorie. Bien que certains y voyait la simple interaction de l'onde de surface avec une partie "non-résonante" de la transmission dans une interaction de type Fano (Genet et al., 2003), d'autres incongruités venaient complexifier la compréhension de l'origine de la résonance. En effet, l'amplification de la transmission optique se manifestait également lorsqu'on considérait, dans les outils de modélisation, le métal comme un conducteur parfait (PEC), qui ne peut pas supporter de SPPs.

Une manière de décrire cette résonance se faisait en analysant l'admittance du mode guidé à l'intérieur de la cavité qui divergeait pour une certaine longueur d'onde (Martin-Moreno et al., 2001). Cette admittance représente le couplage entre l'onde incidente et l'onde à l'intérieur du trou, et est représentée par une intégrale de recouvrement des champs électromagnétiques à l'interface des milieux. Mais ce n'est qu'avec un papier de (Pendry et al., 2004) que davantage de compréhension sur le type de résonance fut établie. Le papier avançait que les réseaux de nano-indentations étaient équivalent à, dans la limite de grandes longueurs d'onde par rapport aux dimensions du réseau, un métamatériau continu possédant une constante diélectrique dépendante de la géométrie. Il était ainsi possible d'écrire la relation de dispersion du phénomène de résonance :

$$k_{//}^2 c_0^2 = \omega^2 + \frac{1}{\omega_{pl} - \omega} \frac{64 a^4 \omega^4}{\pi^4 d^4} \tag{1.1}$$

ou a est la taille de l'indentation, d la période, c_0 la vitesse de la lumière, ω la fréquence angulaire de l'onde, ϵ_h la constante diélectrique du matériau à l'intérieur de l'indentation et μ_h sa perméabilité magnétique.

Cette relation de dispersion ressemble à la relation des SPPs, mais dont la dispersion ne dépend pas de la propriété du matériau mais de la géométrie de la structure. L'auteur réfère même à des "spoofs" plasmons, soit des ondes qui imitent le comportement de résonance des SPPs. Bien que ce modèle n'est valide que pour des dimensions de la structure bien inférieures à la longueur d'onde, il présenta pour la première fois l'idée d'une onde de surface émergeant à cause de la géométrie périodique de la structure.

Mais cela ne représentait toujours pas une représentation complète du phénomène. Il restait à détailler quel était la contribution du matériau, et donc si les SPPs contribuaient d'une façon ou d'une autre à la transmission optique. Après tout, celle-ci était observée expérimentalement sur des surfaces métalliques, et se manifestait particulièrement sur des métaux très

conducteurs, tout comme avec la résonance plasmonique de surface. Une certaine confusion était présente du fait que de la position d'un minima de transmission, juste avant le profil de résonance, concordait avec la condition d'excitation des SPPs sur une surface plane. Certains y voyait la contribution des plasmons de surface comme étant négative (Cao and Lalanne, 2002; Lochbihler and Depine, 2012; Lin and Roberts, 2011; Lalanne et al., 2003; Crouse and Keshavareddy, 2005; Xie et al., 2005), et qui constituait un mécanisme de perte non-radiative de l'onde. Il existait une certaine confusion avec ce qui est identifié comme l'anomalie de Wood, qui était l'origine des minimas de transmission.

Cette approche est considérée aujourd'hui comme erronée, et la contribution des SPPs est maintenant généralement reportée comme étant positive par la plupart des articles (Barnes et al., 2004; Liu and Lalanne, 2008; Garcia-Vidal et al., 2010; Yoon et al., 2014), c'est-à-dire contribuant à un maxima. En fait, la transmission optique extraordinaire est vue comme le résultat d'un phénomène complexe de la multiple diffraction de l'onde à la surface des trous. La nature de la propagation de l'onde de surface dépend de l'espacement entre les trous. Lorsque cette distance est petite, comme c'est le cas pour les réseaux considérés dans cette thèse, l'ensemble des ordres de diffraction évanescents contribue au couplage de l'onde avec les modes guidés à l'intérieur des trous. Ces ondes de surface représente un hybride entre une onde cylindrique évanescente et la résonance plasmonique de surface (Liu and Lalanne, 2008), la dispersion de celle-ci étant modifiée par la présence des trous.

Une partie de cette thèse s'est donc affairée à comprendre en détail les mécanismes en jeu, et à faire un approfondissement de la modélisation afin de mieux comprendre le potentiel de ces structures pour la biodétection. Ce potentiel est mesuré selon la réponse que possède cette résonance à un changement d'indice de réfraction. Le but est également de comparer les métriques de biodétection pour vérifier si ce type de structure peut atteindre des performances similaires à ceux des biocapteurs SPR. Cela fait donc partie d'un article de revue qui se veut également être un tutoriel sur la modélisation des structures nanoplasmoniques à l'aide de la méthode des modes couplés.

Suite à ce travail de modélisation, un travail expérimental de mise en oeuvre de ces structures pour la biodétection est présenté. Une première partie présente la procédure utilisée pour fabriquer les nanostructures. Ces travaux ont fait l'objet d'un article puisqu'il s'agissait d'une méthode nouvelle utilisant un lift-off avec une bicouche de résine négative.

Les objectifs quant au développement des capteurs étaient surtout voués à améliorer leurs performances. En effet, la plupart des capteurs rencontrés dans la littérature possédait des performances parfois jusqu'à 2-3 ordres de grandeur inférieurs en terme de résolution comparativement à des biocapteurs SPR conventionnels, ce qui réduisait leur potentiel d'attrait.

En plus de l'optimisation apportée par l'analyse théorique du phénomène en jeu, des méthodes liés au systèmes optiques et aux méthodes d'interrogation du signal sont au centre des développements technologiques proposés.

1.1 Éléments de la problématique

D'un point de vue plus général, le but du projet est de comprendre les phénomènes physiques en jeu dans la transmission optique de nanostructures périodiques. Le développement d'outils de modélisation permet d'étudier le rôle de chacun des paramètres de ses structures et de comprendre en détails les modalités de propagation de la lumière dans ces matériaux non conventionnels. Un outil global de modélisation permettra aussi d'optimiser les nanostructures pour la détection des analytes souhaités.

Le travail expérimental repose sur le développement de la partie capteur optique. Le capteur sera multiplexé, c'est-à-dire qu'il devra permettre de réaliser plusieurs détections à la fois. Il devra être très précis et fiable : les limites de détection devront être comparables à un biocapteur SPR standard ($1 \times 10^{-7} RIU$) et ne devront pas générer de faux signaux. Il intégrera la partie fluidique à l'aide d'une membrane microfluidique possédant autant de canaux que de capteurs. Un logiciel de lecture permettra une lecture simple du signal à l'écran d'un ordinateur en temps réel. Il devra utiliser un montage optique simple et peu coûteux.

Au niveau du capteur, la partie la plus essentielle repose sur les structures nano-périodiques. Une procédure de fabrication devra être mise en place qui permettrait de reproduire un design de capteur de manière rapide et peu coûteuse. La structure devra être compatible avec une méthode de fabrication à grande échelle.

1.2 Objectifs de recherche

1.2.1 Objectifs de modélisation

- Développer un outil de modélisation des réseaux de nanotrous périodiques
- Analyser l'effet des paramètres de la structure sur la transmission optique et déterminer les paramètres optimaux
- Déterminer les capacités de la structure pour la biodétection et identifier les limites

1.2.2 Objectifs de fabrication

- Développer une procédure de fabrication des réseaux de nanotrous à l'aide du faisceau d'ions focalisés

— Développer une recette de fabrication de réseaux de nanotrous périodiques à l'aide de la lithographie par électrons

1.2.3 Objectif de développement du biocapteurs

— Développer un dispositif multiplexé, c'est-à-dire pouvant réaliser plusieurs détections en simultané.
— Assurer la fiabilité du capteur pour la détection d'analytes ainsi que sa précision/résolution
— Intégrer le capteur dans un système microfluidique
— Concevoir un montage optique simple et peu coûteux

1.3 Plan de la thèse

1. Introduction
2. Approche et justification des méthodes
3. Modélisation
   (a) Papier 1 : Sensing with Periodic Nanohole Arrays
   (b) Papier 2 : Optical Transmission Theory for Metal-Insulator-Metal Periodic Nanostructures
4. Fabrication
   (a) Papier 3 : Electron beam lithography using a PMMA/P (MMA 8.5 MAA) bilayer negative tone lift-off process
5. Biodétection à l'aide de capteurs basés sur les réseaux de nanotrous périodiques
   (a) Papier 4 : Intensity Based Surface Plasmon Resonance Sensor Using a Nanohole Rectangular Array
   (b) Papier 5 : Multiperiodic Nanohole Array for High Precision Multiplexed Biosensor
6. Discussion Générale
7. Conclusion

CHAPITRE 2 APPROCHE ET JUSTIFICATION DE LA MÉTHODE

La démarche du travail regroupe l'ensemble des éléments de conception, de la modélisation des dispositifs jusqu'à leur fabrication et leur utilisation dans des tests expérimentaux de biodétection. L'ensemble des étapes possède une influence sur les autres, puisque, bien que les résultats de la modélisation déterminent les dimensions utilisés expérimentalement, le choix du substrat par exemple définira le choix au niveau de la modélisation. L'ensemble de ces étapes est illustré dans le schéma 2.1.

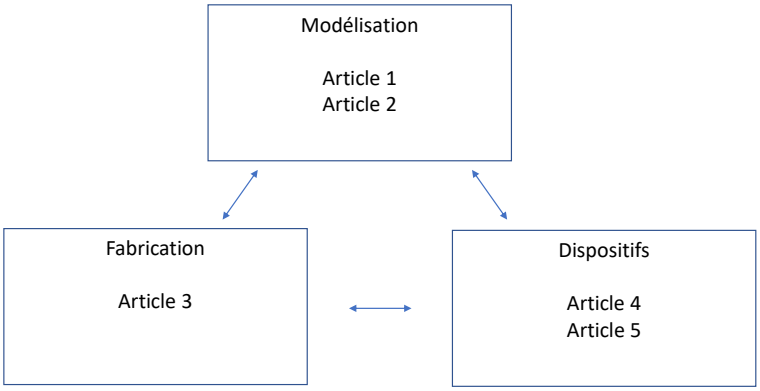


Figure 2.1 Schéma des différentes sphères de développement abordées dans ce travail de doctorat.

Dans ce qui suit nous présentons une certaine justification des choix faits pour la modélisation et la fabrication des échantillons. Ceci constitue une certaine introduction et une revue de littérature pour ces deux aspects du travail effectué. Pour ce qui est de la conception de biocapteurs, une grande revue de littérature est incluse dans l'article 1. La justification des méthodes employées pour cet aspect du développement est incluse directement dans les publications 4 et 5 puisqu'ils constituent le sujet même de celle-ci.

2.1 Analyse de l'approche au niveau de la modélisation

Dans cette thèse, la méthode des modes couplés a été mise de l'avant comme outil de modélisation afin de retrouver les propriétés optiques des structures étudiées. Il existe d'autres méthodes de modélisation retrouvées dans la littérature et nous en faisons ici une brève présentation afin de justifier la méthode choisie.

2.1.1 Méthodes Numériques

FDTD

La méthode des différences finies dans le domaine temporel (ou FDTD pour Finite Difference in Time Domain), présentée à la figure 2.2, est une méthode numérique. Elle implique une division du domaine à simuler en une grille de points, à partir desquels les équations de Maxwell discrétisées sont résolues. Elle simule ainsi chaque pas temporel de propagation d'une onde. En mesurant les amplitudes de l'onde à différents endroit du domaine de simulation, il est possible de déterminer les propriétés optiques (transmission, réflexion, concentration du champs...) de la géométrie d'intérêt.

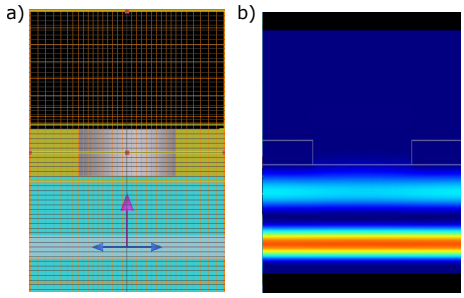


Figure 2.2 a) Représentation de l'espace discrétisé de simulation. b) Pas de temps de propagation de l'onde à l'intérieur du domaine de simulation. Clichés obtenus à l'aide du logiciel *Lumerical*.

Les avantages de cette méthode sont principalement la possibilité de résoudre des géométries complexes, ainsi que son implémentation simple et sa robustesse. Ses désavantages reposent sur une représentation erronée des géométries incurvées, un contrôle limité sur sa convergence et son exactitude ainsi que des temps de simulations plutôt longs.

Éléments finis

La méthode des éléments finis est un autre outil numérique, dans le domaine fréquentiel cette fois-ci, et est présentée à la figure 2.3. L'algorithme de résolution repose également sur une discrétisation de l'espace en de multiples éléments, ou parties de fonction. Les équations à résoudre sont réécrites sous une forme variationnelle dont la solution peut être discrétisée sur les multiples éléments. Un algorithme de résolution de la matrice de couplage entre les éléments permet de retrouver la solution sur l'ensemble du domaine.

Cette méthode est également très robuste et peut simuler n'importe qu'elle géométrie d'intérêt. Elle possède l'avantage sur sa technique connexe de la FDTD de pouvoir décrire les

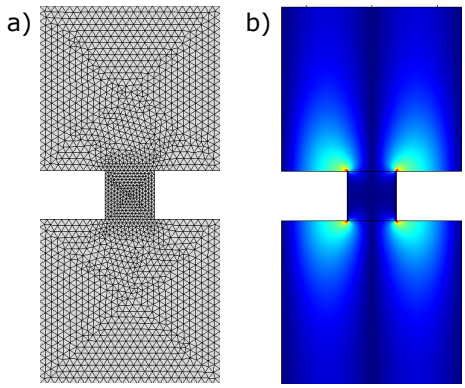


Figure 2.3 a) Maillage des éléments du domaine de simulation. b) Solution représentant $|E|$. Clichés obtenus à l'aide du logiciel COMSOL.

régions incurvées avec une grande précision ainsi que de contrôler plus facilement l'erreur et la convergence de la solution. Elle est toutefois plus complexe et fastidieuse à mettre en place (même avec des logiciels) et peut générer des solutions polluées, c'est-à-dire des solutions faussées provenant de la forme choisie de la résolution.

Ces méthodes numériques ne permettent pas d'écrire sous équations les propriétés optiques des structures d'intérêt, ce qui fait en sorte que l'utilisation de telles méthodes ne cadre avec les objectifs visés. De plus, le modèle doit permettre de cerner l'effet des multiples paramètres sur le profil de résonance des nano-trous. Un schéma numérique nécessite un plus long temps de calcul pour chaque combinaison de paramètres considérés, ce qui au final rend le processus difficilement réalisable. Il est à noter que ces méthodes ont tout de même été mises en place, et on servit de comparaison afin de corroborer la validité du modèle choisi. Les spectres de transmission présentés dans les publications sont comparés aux spectres obtenus à l'aide de la méthode des éléments finis.

2.1.2 Méthodes analytiques

Méthode rigoureuse des modes couplées

Cette méthode repose sur une description des champs à l'aide d'une expansion en différents modes et est représentée à la figure 2.4. Les constantes diélectriques des différents milieux du domaine sont représentées par une expansion en série de Fourier. Ceci a l'avantage de permettre la représentation de géométries diverses. Cependant cette façon de traiter les milieux est généralement assez lourde et complexe et est enclin à des erreurs de troncature des séries de Fourier.

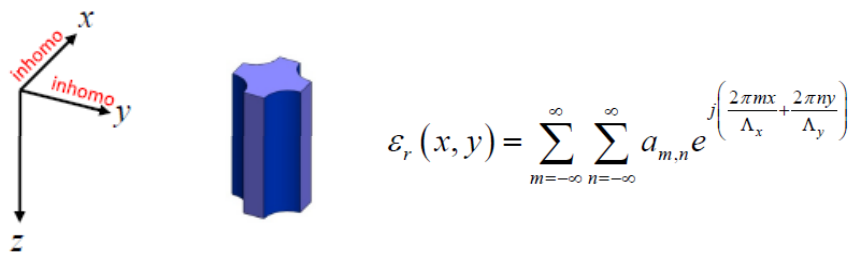
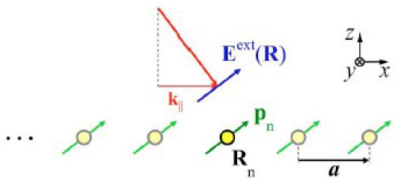


Figure 2.4 Exemple d'un milieu décrit à l'aide d'une expansion de Fourier d e la constante diélectrique.

Les travaux de (Lalanne et al., 2005a) ont permis de développer la méthode à la structure des nano-trous, ainsi que dans une version modifiée de la théorie présentée dans (Lalanne et al., 2005b) pour les nano-fentes.

Méthode des dipôles couplés

Dans cette méthode, chacun des trous est représenté par un dipôle, tel qu'illustré à la figure 2.5. Cela permet la représentation des champs comme une somme d'interactions dipolaires dont l'espacement est donné par la périodicité du réseau.



$$p = \frac{1}{\frac{1}{\alpha_E} - G_E}$$

$$G_E = \sum_{\mathbf{R}\neq 0} (k^2 + \partial_{xx}^2) \mathrm{e}^{\mathrm{i}kR}/R$$

Figure 2.5 (a)Représentation en dipôle des réseaux de nanotrous et représentation du champ. p représente la polarisation des dipôles, α_e est la polarisabilité de la géométrie considérée, et G_E est le terme d'interaction dipolaire. Tiré de (De Abajo, 2007)

Cette méthode permet une représentation simple des équations de couplages. Elle est limitée à certaine géométries simples dont les équations de moments dipolaires sont connues, tels des cercles ou ellipses. Certaines limites, notamment du cas où la longueur d'onde est plus grande que la période du réseau, permet d'écrire les équations sous une forme analytique simple. Cette méthode a été présenté dans le papier de (De Abajo et al., 2005) et fait l'objet d'un papier de revue (De Abajo, 2007)

Ces méthodes analytiques ont fait l'objet de plusieurs papiers sur la phénoménologie de la résonance pour les réseaux de nano-trous. Elles permettent d'utiliser des équations analy-

tiques et d'associer des conditions pour les résonances. La méthode des modes couplés a été choisie simplement car elle était plus documentée et repose sur une expansion des champs électromagnétiques et à des conditions de continuité aux interfaces, ce qui correspond à une démarche classique en optique.

2.2 Analyse de l'approche au niveau de la fabrication

Les nano-trous étudiés sont de dimension nanométriques. Ces structures nécessitent donc l'utilisation de méthode de fabrication à haute résolution. Nous revoyons ici l'ensemble des méthodes de fabrication retrouvées dans la littérature afin de comparer et justifier les outils utilisés dans les publications de cette thèse.

Les caractéristiques d'intérêts pour la fabrication sont :

1. Précision à l'échelle du nanomètre
2. Uniformité au niveau de la géométrie
3. Uniformité au niveau de la périodicité
4. Possibilité de fabrication à grande échelle
5. Coût de fabrication
6. Épaisseurs possibles pour le film métallique
7. Rugosité de surface

Nous présentons ici les caractéristiques de chaque méthode. Un tableau récapitulatif permet de retrouver quelles méthodes ont été employées dans la littérature.

2.2.1 Faisceau d'ions focalisés

Le faisceau d'ions focalisés consiste en une méthode de gravure directe du motif, tel qu'illustré à la figure 2.6. Elle nécessite l'utilisation d'un appareil à colonne électronique qui peut balayer la surface de l'échantillon. La source est composée d'ions, typiquement de Gallium, qui sont accélérés vers la surface et qui pulvérisent le matériau.

Cette méthode a l'avantage de nécessiter qu'une seule étape et d'être très facile à mettre en place. Elle est un outil idéal pour tester des prototypes. Elle offre une grande résolution et une bonne régularité sur les motifs gravés. Elle est cependant la méthode la plus lente et la plus coûteuse. Elle nécessite également de faire un raccordement des fenêtres de gravure car le grossissement doit être élevée pour obtenir une bonne résolution sur les motifs.

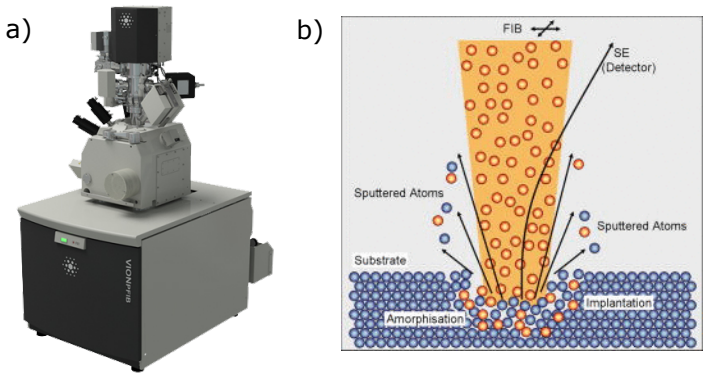


Figure 2.6 a) Station de travail du faisceau d'ions focalisés. Tiré de *FEI* b) Principe de pulvérisation de la matière. Tiré de (Utke et al., 2008)

2.2.2 Lithographie par faisceau d'électrons

Cette méthode est une méthode de lithographie avec transfert de motif. L'appareillage utilisé est également une colonne électronique qui ballait la surface de l'échantillon. Le faisceau d'électrons expose la résine et la rend soluble (résine positive) ou insoluble (résine négative). Ces étapes sont illustrées à la figure 2.7. L'étape de dissolution de la résine se nomme "développement" et se fait à l'aide d'un solvant spécifique. Une fois le motif imprimé sur la résine, un transfert de celui-ci s'opère généralement grâce à un lift-off ou une gravure.

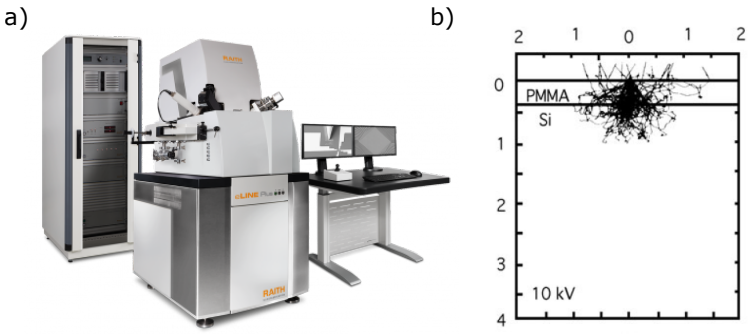


Figure 2.7 a) Station de travail de lithographie par faisceau d'électrons.Tiré de *Raith*b) Simulation Monte Carlo de l'absorption et de la diffusion des électrons à travers la résine.

Transfert par Lift-Off

Dans un transfert par lift-off, le matériau final est déposé sur la résine développée et sur le substrat, à l'intérieur des régions qui ont été développées. Un décapage de la résine permet d'enlever le matériau déposé sur la résine et ne laisse que celui sur le substrat, obtenant

ainsi un *négatif* du motif imprimé sur la résine. Pour cette méthode, une caractéristique à respecter pour obtenir de bons résultats est d'utiliser une résine au moins 3 fois plus épaisse que le matériau à déposer. Effectivement, dans le cas inverse, la déposition de matériau sur le coté des parois de la résine développée empêchera un décapage efficace de celle-ci en créant parfois une couche continue. Une méthode couramment utilisée pour améliorer l'efficacité du lift-off est d'utiliser un système de 2 résines avec la résine du dessous agissant comme couche sacrificielle pour empêcher la création de couches continues. Le principe est d'utiliser une résine qui est plus sensible ou qui se développe à l'aide d'un autre développeur. Dans le cas d'une résine positive, une méthode conventionnelle consiste à utiliser de la PMMA de longueur de chaînes polymériques différentes, ou d'utiliser le copolymère MMA-PMMA qui est lui aussi plus sensible. Une bonne référence pour cette méthode est la fiche de la résine (MicroChem, 2001). Pour une méthode utilisant une résine négative, nous proposons une recette qui a fait l'objet d'une publication dans le cadre de ce doctorat et qui est disponible dans la section 5.

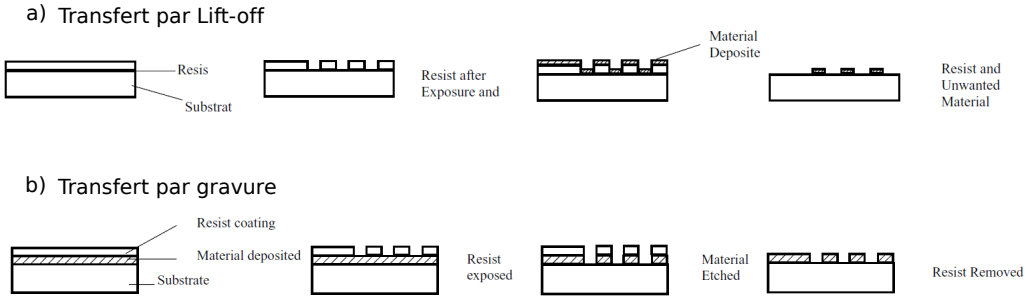


Figure 2.8 a) Procédure pour un transfert de motif par lift-off. b) Procédure pour un transfert par gravure. Tiré de (Zhou, 2005)

Les caractéristiques de cette méthode sont qu'elle permet d'obtenir une bonne verticalité et régularité des motifs. Elle est toutefois un peu plus complexe à mettre en oeuvre car elle comporte plusieurs étapes, et elle nécessite un dépôt pour chaque échantillon réalisé.

Transfert par gravure

Dans un transfert par gravure, une solution ou un plasma sont utilisés pour graver la partie du substrat qui est exposée, obtenant ainsi le positif du motif imprimé sur la résine. La résine est ensuite enlevée pour ne laisser que le matériau avec le motif. Cette méthode est généralement peu utilisée ; en effet les gravures disponibles, autant en solution qu'en plasma, sont généralement anisotropes, et ne permettent pas d'obtenir de bon contrastes de gravure matériau/résine, ce qui veut dire que les trous ne peuvent être profonds. Les deux méthodes

de transfert sont présentées a la figure 2.8.

2.2.3 Lithographie par nanoimpression

Cette méthode consiste en une lithographie à l'aide d'un moule, souvent en silicium, qui permet d'imprimer le motif sur une résine, tel qu'illustré à la figure 2.9. En appliquant de la pression et parfois de la chaleur sur la résine à partir du moule, le motif est transféré. Tout comme avec la lithographie par électron, le motif est ensuite transféré dans une étape subséquente.

L'intérêt de cette méthode est d'utiliser la grande reproductibilité de la nano-impression pour éviter d'avoir recours à l'appareillage du FIB ou EBL à chaque fois qu'un échantillon doit être fabriqué. Cela permet de réduire les coûts tout en permettant une fabrication à large échelle. Les travaux de (Skinner et al., 2008), (Henzie et al., 2007) et (Malyarchuk et al., 2005) ont permis d'élaborer la technique pour les réseaux de nano-trous.

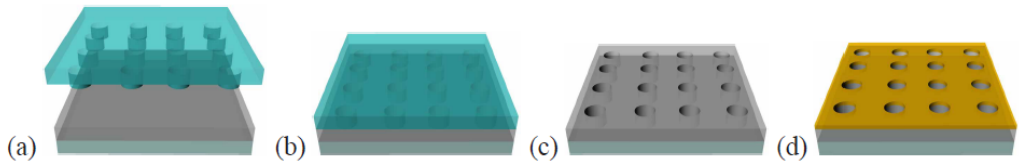


Figure 2.9 Procédure pour la lithographie par nano-impression. Tiré de (Malyarchuk et al., 2005).

2.2.4 Lithographie par nanosphère

Cette méthode, plus connue pour la fabrication de réseaux de nanoparticules sur substrat, peut également être utilisée pour la fabrication de réseaux de nano-trous sur film de métal et est présentée à la figure 2.10. Une matrice de sphères de silice est déposée par enduction centrifuge afin de créer un réseau régulier de ces sphères sur une résine. Les parties de la résine non couvertes par les sphères sont ensuite exposées et développées. Un lift-off est ensuite employé pour retrouver le négatif de la résine développée dans le dépôt métallique. Une référence utile pour cette méthode est (Wu et al., 2008). Cette technique a l'avantage d'être très peu coûteuse et assez facile d'implémentation, en plus de permettre une fabrication à grande échelle. Elle nécessite toutefois un dépôt métallique pour chaque échantillon et possède de grandes irrégularités au niveau de l'arrangement périodique puisque les sphères ne peuvent s'arranger parfaitement sur toute la surface. De plus, les trous formés peuvent également être assez irréguliers car l'exposition n'est pas très uniforme à cause de l'espacement variable des

sphères. Elle est également peu flexible au niveau de la période et de la taille des trous ainsi que de leur disposition.

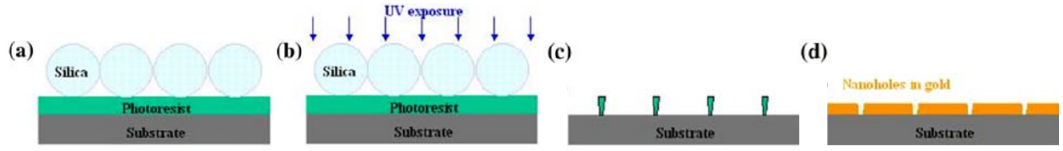


Figure 2.10 a) Procédure pour la lithographie par nano-sphère. Tiré de (Wu et al., 2008).

2.2.5 Lithographie par interférence

La lithographie par interférence est une méthode qui exploite les motifs d'interférence d'un faisceau laser afin d'en imprimer la géométrie sur une résine, tel qu'illustré à la figure 2.11. Elle nécessite uniquement un système optique relativement simple composé de deux ondes planes qui interfèrent entre elles à un certain angle grâce à un miroir. Dans cette approche, la période du réseau est donnée par $p = \lambda/2 \sin\theta$, où λ est la longueur d'onde de la source employée et θ est l'angle entre les deux faisceaux.

Cette technique a l'avantage d'être facile d'implémentation et peu coûteuse. Elle possède cependant l'inconvénient d'avoir peu de contrôle sur la disposition des trous et sur leurs géométries. Elle présente également d'importantes irrégularités au niveau de l'aspect des trous et nécessite un lift-off, ce qui implique un dépôt pour chaque échantillon.

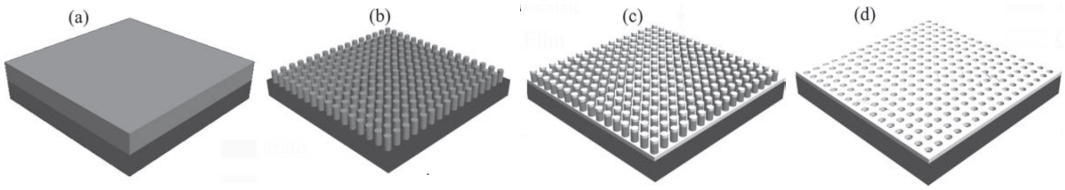


Figure 2.11 a) Procédure pour la lithographie par interférence

2.2.6 Transfert par pelage de motif

Cette méthode consiste en une autre méthode de transfert de motif à partir d'un moule, comme la technique de nano-impression. Elle n'utilise toutefois pas de résine et repose sur le principe d'extraction d'un motif déposé sur un moule, tel qu'illustré à la figure 2.12. En effet, en déposant le métal sur un substrat structuré avec des trous assez profonds, la couche de métal possédera le motif désiré. On peut relever la couche de métal en ajoutant une colle

optique ou un polymère sur la face de métal et en la pelant délicatement, puisque le métal adhérera plus à la colle qu'au substrat. La structure possède donc la rugosité de surface du substrat de silicium, qui est très faible, jusqu'à dix fois moindre qu'un dépôt conventionnel.

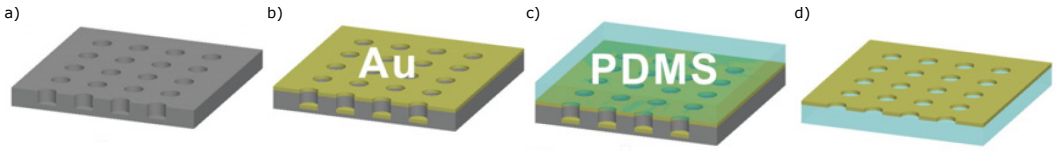


Figure 2.12 a) Procédure pour la lithographie par interférence

2.2.7 Sommaire des méthodes et comparaison

Dans le tableau 2.1 les avantages et inconvénients des différentes méthodes sont répertoriées.

Tableau 2.1 Avantages et inconvénient des différentes méthodes de fabrication

Méthode	Avantages	Inconvénients
FIB	Grande Flexibilité Une seule étape Prototypage rapide Bonne uniformités sur la géométrie	Méthode coûteuse Méthode Lente Fabrication à petite échelle Problème de raccordage des fenêtres de fabrication
EBL	Grande flexibilité Assez rapide Grande précision	Méthode coûteuse Fabrication à petite échelle Plusieurs étapes
Lithographie par Nano-Impression	Peu d'étapes Grande échelle Peu coûteux Nécessite un moule	Pas de grande flexibilité Dépôt à chaque échantillon Le substrat est la résine
Lithographie par Nano-Sphère	Grande échelle Peu d'étape Très peu coûteux Ne nécessite pas de moule	Irrégularité sur la géométrie Irrégulier sur la période Nécessite un liftoff
Lithographie par Interférence	Grande échelle Très peu coûteux Ne nécessite pas de moule	Irrégularité sur la géométrie Nécessite un liftoff
Transfert par pelage de motif	Grande échelle Peu coûteux Très petite rugosité de surface	Nécessite un moule Nécessite un dépôt

Le tableau 2.2 permet de répertorier l'ensemble des techniques utilisées pour la fabrication de noantrous dans des références qui font mention de leur utilisation comme biocapteur.

Tableau 2.2 Répertoire des méthodes employées pour la fabrication de nanotrous pour la conception de biocapteurs

Author	Year	Method	Hole size	Period	Thickness
Brolo et al	2004	FIB milling	200 nm	510-618 nm	100 nm
Tetz et al	2006	Interference litho.	200 nm	1400 nm	
Lesuffleur et al	2007	FIB milling	200 nm	600-800 nm	
de Leebeeck	2007	FIB milling	150 nm	350-850 nm	
Ji et al	2008	E-beam litho.	$150nm$	350 nm	
Lesuffleur et al	2008	FIB milling	200 nm	380-460 nm	
Hwang et al	2008	Interference litho.	300 nm	1500 nm	
Yang et al	2008	Template Striping	130-180 nm	217-540 nm	
Sharpe et al	2008	E-beam Litho.	70-200 nm	500-600 nm	40 nm
Im et al	2009	FIB milling	150 nm	390-440 nm	
Eftekari et al	2009	FIB milling FSF	250-300 nm	450-700 nm	100 nm
Yanik et al	2010	E-Beam litho. FSF	220 nm	600 nm	125 nm
de Meneze et al	2010	Interference litho.	240 nm	700 nm	100 nm
Im et al	2010	Template stripping	180nm	500 nm	100 nm
Escobedo et al	2011	FIB milling	225-275 nm	420-450 nm	100 nm
B-Dionne et al	2011	FIB milling	160 nm	380-420 nm	100 nm
Chang et al	2011	Interference Litho.	200 nm	600 nm	-
Lee et al	2012	Template stripping	30-165 nm	500 nm	100 nm
Wittenberg et al	2012	Nanoimprint Litho.	210 nm	500 nm	200 nm
Jia et al	2013	Template stripping	200 nm	600 nm	100 nm
Tellez et al	2013	Template stripping	$80nm \times 175nm$	495 nm	100nm
Zhang et al	2015	E-Beam litho.	150-235 nm	500 nm	100 nm
Barik et al	2014	Template stripping	140 nm	600 nm	100 nm
Im et al	2015	FIB	200 nm	450 nm	200 nm
Monteiro et al	2016	FIB	200 nm	400 nm	100 nm

Les motifs développés pour la conception des biocapteurs optiques reposaient généralement sur des géométries plus complexes et non régulières. Comme il sera présenté dans les chapitres suivants, des réseaux avec des périodicités diverses dans les deux axes -X et -Y sont employés. Les techniques telles la lithographie par interférence ou par lithographie par nanosphère ne cadraient donc pas avec les structures désirées. Puisque beaucoup de prototypage était nécessaire pour confectionner les structures désirées, un méthode à petite échelle et ne nécessitant pas trop d'étapes a donc été favorisée. La lithographie par électron avec lift-off a donc été mise en place. La lithographie par nano-impression a été tentée (par un stagiaire) et a permis d'obtenir de bons résultat préliminaires, mais n'a pas été employée directement

pour les échantillons testés lors de tests de détection.

CHAPITRE 3 ARTICLE 1 : SENSING WITH PERIODIC NANOHOLE ARRAY (REVUE DE LITTÉRATURE)

Ce chapitre consiste en un article de revue rédigé pour *Advances in Optics in Photonics*. Il inclue donc la revue de littérature de cette thèse. Il s'agit également d'un article qui établit une revue de la modélisation des structures d'intérêt à l'aide de la méthode des modes couplés. L'ensemble des équations est ensuite utilisé pour évaluer les performances des structures pour la biodétection, soit en mesurant leur sensibilité, leur résolution ainsi que la distribution du champ. L'analyse est effectuée sur deux grandes catégories de structure, soit des réseaux de nano-fentes 1-D et de nano-tours carrés 2-D.

3.1 Auteurs

André-Pierre Blanchard-Dionne et Michel Meunier

3.2 Introduction

When a metallic layer is perforated with periodic small indentations, its interaction with light changes greatly in comparison to what would be expected of a collection of isolated holes. At certain wavelengths which correspond to resonant conditions of the structure, impinging light is channelled inside the holes and an increase in optical transmission is observed. This behavior was identified in circular hole arrays in silver films and termed Extraordinary Optical Transmission (EOT)Ebbesen et al. (1998). Since this type of structure and its optical properties share many similarities with Surface Plasmon Resonance (SPR), the initial assumption was that Surface Plasmon Polariton (SPP) waves were responsible for the resonance Ghaemi et al. (1998). But some differences with the resonance conditions with SPPs, as well as the fact that models using a perfect electrical conductor (PEC), which cannot support SPPs, still exhibited resonance peak suggested that the resonance might be more complex. Early models using analytical methods Martin-Moreno et al. (2001) showed that the resonances could be explained in terms of diverging admittance of the modes inside the hole. More understanding of the resonant behavior was made in a paper by *Pendry et al* Pendry et al. (2004) where, in the limit of small apertures and subwavelength structures, it was shown that the structure could be described as a metamaterial with a dispersion relation reminiscent of the one of an SPP, except with its property given by the dimensions of the structure. This paper introduced the notion that resonant surface waves could be achieve due to the geometry of the

structure.

Another feature that was observe in the transmission spectrum was a sharp transmission minima, usually for wavelengths just shorter of the wavelength of maxima. This minima was identified as Wood Anomaly's Wood (1902), for which the condition, identified by Rayleigh Rayleigh (1907), happens when the diffraction order becomes grazing to the array. This condition, strictly geometrical in the case of a PEC, is slightly broaden and red-shifted when we consider a real metal since the finite dispersion and losses in the metal will change the phase velocity of the tangent surface wave Fano (1941). Since this condition coincides with the condition of excitation of an SPP on a flat surface, some authors reported that the contribution of SPPs was detrimental to the transmission Cao and Lalanne (2002); Lochbihler and Depine (2012); Lin and Roberts (2011); Lalanne et al. (2003); Crouse and Keshavareddy (2005); Xie et al. (2005).

This view has since been revised and it is now generally accepted that SPPs contribute favourably to the resonant condition Barnes et al. (2004); Liu and Lalanne (2008); Garcia-Vidal et al. (2010); Yoon et al. (2014). The complete mechanism is in fact a complicated phenomenon which relies on the multiple scattering of waves between holes Garcia-Vidal et al. (2010) and its coupling to modes inside the holes. The scattered waves propagate at the surface as what has been identified as an hybrid between an evanescent cylindrical wave and an SPP Liu and Lalanne (2008), and its character depends upon the inter-hole distance Garcia-Vidal et al. (2010). These wave are weakly coupled to a continuum in a Fano-type interaction Genet et al. (2003). It should be noted that 1-D Nanoslit arrays and 2-D Square hole arrays differ in how the wave is transmitted inside the hole, and will present different resonant feature, but both do support bound surface waves that contribute to the transmission.

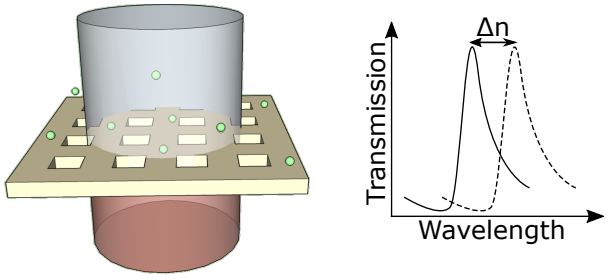


Figure 3.1 Principle of sensing with nanohole array. As molecules bind to the surface of the structure the resonant wavelength shifts and the change in intensity or of the position of the maxima is used as the signal.

One of the application that rose from this phenomenon was the sensing of analytes Brolo et al. (2004) since the resonance properties of the array depend upon the refractive index unit (RIU) of the dielectric medium around the structure. When a targeted molecule binds to the surface of the metal, the position of the maxima of the peak shifts, so the optical signal can be used to detect the presence and measure the concentration of analytes in a sample, as depicted in Fig 3.1. The usual setup for this type of sensors consists in a simple imaging system like a microscope that images the arrays and records its transmission intensity. It has gain popularity since it can achieve specific affinity sensing of label-free analytes, like SPR sensors, but with different modalities. For example, it is particularly well suited for multiplexed sensing : the small footprint of each nanohole array makes it easy to integrate many sensors on a single chip, and the normal collimation setup allows for simple optical setups that can monitor all the sensors at once Tetz et al. (2006); De Leebeeck et al. (2007); Lesuffleur et al. (2008); Im et al. (2009); Ji et al. (2008); Yang et al. (2008a). The integration with microfluidic leads to reduced analyte volume as well for high-throughput sensingDe Leebeeck et al. (2007); Eftekhari et al. (2009). High localization of the field in nanohole array is also favorable for low concentration sensing since the effect of a single molecule can be more significant if it is contained inside a region of high electric field density Lesuffleur et al. (2007). This property is also shared by Localized Surface Plasmon Sensor (LSPR), for which the low sensitivity can be balanced by an improved localized sensing of analytes Willets and Van Duyne (2007). In this tutorial article we aim at giving a complete analysis of the use of nanohole array as sensors. In the first section, a review of significant contributions is presented, with a detailed survey of the performances of the structures in terms of sensitivity and resolution. The second section describes the mathematical formalism used to describe the optical properties of the array using coupled mode theory. The next part is dedicated to an analysis of the sensing performances of both 1-D nanoslit and 2-D square nanohole arrays, which present distinct resonant features. Each structure is first presented with a perfect conductor as the metal in order to obtain some insights from the simplified equations. The consideration of finite dielectric constant for the metal is then presented and compared to the ideal case for 2 different scenario, one of a matching index substrate and one of a glass substrate. The highlights of the analysis are presented in a conclusion for each type of array. We also include in the supplementary material a MATLAB user interface Blanchard-Dionne (2017a), downloadable as a standalone application also Blanchard-Dionne (2017b), that can plot the reflection and transmission spectrum of nanoslit and square hole arrays as well as the field distribution around the structure.

3.3 Experimental results of sensing with nanohole arrays

In what follows we present a review of significant contributions to the field of sensing with nanohole arrays. Please note that other reviews of similar topics are also available at Gordon et al. (2008); Escobedo (2013); Dahlin (2015).

3.3.1 First reports of sensing with nanohole arrays

The origin of extraordinary optical transmission was first thought to be emerging from coupling of the impinging electromagnetic waves to SPPs Ghaemi et al. (1998). This finding lead to the demonstration of the ability of nanohole arrays to shift its wavelength of resonance when the refractive index of the surrounding medium was change by the addition of analytes Brolo et al. (2004). In that report by *Brolo et al*, the transmission spectrum of nanohole array functionnalized with 11-mercaptoundecanoic acid (MUA) was recorded before and after the adsorption of Bovine Serum Albumine (BSA) molecules. The results that were obtained are presented in Fig 3.2 and showed that this type of array could be used as a sensor.

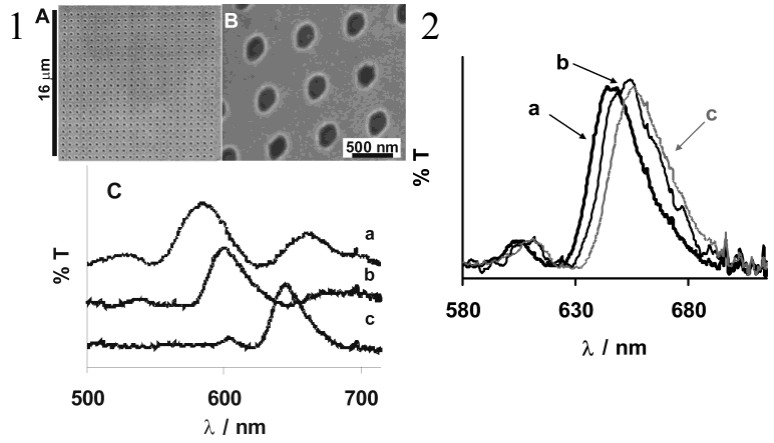


Figure 3.2 1- (A and B) Scanning electron microscopy images of a typical array of sub-wavelength holes. The image in part B is an enlargement of the array presented in part A. (C) Normalized transmission spectra of white light through three arrays of sub-wavelength holes. All arrays were patterned in a 100-nm-thick gold film deposited on the glass slide, and the diameters of the holes were about 200 nm. The lattice parameters (periodicities) of arrays a-c were 618, 545, and 590 nm, respectively. 2- Normalized transmission spectra of normally incident white light through an array of sub-wavelength (200 nm diameter) holes on a 100-nm-thick gold substrate deposited on a glass slide. (a) Bare (clean) Au surface ; (b) Au modified with a monolayer of MUA ; (c) Au-MUA modified with BSA. Reprinted with permission from Brolo et al. (2004). Copyright 2004 American Chemical Society.

Nanohole arrays benefit from the small footprint of the sensor area which is an important

advantage for the miniaturization of this type of sensing device. In order to integrate such samples into a sensing platform, the delivery of sample solution must be independent for each array or series of array. For this reason this is usually achieved using microfluidics, which allows delivery of different solutions for sensors sometimes spaced apart by only tens of microns. Such a setup was presented by *de Leebeck et al* De Leebeeck et al. (2007) who achieved delivery of solutions to 6 parallel sensors. A sensitivity of $333nm/RIU$ of the nanohole array was recorded for resonant wavelength around $670nm$. The original studies were made on circular nanohole arrays but EOT had been reported for many different shape of holes, notably in 1-D nanoslit arrays Pang et al. (2007). The use of such structure for sensing was reported by *Lee et al* Lee et al. (2009), who compared the sensing performances of nanohole array and nanoslit arrays (Fig 3.3). The authors concluded that the nanoslit array offered a better sensitivity ($3800\%/RIU$ vs $1800\%/RIU$) and overall better Full Width at Half Maximum (FWHM) of the sensing peak. The array was then used to demonstrate thin layer detection of anti-BSA at a resolution of $83.3pM$.

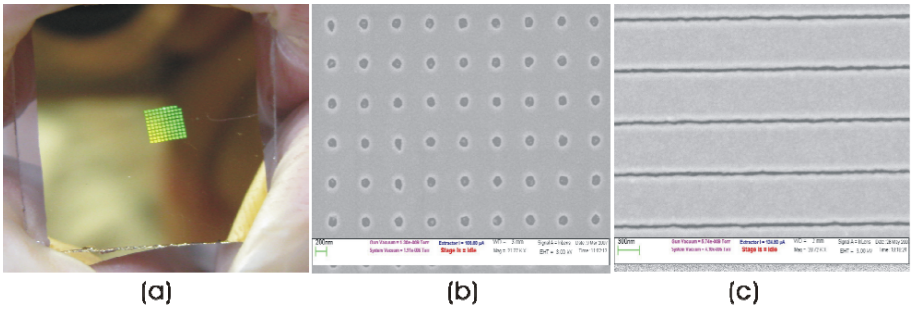


Figure 3.3 (a) The optical image of a 10×10 microarray on a glass slide (b) The SEM image of a 600nm-period gold nanohole array. (c) The SEM image of a 600nm - period gold nanoslit array. Reprinted with permission from Lee et al. (2009). Copyright 2009 Optical Society of America.

3.3.2 Resolution Improvement Methods

While the multiplexing capability of nanohole arrays offered clear advantages for high-throughput sensors, the sensing performances reported by early papers were always low compared to performances achieved by SPR sensors based on the Kretschmann configuration Piliarik and Homola (2009). Resolution improvement methods are thus an important aspect to develop for this type of sensor in order to compete with other widespread technologies and to be able to achieve detection of small concentrations of analytes. In an interesting experimental approach by *Tetz et al* Tetz et al. (2006), crossed polarizers were used before and after the transmission of light through a nanohole array of period of $1400nm$, see in Fig

3.4. They observed a change in the shape of the resonant peak from a Fano to a Lorentzian peak, which is link to the suppression of the background contribution (non resonant) of the transmission. This approach lead to an improvement of the resolution of the peak and overall improvement of the sensing performances, which was evaluated at $5 \times 10^{-6} RIU$ from the noise level and sensitivity of the sensor. In a subsequent paper by the same group Hwang

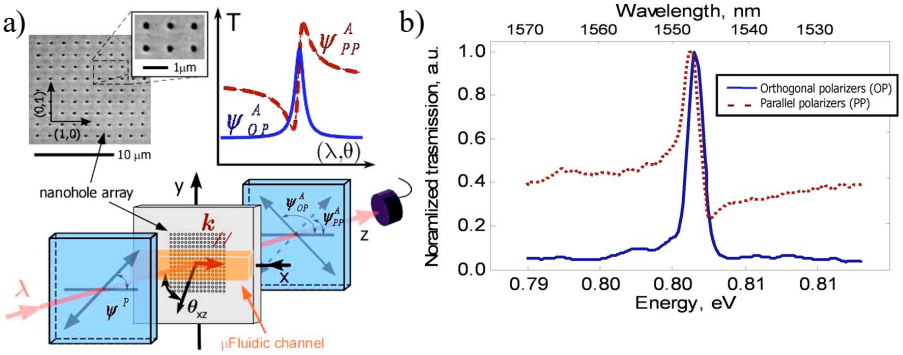


Figure 3.4 1-Conceptual diagram of the 2-D nanohole-array-based SPR sensor. The input and output polarization states of a tunable laser are controlled, providing variable spectral or angular Fano-type profiles. A microfluidic channel is used to transport the analyte fluid to the surface of the sensing area and can be used to control the refractive index on the metal-dielectric interface to tune the SPP resonance frequency. Also shown is a scanning electron microscopy image of a representative sample. 2-Normalized transmission as a function of a) energy (wavelength). Reprinted with permission from Tetz et al. (2006). Copyright 2006 Optical Society of America.

et al. (2008), the wavelength interrogation of the hole array of $\approx 1500nm$ period led to a sensitivity of $1520nm/RIU$, for which the authors concluded a possible $6.6 \times 10^{-5} RIU$ resolution. The setup was then used to demonstrate the detection of a model receptor molecule and analyte pair for *E. Coli* which consists of Ovomucoid molecule receptors with conconavalin A carbohydrate-binding lectin, for which a concentration limit of $143\mu g/mL$ was achieved.

As one of the main attract for using nanoholes as sensor resides in its integration into Lab-on-a-Chip devices, packing density of the nanohole array became one important issue to address. A paper by Przybilla et al. (2008) demonstrated a strong broadening of the resonant peak when the number of holes becomes smaller than a certain threshold. In order to circumvent this issue an interesting structure of nanohole arrays flanked by bragg mirrors in the form of periodic trenches was presented by *Lindquist et al* Lindquist et al. (2009). This setup allowed to isolate the surface modes around the holes and to reduce the effect of having a limited number of holes.

In a paper by *Lesuffleur et al* Lesuffleur et al. (2007), circular double-holes were used. While

the shape of the hole plays a role in the coupling coefficient between the surface modes and the propagative modes inside the holes, an improvement in sensitivity compared to the *Brolo et al* article Brolo et al. (2004) was wrongly attributed to the shape of the holes while it is more believable that it was due a the longer period of the array (see next Sections). A 2% BSA solution was also used to demonstrate the ability of the array to detect thin films. Another method commonly used in SPR sensing is the use of nanoparticles to enhance the signal of low concentration analytes. This was done on nanohole arrays by *Sharpe et al* Sharpe et al. (2008) in a setup where nanoparticles were used to increase the response of monoclonal antibodies, and a 3-fold enhancement was observed. A similar approach was used in a paper by *Wang et al* Wang et al. (2014), but instead of increasing the peak shift of the array by using nanoparticles, they used an enzymatic reaction that precipitates silver agglomerate inside the holes, blocking their transmission. This technique achieved a detection limit of $0.1 ng/mL$ of biotinylated hen egg lysozomes.

Another method for improving the performances of the array made use of its 2-D nature. In a paper by *Blanchard-Dionne et al* Blanchard-Dionne et al. (2011) a nanohole array with different periodicities in the -x and -y axis was used to increase the performance by using the different polarization measurements as the sensing signal. The signal consisted in the differential transmission from -x and -y polarizations, which doubled the sensitivity and reduced spurious noise. A 5-fold improvement was noted using this setup compared to a regular transmission measurement. Another approach to improve the resolution of the sensor was done using a dual wavelength detection system. The setup used by *Escobedo et al* Escobedo et al. (2011) was a fully integrated and compact system that uses the differential signal of a 565 nm LED and a 660 nm LED as the sensing signal. A resolution of 6×10^{-4} RIU was demonstrated and the system was used for biotin-streptavidin binding experiments and showed a 2 μM detection limit. A similar approach of using two wavelengths on two different arrays and to use the differential signal was made by *Chang et al* Chang et al. (2011). The authors measured a 30 fold improvement of the resolution of the system using this approach. Another group has shown resolution improvement using the multispectral integration method Lee and Wei (2010), a method making use of the integration of the sensing signal for all wavelengths. They observed great noise reduction and achieved a resolution of $3.3 \times 10^{-5} RIU$. Another approach made by *de Menezes et al* de Menezes et al. (2015) demonstrated that the collimation angle can influence the performances of the sensors. The group tuned the collection angle to the optimal angle for maximum sensitivity, which was shown to improve of a factor 3.5 when changed from 2.3 to 25.4 degrees. A paper by *Cetin et al*Cetin et al. (2015) showed the influence of the resonant states of the substrate on the resonant peaks of the medium interface. They demonstrated how the obstruction of a resonant peak can alter

other resonant feature and improve the limit of detection to $1 \times 10^{-5} RIU$.

3.3.3 Report of multiplexed detection

One of the big interest in using nanohole arrays for sensors is the integration of multiple sensors on one chip and the achievement of multiplexed detection. Such a setup was demonstrated by *de Leebeck* De Leebeeck et al. (2007) for the detection of biotin-streptavidin complexes. A sensor chip was incorporated in a microscope setup linked to a spectrometer and the wavelength maxima were used to obtain a sensing signal. In another setup by *Lesuffleur* Lesuffleur et al. (2008), several sensors were incorporated on a chip illuminated by an He-Ne laser for the detection of self-assembled monolayer of alkanethiolates. The design demonstrated a $16000\%/RIU$ intensity sensitivity. The setup they used is presented in Fig 3.5.

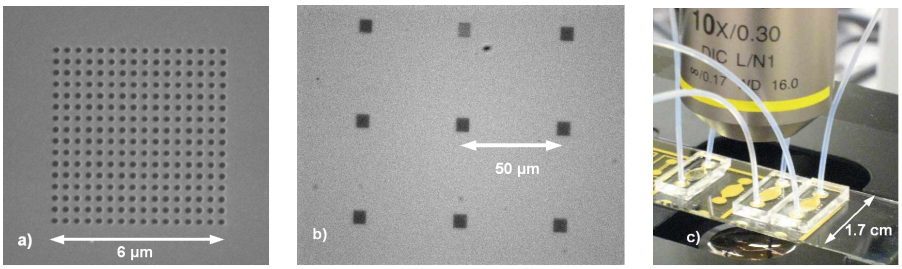


Figure 3.5 1.a) Scanning electron microscopy (SEM) image of a 16×16 nanohole array with a 200 nm hole size and 380 nm periodicity. b) A bright-field microscope image of 5×3 microarray of nanohole arrays (partially shown). Each sensing element, a 16×16 nanoholes array as in (a), is separated by $50\mu m$. c) The PDMS chip, shown with microfluidic flow cells and tubing. Reprinted with permission from Lesuffleur et al. (2008). Copyright 2008 Optical Society of America.

In an article by *Im et al* Im et al. (2009) it was pointed out that spurious noise can emerge from the absorption of light in the sample liquid or from the bulk refractive index from the sample solution. The signal from an array which is not functionalized with receptors can help reject this type of noise. In an article by *Ji et al* Ji et al. (2008), a setup with 25 simultaneous sensors monitoring the binding events of anti-GST antibodies was demonstrated. A high packing density setup using $10x10$ nanohole array using a 635 nm laser diode helped to achieve this result, for which a resolution of $13mM$ anti-GST was demonstrated. Still by the same group Yang et al. (2008a) another setup using an index matching substrate of fluorinated ethylene propylene (FEP) was used to enhanced the transmitted intensity. The authors although observed a decrease in sensing performances. Repeated sensing cycles of the same anti-GST was used to demonstrate the association constant of the GST-antiGST

complex, which they reported as being coherent with typical BIAcore reported measurements. Another group demonstrated the utility of multiplexed sensing by selectively applying voltage to the surface of the array in order to functionnalized them for different gas Wright et al. (2012). They were able to detect dimethylmethyl phosphonate and to clearly distinguish it from the hydrogen control.

3.3.4 Improvement in surface roughness

Surface roughness is critical for achieving high quality factors of the resonance peak by reducing radiative losses. Many authors explored different fabrication methods to improve the quality of the surface. In a paper by *Zhang et al* Zhang et al. (2015), a nanohole array was built using an e-beam lithography double lift-off process with annealing to improve the surface roughness of the hole array. The RMS surface roughness was improved from 1.89 to 0.87 nm which resulted in a near 3 times improvement of the resolution. Another popular method to improve the surface quality of the array is to use template stripping. The metal is deposited on a patterned silicon wafer and then stripped using a cured substrate. This way, the smoothness of the silicon master can be retained for the nanohole array. A setup by *Im et al* Im et al. (2011) used this method to achieve large-scale nanohole arrays by using multiple times the same silicon master. The arrays were made of silver with a 1-2 nm square mean root value for roughness with a 15nm silica coating to prevent from oxidation. Another report of template stripping, this time with nanoslit arrays, was provided by *Lee et al* Lee et al. (2012). The nanoslit were described as improving the sensing performances because they can reach very low width of the resonant peak. Template stripping has also been used by *Jia et al* Jia et al. (2013) using PDMS as the substrate. The team showed that contact binding improved the performance of the sensor compared to cured PDMS, which they owe to the negative effect of the presence of PDMS inside the hole and near the surface. They were able to detect troponin protein, a marker a myocardiac infarction, down to a concentration 0.4 nM. In a paper by *Tellez et al* Tellez et al. (2013) the stripping fabrication technique was used to built elliptical holes. The combination of index matching substrate along with improve resolution of elliptical holes and low surface roughness (RMS of 0.2 nm) allowed for improved resolution below $1 \times 10^{-7} RIU$.

3.3.5 Delivery of analytes towards the surface

Most of the sensors using nanohole arrays for multiplexed sensing are integrated with microfluidic. Such a small-scale fluidic device exhibits laminar flow Escobedo et al. (2010); Yanik et al. (2010), for which lateral diffusion can be very small and constitute a problem for ade-

quate delivery of the analyte towards the surface where the sensing occurs. A way to avoid this problem is to use the nanoholes as nanochannels. A first group to demonstrate this integrated setup, *Eftekhari et al* Eftekhari et al. (2009), were able to do so by milling holes on a gold film standing on a Silicon Nitride membrane (Si_3N_4), see in Fig 3.6. They showed an improvement of 6-fold for the kinetics of analytes delivery by passing the solution inside the nanoholes instead of simply over them. This sensor was also able to demonstrate thin layer sensing of cancer marker antibodies PAX8. The group also demonstrated the efficiency of the approach via numerical simulations in order to understand the effect of the delivery towards the surface in a case of binding kinetics experiments Escobedo et al. (2010). Using common diffusive constant of small analytes they were able to demonstrate a minimum of 10 fold improvement in terms of response time. *Yanik et al* Yanik et al. (2010) also demonstrated a

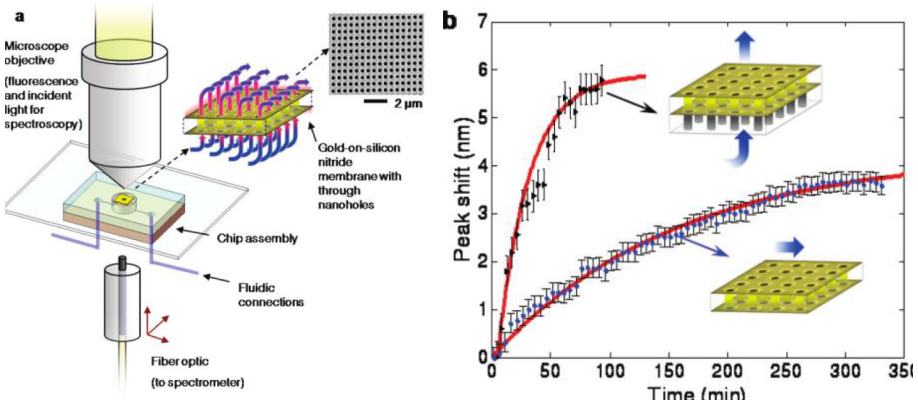


Figure 3.6 Flow-through nanohole arrays. (a) Schematic of the optical and fluidic test setup employed for both fluorescence tests and transmission spectroscopy. (b) comparison of response to surface adsorption achieved with flow-over and flow-through formats as indicated inset. Measured peak shift (625 nm peak) is plotted as a function of time during flow through/over of an ethanol/MUA solution. As indicated in the inset, the flow-through sensor is operated with flow from the nonparticipating silicon nitride side to the active gold surface. The flow-through case results in a characteristic rate constant of k_{abs}) $3.8 \times 10^{-2} min^{-1}$ as compared to k_{abs}) $6.4 \times 10^{-3} min^{-1}$ for the flow-over case. Adapted with permission from Eftekhari et al. (2009). Copyright 2009 American Chemical Society.

flow-through setup using an etched Si_3N_4 free standing film with gold as the metallic layer. Their experimental results, supported by finite-element simulations, demonstrated a 14-fold improvement in mass transportation constant towards the surface. The same group further analyzed the mass transportation problem in a subsequent paper Huang et al. (2013) and a demonstration of the approach was given for virus-like analytes. Another method reported by *Barik et al* Barik et al. (2014) used dielectrophoresis to attract the particles towards the surface. The group demonstrated the role of the electric field gradient induced by the hole

which is crucial to generate an electro-osmosis force to trap the molecule on the surface. They used BSA concentrations to demonstrate the efficiency of their approach for small molecule sensing. The technique showed that for low concentrations, the diffusion time to record surface coverage of the molecule was in some cases 1000 times faster.

3.3.6 Fully integrated systems

The attract of nanohole array for sensing resides in their potential for fast and high-throughput sensing devices. The integration of all the optical, sensing and signal detection components into a compact design thus constitutes a very appealing equipment for medical diagnostics. A first step in that direction was given by *Guyot et al* Guyot et al. (2011) who was able to integrate the sensor onto a silicon substrate which acted as a MOS detector. A more complete integrated system was presented by Escobedo et al. (2011) who developed a hand-held device which incorporated a LED, array and detector. Another demonstration of a fully integrated system was done by *Cetin et al* Cetin et al. (2014) who developed a lens-free sensing system using the image of the diffraction of nanohole array on a CMOS camera $1mm$ away (Fig 3.7a). This design allows to follow individually the intensity measurements of each sensor by differentiating the intensity for each sensor independently via an image reconstruction algorithm. The system was able to achieve detection of IgG antibodies at a concentration of few $\mu g/mL$, although without a dynamic scan. The same setup, using a dual wavelength source, was also reported by the group Coskun et al. (2014). Another demonstration of the integration of the nanohole array on the sensing device was provided by *Seiler et al* Seiler et al. (2016) who integrated a nanohole array sensor in the close vicinity of a CMOS sensor chip. By using diffraction from the hole array, the authors were able to demonstrate the detection of the full spectrum of the transmitted light directly on the camera. In a recent demonstration of nanohole array as a diagnostic tool for biomedical application, *Im et al* Im et al. (2014) reported the full study of ovarian cancer markers using a compact device that integrated the light source, nanohole array and detector inside a microscope setup. The apparatus is presented in Fig 3.7b). The wavelength of operation was tuned for an increased sensitivity according to the size of the analyte.

3.3.7 Nanohole array as a diagnostic tool

The high-throughput of the nanohole sensor array is a great advantage for situations where multiple analytes must be detected. This way, complete profiles of disease markers can efficiently be achieved in a quick and costless method that requires low sample volumes. The work presented previously by *Jia et al* Jia et al. (2013) has shown detection of cardiac

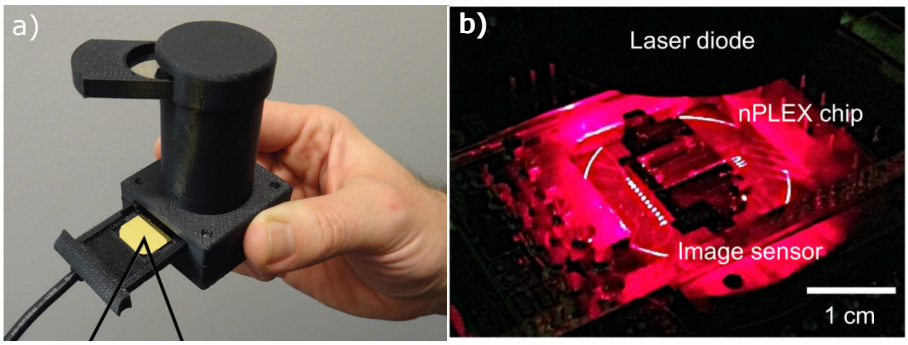


Figure 3.7 a) Real picture of the portable biosensing device, weighing 60 g and 7.5 cm tall designed for point-of-care applications. In the picture, the hand of the author highlights the compactness of the device. Reprinted with permission from Cetin et al. (2014). Copyright 2014 Nature Publishing Group. b) A prototype miniaturized nPLEX imaging system developed for multiplexed and high throughput analysis of exosomes. The system uses a complementary-metal-oxide semiconductor (CMOS) imager to record the transmitted light intensity from a nPLEX chip. Reprinted with permission from Im et al. (2014). Copyright 2014 Nature Publishing Group.

troponin-I analytes, which are a marker of myocardial infarction. The nPLEX integrated system presented in the previous section was used to determine the potential of exosomes towards the diagnostic of cancer Im et al. (2014), with their results presented in Fig 3.8. The group was able to determine that surface proteins CD24 and EpCAM can be used as markers for the detection of ovarian cancer cells. The studies of *Wittenberg et al* Wittenberg et al. (2012) helped determine the affinity of antibodies to myelin receptors in order to determine their possible role in signaling neural damage for the diagnostic of multiple sclerosis. The nanohole in this case had the advantage of exposing silica inside the holes, which helps the formation of supported lipidic bilayers. Another demonstration of diagnostic applications of nanohole arrays was realized by *Monteiro et al* for the study of breast cancer biomarkers HER2-positive Monteiro et al. (2016). Recently nanohole array assays have been used to detect sexually transmitted infections *Chlamydia trachomatis* and *Neisseria gonorrhoeae* to detection limits of 300 and 1500 CFU/mL, respectively Soler et al. (2017). Another publication demonstrated the utility of the real-time sensing of this type of device by measuring cell secretions Li et al. (2017). This monitoring of cells can help understand the processes and possible treatments of diseases.

3.3.8 Survey of the performances of nanohole array sensors

A complete table that summarizes the performances of nanohole and nanoslit arrays is presented in Table 3.1. The type of structure is given as well as, when available, the sensitivity

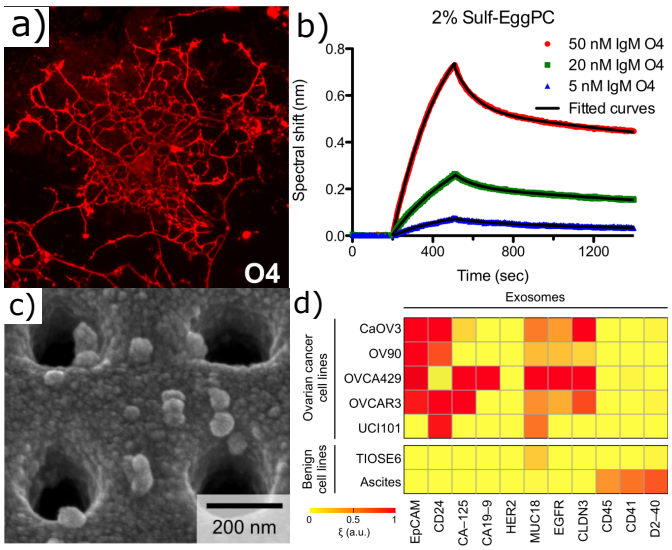


Figure 3.8 a)An example of antibody O4 binding to the surface of a live immature rat oligodendrocyte b) SPR kinetic curves for IgM autoantibodies binding to SLBs. (a) O4 binding to SLBs containing 2% Sulf. Reprinted with permission from Wittenberg et al. (2012). Copyright 2012 American Chemical Society. c) SEM indicates specific exosome capture by functionalized nPLEX d)Putative ovarian cancer markers (EpCAM, CD24, CA19-9, CLDN3, CA-125, MUC18, EGFR, HER2), immune host cell markers (CD41, CD45) and a mesothelial marker (D2-40) were profiled on exosomes (b, using nPLEX sensor). Reprinted with permission from Im et al. (2014). Copyright 2014 Nature Publishing Group.

and working wavelength of the setup. The resolution is given either in terms of the smallest refractive index unit change distinguishable by the system, or the smallest concentration of the analytes that was measured in a real type assay.

3.4 Performances of nanohole array sensors

In this article we aim at presenting in details a mathematical formalism in order to describe the sensing performances of nanohole arrays. Sensitivity, resolution and field distribution are presented. We describe in this section the metrics used in order to do so. Sensitivity is defined as the rate of change of the sensing parameters as a function of the refractive index. For a wavelength interrogation or intensity interrogation setup this will be represented by the derivative of the wavelength of resonance as a function of refractive index :

$$Sensitivity = \frac{d\lambda_r}{dn} \tag{3.1}$$

For sensing purposes, the quality factor of the resonance peak must also be considered in order to describe the precision at which we can define a resonant maxima. We use the metric of resolution for this purpose :

$$Resolution = \frac{FWHM}{sensitivity \cdot depth} \tag{3.2}$$

Resolution can also be viewed as the inverse of the sensitivity of the array multiplied by the slope of the peak, which is the rate of change of the effective sensing signal in an experiment that uses intensity changes at a fixed wavelength. The definition of these sensing parameters is illustrated in Fig 3.9a).

When considering sensing applications, the distribution of the fields at the surface must also be considered since changes in refractive index will only be effective if they occur in a region of strong field confinement. We thus define the other metrics of surface sensitivity and layer sensitivity which weights the sensitivity for changes of refractive index at the surface or inside a defined region near the surface (see Fig 3.9b).) For the field distribution analysis we use a modified waveguide perturbation theory to assess the change in propagation constant that depends on refractive index change in the medium as discussed in Yang et al. (2015) :

$$\frac{\widetilde{\omega} - \widetilde{\omega_0}}{\widetilde{\omega_0}} \approx \frac{\int\int\int \Delta\epsilon E_0^2 dV}{\int\int\int \epsilon E_0^2 dV} \tag{3.3}$$

where ω_0 is the angular frequency at resonance before the perturbation and ω the one of the

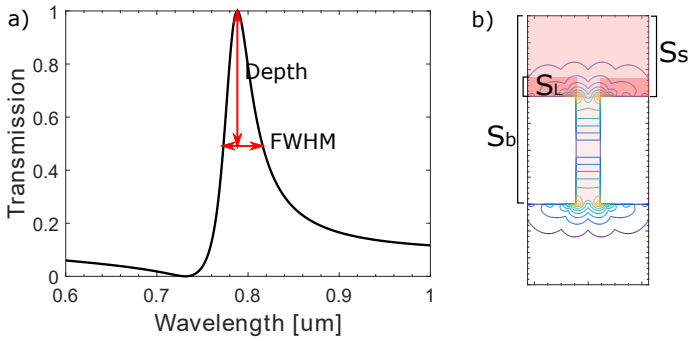


Figure 3.9 a) Definition of the Full Width at Half Maximum (FWHM) and depth of the resonant peak. b) Definition of the different sensitivities used in this article : bulk sensitivity (S_b) is relative to a change of refractive index in medium 1 and 2, surface sensitivity S_s is relative to a change if refractive index in medium 1 only and the layer sensitivity S_l is relative to a change of refractive index occurring in a layer of thickness L at the surface of the structure. These section define the volume of the field integral involved in Eq 3.3

Tableau 3.1 – Sensitivity and resolution of nanohole array

Author[ref] Year	Structure	Sensitivity	λ	Resolution
Brolo et al. (2004) 2004	Circ. Hole	400 nm/RIU	633 nm	-
Tetz et al. (2006) 2006	Circ. Hole	1022 nm/RIU	1550 nm	est. $5 \cdot 10^{-6}$ RIU
Lesuffleur et al. (2007) 2007	Circ. Double-Hole	600 nm/RIU	$\approx$ 850 nm	2% BSA
De Leebeeck et al. (2007) 2007	Circ. Hole	333 nm/RIU	$\approx 680nm$	-
Hwang et al. (2008) 2008	Circ. Hole	1520 nm/RIU	1540 nm	$6.6 \cdot 10^{-5} RIU$
Lesuffleur et al. (2008) 2008	Circ. Hole	16600 %/RIU	$380nm$	2% BSA
Im et al. (2009) 2009	Circ. Hole	-		20mM Strep.
Ji et al. (2008) 2008	Circ. Hole	-	635 nm	13 nM anti-GST Ab
Yang et al. (2008a) 2008	Circ. hole	323 nm/RIU	600nm	10 nM anti-GST Ab
Sharpe et al. (2008) 2008	Circ. hole	393 nm/RIU	$\approx 1000nm$	-

Lee et al. (2009) 2009	Slit	575 nm/RIU - 3800%/RIU	$800nm$	83.3pM anti-BSA
" "	Circ. hole	1800 %/RIU	$800nm$	-
Eftekhari et al. (2009) 2009	Circ. hole FSF	324 nm/RIU	$\approx 600nm$	-
Yanik et al. (2010) 2010	Circ. hole FSF	630 nm/RIU	$889nm$	-
de Menezes et al. (2015) 2010	Circ. hole	271 nm/RIU	750 nm	-
Lee and Wei (2010) 2010	Slit	$\approx 600nm/RIU$	$\approx 750nm$	$3.3 \cdot 10^{-5}$ RIU
Im et al. (2011) 2011	Circ. Hole	450nm/RIU	$\approx 660nm$	$2 \cdot 10^{-5}$ RIU
Blanchard-Dionne et al. (2011) 2011	Circ. hole	396 nm/RIU - 2900%/RIU	$632.8nm$	$6.4 \cdot 10^{-6}$ RIU
Escobedo et al. (2011) 2011	Circ. hole	-	≈ 600 nm	$6.4 \cdot 10^{-4}$ RIU
Chang et al. (2011) 2011	Circ. holes	615 nm/RIU	$\approx 900nm$	$10\mu l/ml$ IgG
Lee et al. (2012) 2012	Slit	$10367\%/RIU$ - 427nm/RIU	694 nm	$1.93 \cdot 10^{-5}$
Jia et al. (2013) 2013	Circ. Hole	522 nm/RIU	750 nm	2×10^{-5} - 0.4 nM cTnI
Tellez et al. (2013) 2013	Elliptical holes	$1.67 \cdot 10^{5}\%/RIU$	655 nm	$0.9 \cdot 10^{-7}$ RIU
Barik et al. (2014) 2014	Circ. Hole	-	838 nm	1pM BSA
Cetin et al. (2014) 2014	Circ. Hole FSF	-	680 nm	3.9 μm/mL IgG
Im et al. (2014) 2014	Circ. Hole	-	638 nm	670 aM exosomes
Cetin et al. (2015) 2015	Circ. Hole		650 nm	$2 \cdot 10^{-5} RIU$
Monteiro et al. (2016) 2016	Circ. Hole	302 nm/RIU	$\approx 650nm$	30 nG/mL
Seiler et al. (2016) 2016	Circ. Hole	-	$\approx 600nm$	$5 \cdot 10^{-4} RIU$

Soler et al. (2017) 2017	Circ. Hole	600 nm/RIU	850 nm	300 CFU/mL CT 1500CFU/mL NG
Li et al. (2017) 2017	Circ. Hole	-	850 nm	145pg/mL VEFG

perturbed waveguide. The sensitivity of the array can thus be weighted by this field volume integral in order to obtain the surface sensitivity for example, as illustrated in Fig 3.9b).

3.5 Coupled mode theory

In this section we review the formalism of Coupled Mode theory (CMT) in the multiple scattering formalism, for which many good tutorial papers and reviews are available Martin-Moreno et al. (2001); Garcia-Vidal et al. (2005); Garcia-Vidal and Martin-Moreno (2002); Martín-Moreno and García-Vidal (2008); de León-Pérez et al. (2008); Garcia-Vidal et al. (2010), in order to obtain the optical properties of the studied structures. We use of the periodicity of the system by introducing a unit cell representation given in Fig 3.10

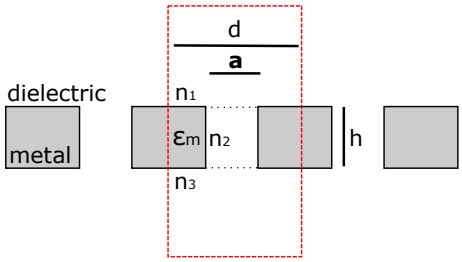


Figure 3.10 a) A schematic representation of a unit cell of a periodic nanoslit (or square nanohole) array

The fields are defined inside a single unit cell by using an expansion into the possible diffracted components, which corresponds to Bloch modes. Inside the holes, the fields are expanded into the guided modes. In Fig 3.11, the electric fields are written using the braket convention presented in a previous paper Garcia-Vidal et al. (2010). Since the fields are considered solely as guided modes inside the indentation, we neglect in this method any direct transmission through the metal. The model is thus valid for optically thick metal structures, which is normally the case of interest when studying EOT.

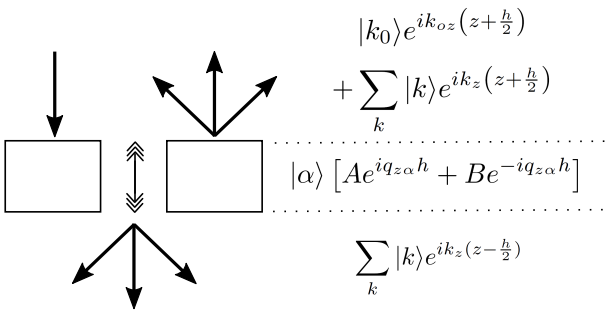


Figure 3.11 Electric field definition for each medium of the structure. Tangential part of the fields are contained in the braket factor. The fields in region 1 and 3 are represented as a sum of diffracted plane waves, while in region 2 the fields are given by the waveguide mode, which depends on the geometry.

3.5.1 Field Equations

The fields are defined as free plane wave in medium 1 and 3 and as guided waves in medium 2 (inside the indentation), see Fig 3.11. The tangential components of the fields are included in the braket notation while components parallel to the propagation direction are presented with their exponential propagating factor. We choose the axis $\hat{\mathbf{x}}$ to represent the incoming incident p-polarization.

Plane waves in Region 1 and 3

In Fig 3.11 the field of the incident wave with wavevector $k_0 = k_w sin(\theta)$ and the multiple reflected fields are represented with the factors :

$$|k_o\rangle = C_k e^{ik_0 r}\hat{\mathbf{x}} \qquad |k\rangle = [C_{kx}\hat{\mathbf{x}} + C_{ky}\hat{\mathbf{y}}]e^{i\vec{k}\vec{r}} \tag{3.4}$$

The wavevectors can take value of

$$\vec{k} = \left(k_w sin\theta + \frac{m_x 2\pi}{d}\right)\hat{\mathbf{x}} \tag{3.5}$$

for the case of 1-D slit arrays and

$$\vec{k} = \left(k_w sin\theta + \frac{m_x 2\pi}{d}\right)\hat{\mathbf{x}} + \frac{m_y 2\pi}{d}\hat{\mathbf{y}} \tag{3.6}$$

for the 2-D nanohole array case, where m_x and m_y are integers relative to the diffraction order and θ is the incident angle. The term C_k is a normalization factor which takes the value $C_k = \frac{1}{\sqrt{d}}$ in 1-D and $C_{kx} = \frac{k_x}{|k|^2 d}$ and $C_{ky} = \frac{k_y}{|k|^2 d}$ in 2-D for the p-polarization and$C_{kx} = \frac{-k_y}{|k|^2 d}$

and $C_{ky} = \frac{k_x}{|k|^2 d}$ for the s-polarization.

Guided waves in Region 2 - Case PEC

Waves inside the holes are represented by their modal expression of the corresponding waveguide type. For 1-D slit array the interesting case will correspond to the TM modes of a parallel plates waveguide. The normalized equations for these modes are given by :

$$|\alpha\rangle = \frac{C_\alpha}{\sqrt{a}} cos(\frac{b\pi}{a}(x + \frac{a}{2}))\hat{\mathbf{x}} \tag{3.7}$$

where b is an integer that represents the mode number ad C_α is a constant that will equal 1 if $b = 0$ and $\sqrt{2}$ otherwise. The propagation constant inside the hole is given by :

$$q_{z\alpha} = \sqrt{k_w^2 \epsilon_2 - (b\pi/a)^2} \tag{3.8}$$

A fundamental characteristic of parallel plate waveguides is that a propagative TEM mode with coefficient $b = 0$ and propagation constant equal to $q_z = k_w\sqrt{\epsilon_2}$ has no cut-off and will constitute the leading contribution to the transmission.

For the 2-D case of rectangular waveguide we must consider both TE and TM modes, for which the tangential part of the field are equal to :

$$|\alpha\rangle = C_\alpha \left[C_{qx} sin\left(q_y(y + \frac{a}{2})\right) cos\left(q_x(x + \frac{a}{2})\right)\hat{\mathbf{x}} + C_{qy} sin\left(q_x(x + \frac{a}{2})\right) cos\left(q_y(y + \frac{a}{2})\right)\hat{\mathbf{y}} \right] \tag{3.9}$$

where $q_x = b_x\pi/a$, $q_y = b_y\pi/a$ and b_x, b_y are integers relative to the mode, $C_\alpha = \sqrt{2}/a$ and for the fundamental TE_{10} mode and $2/a$ for all other modes. $C_{qx} = \frac{q_y}{\sqrt{q_x^2+q_y^2}}$ and $C_{qy} = -\frac{q_x}{\sqrt{q_x^2+q_y^2}}$ for TE modes and $C_{qx} = \frac{q_x}{\sqrt{q_x^2+q_y^2}}$ and $C_{qy}\frac{q_y}{\sqrt{q_x^2+q_y^2}}$ for TM modes.

For the TE case the mode number must respect $b_y \geq 1$ only while for TM modes it must respect $b_x \geq 1$ and $b_y \geq 1$. The propagation constant is equal to :

$$q_z = \sqrt{(n_2 k_w)^2 - (\frac{b_x\pi}{a})^2 - (\frac{b_y\pi}{a})^2} \tag{3.10}$$

for a 2-D square hole array. In the case of 2-D Square hole array the fundamental TE_{10} will be propagative only if $\lambda < n_2 a/2$.

Guided waves in Region 2 - Real metal

When considering the case of a real metal, an appropriate evaluation of the propagation constants must be made. Indeed, field penetration in the waveguide's wall will lead to an increase in the cutoff frequency compared to the perfect conductor case, as well as the attribution of an imaginary part to the propagation constant in order to account for losses (see Fig 3.12b)). Furthermore, when considering TM modes of a parallel plate waveguide, the interaction of SPPs excited on the waveguide's interface becomes significant when the hole opening is small, which modifies even more the propagation constant Gordon and Brolo (2005); Collin et al. (2007). In such a case the propagation constant will be describe by the characteristic equation for the TM modes of parallel plate waveguide :

$$tanh(\frac{a}{2}\sqrt{q_z^2 - k_w^2\epsilon_2} - ib\frac{\pi}{2}) + \frac{\epsilon_2\sqrt{q_z^2 - k_w^2\epsilon_m}}{\epsilon_m\sqrt{q_z^2 - k_w^2\epsilon_2}} = 0 \tag{3.11}$$

These equations must be solved numerically, for example by a Nelder-Mead algorithm Dionne et al. (2006), in order to retrieve the complex propagation constant q_z. This operation is computationally costly, but, as pointed out by *Collin et al* Collin et al. (2007), an analytical approximation can be used for the fundamental mode by taking the first order approximation to the *tanh* function in order to obtain :

$$q_z = k_w\sqrt{\epsilon_2}\left(1 + \frac{2k_w}{\sqrt{-\epsilon_m}}\sqrt{1 + \frac{\epsilon_d}{-\epsilon_m}}\right) \tag{3.12}$$

The field equation inside the indentation will then be given by

$$|\alpha\rangle = C_\alpha cos(q_x x + b\pi/2)\hat{\mathbf{x}} \tag{3.13}$$

where $q_x = \sqrt{k_w^2\epsilon_2 - q_z^2}$. The constant C_α is given by

$$C_{\alpha c} = \sqrt{\frac{2q_x}{aq_x + sin(aq_x/2)cos(\pi b)}} \qquad C_{\alpha s} = \sqrt{\frac{2q_x}{aq_x - sin(aq_x/2)cos(\pi b)}}$$

when b is even or odd, respectively.

For the case of 2-D rectangular modes we can determine the propagation constant of the modes using the effective index method as described by *Gordon et al* Gordon and Brolo (2005) and separating the mode equations of a rectangular waveguide into a combination of the TM and TE modes of parallel plate waveguide in the two different directions, as depicted in Fig 3.12b).

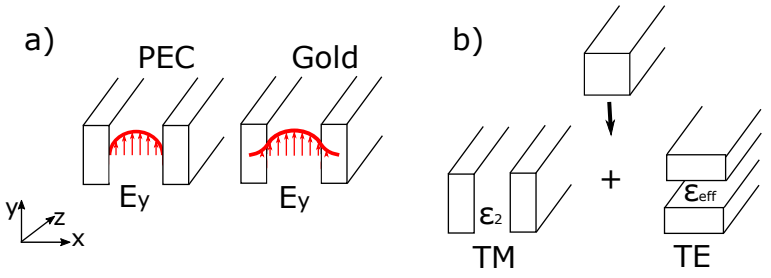


Figure 3.12 a) Electric field inside a PEC and a real metal waveguide b) Principle of the effective index method for rectangular waveguides, which are separated into the modes of 2 parallel plates waveguides. The propagation constant of the TM modes of the 1st waveguide is introduced as an effective dielectric constant $\epsilon_{eff} = \beta_1/k_w$ into the TE modes of the second waveguide.

Solving the first waveguide gives an effective index for the characteristic equation of the other waveguide. For the TE modes this lead to solving Eq 3.11 in order to define a corresponding $\epsilon_{eff} = (q_z/k_w)^2$. We now use this variable in order to solve the characteristic equation of the TE modes of the parallel plate waveguide :

$$coth(\frac{a}{2}\sqrt{q_z^2 - k_w^2\epsilon_{eff}} - b_y i\frac{\pi}{2}) + \frac{\sqrt{q_z^2 - k_w^2\epsilon_m}}{\sqrt{q_z^2 - k_w^2\epsilon_{eff}}} = 0 \tag{3.14}$$

The transverse component of the wavevector will be given by $q_x = \sqrt{k_w^2\epsilon_2 - k_w^2\epsilon_{eff}}$ and $q_y = \sqrt{k_w^2\epsilon_{eff} - q_z^2}$. We can also use a $1st$ order approximation of the $tanh$ function in order to solve this transcendental equation as described by Collin et al. (2007) :

$$q_z = k_w\sqrt{\epsilon_{eff} - \left(\frac{\lambda}{2a'}\right)^2} \tag{3.15}$$

using an effective width $a' = a\left(1 + \frac{2}{k_w a\sqrt{(\epsilon_{eff}-\epsilon_m)+(\lambda/2a)^2}}\right)$. The corresponding field equation will be given by :

$$|\alpha\rangle = \left[C_{qx}C_{\alpha c}\cos(q_x x + b_x\frac{\pi}{2})C_{\alpha s}\sin(q_y y + b_y\frac{\pi}{2})\hat{\mathbf{x}} + C_{qx}C_{\alpha s}\sin(q_x x + b_x\frac{\pi}{2})C_{\alpha c}\cos(q_y y + b_y\frac{\pi}{2})\hat{\mathbf{y}}\right] \tag{3.16}$$

3.5.2 Overlap integrals

The overlap integrals describes how much of the fields couple from the incident waves to the guided modes inside the indentation. The integral is define in the tangential plane and is

define for 1-D slits :

$$\langle k|\alpha\rangle = I_c(b) = C_{\alpha c} C_k \cos(b\pi/2) \left[\frac{2b\sin(ab/2)\cos(ak/2) - 2k\cos(ab/2)\sin(ak/2)}{b^2 - k^2}\right] \quad (3.17)$$

when b is even and

$$\langle k|\alpha\rangle = I_s(b) = C_{\alpha s} C_k \sin(b\pi/2) \left[\frac{2ik\sin(ab/2)\cos(ak/2) - 2b\cos(ab/2)\sin(ak/2)}{b^2 - k^2}\right] \quad (3.18)$$

when it is odd. At normal incidence, only the even overlap integrals are non null. For the single mode approximation this expression reduces to $S_0 = \sqrt{\frac{a}{d}} sinc(ka/2)$.

For the 2-D case, since the field corresponds to similar equations than the slits but defined in two dimensions, we can use a combination of the same expressions :

$$\langle k|\alpha\rangle = [C_{qx} I_c(b_x) I_s(b_y) + C_{qy} I_s(b_x) I_c(b_y)] \quad (3.19)$$

when b_x and b_y are even (note that the constant C_k will have to be changed to its 2-D counter-part C_{kx} and C_{ky}. The I_c or I_s expression must be changed to I_s or I_c when the mode number b_x or b_y become odd. Again at normal incidence only the mode numbers with b_x even and b_y will lead to non-zero integrals. For the single mode approximation for square hole array this expression reduces to $S_0 = \frac{2\sqrt{2}a}{\pi d} sinc(k_x a/2)$.

3.5.3 Scattering coefficients

A field matching procedure is used in order to define the transmission and reflection coefficients at each interface of the structure as if they were semi-infinite medium Martín-Moreno and García-Vidal (2008). Since the fields can be expressed as an infinite number of terms, both summation must be truncated to a sufficient number of terms to reach convergence. For simplicity of the method and consideration of the interesting polarization case, only incident p-polarized wave will be considered, and for the 2-D case, holes of square geometry with similar interspacing in the x and y direction ($d_x = d_y = d$) will be considered. The equations are also derived for the case of an infinite number of holes. For a finite number of holes, Green's dyadic tensor must be used to adequately describe the optical properties of the series of holes Bravo-Abad et al. (2004a).

For the definition of scattering coefficients, the medium are considered to be semi-infinite, and transverse components of the electric fields and magnetic fields are matched at the interface. In order to account for real metals, surface impedance boundary conditions are used, and

thus the electric field matching equation is replaced by de León-Pérez et al. (2008) :

$$\vec{E} = z_s \vec{H} \times \hat{n}_z \tag{3.20}$$

where $z_s = 1\sqrt{\epsilon_m}$. This procedure leads to the definition of transmission and reflection coefficients for each interface given by for interface 1-2 :

$$\left(G_{\alpha\alpha} \frac{f_\alpha^-}{f_k^+} + Y_\alpha \right) \tau_\alpha^{12} + \sum_{\alpha \neq \beta} G_{\alpha\beta} \frac{f_\beta^-}{f_k^+} \tau_\beta^{12} = i \frac{Y_{k0}}{f_{k0}^+} \langle k_0 | \alpha \rangle \tag{3.21}$$

and

$$\rho_k^{12} = -\delta_{k0,\sigma 0} \frac{f_{k0}^-}{f_{k0}^+} + \sum_\alpha \langle k | \alpha \rangle \tau_\alpha^{12} \frac{f_\alpha^-}{f_k^-} \tag{3.22}$$

and for interface 2-3

$$\left(G_{\gamma\gamma} \frac{f_\alpha^-}{f_k^+} + Y_\gamma \right) \rho_{\alpha\gamma}^{23} + \sum_{\beta \neq \gamma} G_{\alpha\beta} \frac{f_\alpha^-}{f_k^+} \rho_{\alpha\beta}^{23} = Y_\gamma \delta_{\gamma\alpha} - G_{\gamma\alpha} \frac{f_\alpha^+}{f_k^+} \tag{3.23}$$

and

$$\tau_{23} = \sum_\alpha \langle k | \alpha \rangle \frac{f_\alpha^+}{f_k^+} + \sum_\beta \langle k | \beta \rangle \frac{f_\alpha^-}{f_k^+} \sum_\alpha \rho_{\alpha\beta}^{23} \tag{3.24}$$

where τ_α^{12} is a transmission coefficient of the 1-2 interface into mode α and τ_α^{23} is the transmission coefficient associated with interface 2-3 of mode α, $\rho_{\alpha\beta}^{23}$ and $\rho_{\alpha\beta}^{21}$ are reflection coefficients of mode α going into mode β for interface 2-3 and 2-1 respectively, Y_k is the plane wave admittance and equals $Y_p = n^2 k_w / k_z$ for p-polarized waves and $Y_s = k_z / k_w$ for s-polarized waves, Y_α is the mode admittance and equals $Y_\alpha = q_{z\alpha} / k_w$ for TE modes. The coupling coefficient

$$G_{\alpha\beta} = \sum_k Y_k \langle k | \alpha \rangle \langle \beta | k \rangle \tag{3.25}$$

quantifies the overlapping of the fields. When considering only the fundamental mode inside each of the array, the coefficients can be greatly simplified to the values Martín-Moreno and García-Vidal (2008) :

$$\tau_0^{12} = \frac{2 \frac{Y_{k0}}{f_{k0}^+} \langle k_0 | 0 \rangle}{G_{00} \frac{f_0^-}{f_k^+} + Y_0} \qquad \rho_k^{12} = -\delta_{k0,\sigma 0} \frac{f_{k0}^-}{f_{k0}^+} + \langle k | 0 \rangle \tau_0^{12} \frac{f_0^-}{f_k^-} \tag{3.26}$$

$$\rho_{00}^{23} = \frac{Y_0 - G_{00} \frac{f_\alpha^+}{f_k^+}}{G_{00} \frac{f_0^-}{f_0^+} + Y_0} \qquad \tau_{23} = \langle k | 0 \rangle \frac{f_\alpha^+}{f_k^+} + \langle k | 0 \rangle \frac{f_0^-}{f_k^+} \rho_{00}^{23} \tag{3.27}$$

3.5.4 Connecting Matrix

Once the coefficients are defined, the total transmission of the array will be given by the sum of all possible paths inside the structure. The waves can bounce back and forth inside the structure an infinite number of times as in a Fabry-Perot cavity, using the different modes of the hole. In order to represent this, we can use a matrix formalism using connecting coefficients, which has been presented in details elsewhere Blanchard-Dionne and Meunier (2016). A loop factor for one cycle inside the hole can be defined by :

$$l(\alpha,\beta) = \rho^{23}_{\beta\alpha} e^{iq_{z\alpha}h} \rho^{21}_{\alpha\beta} e^{iq_{z\beta}h} \tag{3.28}$$

The total transmission will then be given by :

$$t_k = \sum_{\alpha} \tau^{12}_{\alpha} \tau^{23}_{\alpha,k} e^{iq_{z\alpha}h} (1 + M_{\alpha}) \tag{3.29}$$

where M represents the summation of all possible path given by the geometric serie of matrices :

$$M_{\alpha} = \mathbf{V}^{in}_{\alpha} \left[\mathbf{I} - \mathbf{T}_{\alpha}\right]^{-1} \mathbf{V}^{out}_{\alpha} \tag{3.30}$$

where $\mathbf{V_{in}}$ represents a vector with the initial loops of a combination, I is the identity matrix, $\mathbf{T}_{\alpha}$ is a matrix of the subsequent loop factor with a connecting coefficient $a_{\gamma\alpha} l_{\alpha\beta}$, and $\mathbf{V_{out}}$ is a vector of outgoing factor of transmission. These matrices are of the following format :

$$\mathbf{V}^{in}_{\alpha} = \begin{bmatrix} l(\alpha,\alpha) & l(\alpha,\beta) & \dots \end{bmatrix} \quad \mathbf{T}_{\alpha} = \begin{bmatrix} a_{\alpha\alpha-\alpha\alpha} l(\alpha,\alpha) & a_{\alpha\alpha-\alpha\beta} l(\alpha,\beta) & \dots \\ a_{\alpha\beta-\beta\alpha} l(\beta,\alpha) & a_{\alpha\alpha-\beta\beta} l(\beta,\beta) & \dots \\ \vdots & \vdots & \ddots \end{bmatrix} \quad \mathbf{V}^{out}_{\alpha} = \begin{bmatrix} b(\alpha,\alpha) & b(\alpha,\beta) & \dots \end{bmatrix} \tag{3.31}$$

Connecting coefficients $a_{\alpha\beta-\gamma\delta} = \rho^{23}_{\beta,\gamma}/\rho^{23}_{\delta,\gamma}$ adjust the loop factor to take into account the reflections factors of the previous loop (see Blanchard-Dionne and Meunier (2016)). The exit coefficient adjusts the transmission coefficient in order to take into account the exiting mode of the serie $b(\alpha,\beta) = \tau^{23}_{\beta}/\tau^{23}_{\alpha}$. Similarly we can define the reflection coefficients of the array :

$$r_k = \rho^{12}_k + \sum_{\alpha} \sum_{\beta} \tau^{12}_{\alpha} e^{iq_{z\alpha}h} \rho^{23}_{\alpha,\beta} e^{iq_{z\beta}h} \tau^{21}_{\beta,k} (1 + M_{\alpha}) \tag{3.32}$$

The total transmission and reflection will then be given by :

$$T = |t|^2 \qquad R = |r|^2 \tag{3.33}$$

Similarly we can define the amplitude of the guided modes inside the indentation given by A and B :

$$B_\beta = \sum_\alpha \tau_\alpha^{12} e^{iq_{z\alpha}h} \rho_{\alpha,\beta}^{23} e^{iq_{z\beta}h/2}(1 + M_\alpha)$$
$$A_\alpha = \sum_\beta \tau_\alpha^{12} e^{iq_{z\alpha}h/2}(1 + M_\beta); \tag{3.34}$$

In the single mode approximation, these factor can be greatly simplified to the simple Fabry-Perot like equation, for example for the transmission coefficient :

$$t = \frac{\tau^{12}\tau_k^{23} e^{iq_{z\alpha}h}}{1 - \rho_{21}\rho_{23} e^{2iq_{z\alpha}h}} \tag{3.35}$$

3.5.5 Dispersion relation and zero-order approximation

The many reports of sensing with nanohole array usually make a reference to the SPP dispersion relation and wave properties Brolo et al. (2004); de Menezes et al. (2015); Escobedo et al. (2011); Hwang et al. (2008); Im et al. (2009); Ji et al. (2008); Lee et al. (2009, 2012); Lesuffleur et al. (2007); Lindquist et al. (2009); Monteiro et al. (2016); Seiler et al. (2016); Sharpe et al. (2008); Lee and Wei (2010) to describe the electromagnetic properties of the array, given by :

$$k = k_w \sqrt{\frac{\epsilon_m n_d^2}{\epsilon_m + n_d^2}} \tag{3.36}$$

with k_w the wavevector of light in vacuum, ϵ_m the dielectric constant of the metal and n_d the refractive index of the surrounding medium as a theoretical background of the resonance. This portrait of the resonance was inaccurate. As shown by *Pendry et al* Pendry et al. (2004) resonance due to the geometry of the structure can emerge, taking a dispersion relation of the form Pendry et al. (2004) :

$$k_{//}^2 c^2 = \omega^2 + \frac{1}{\omega_{pl}^2 - \omega^2} \frac{64 a^4 w^4}{\pi^4 d^4} \tag{3.37}$$

with ω the angular frequency of light, c the speed of light in vacuum, a and d are the opening of the hole and the period of the array, and $\omega_{pl} = \frac{\pi c}{a\sqrt{\epsilon_h \mu_h}}$ the cut-off frequency of the waveguide mode, which serves as the analogue of the plasma frequency of a metal. The structure thus behaves like a metal with plasma frequency depending of the parameters of the holes. This dispersion relation was obtained using energy conservation principle of light inside and outside the holes Pendry et al. (2004). It can also be retrieved using the formalism

presented above by using the zero-order approximation (ZOA), by considering one guided mode and the zero diffraction order term only. Then, using the condition $r = \pm t$ Shen et al. (2005) for the resonance, we can obtain the following relation :

$$G = \frac{n_2}{icot(q_z h/2)} \tag{3.38}$$

$$G = \frac{n_2}{-itan(q_z h/2)} \tag{3.39}$$

for symmetrical and asymmetrical modes respectively. This relation is a general dispersion relation that is equivalent to Eq 3.37. This approximation requires the wavelength to be long compared to the size of the hole ($\lambda >> a$) Martin-Moreno et al. (2001) for the single mode approximation to be valid, and the hole opening to be small compared to the period so that the higher diffraction order terms in G become negligible De Abajo and Sáenz (2005). The consideration of higher diffraction orders adds a modification to the dispersion relation close to the Brillouin zone, and describes the coupling of incident radiation to the surface modes, who become leaky Pendry et al. (2004); Garcia-Vidal et al. (2010). At small hole separation which we consider in this review, contribution to the surface wave of one hole towards another will depend upon the summation of all diffracted waves Garcia-Vidal et al. (2010). This dispersion relation represents a rough approximation and a full calculation must be taken to obtain the optical properties of the arrays.

3.6 1-D Nanoslit arrays

In this section we consider the sensing properties of nanoslit arrays. These slits are represented by a metallic slab with trenches of size a, spaced of d, and of thickness h, as depicted in Fig 3.13. When we consider a PEC, the transmission properties of the slit array are identical if the ratio of the dimensions of the structure are maintained relatively to the wavelength, since there is no dispersion involved in the optical transmission process. All dimensions could have arbitrary values compared to a single geometric factor. We choose to continue the analysis with realistic values of the period for sensing in order to be coherent with the subsequent sections where the dispersion of the metal is included.

3.6.1 Case of a perfect electrical conductor

In a first instance we treat the metal as a perfect electrical conductor with dielectric constant $\epsilon_m = -\infty$. This leads to the terms $f^{\pm}_{\alpha-k} = 1$ in the scattering coefficient derived in the previous section.

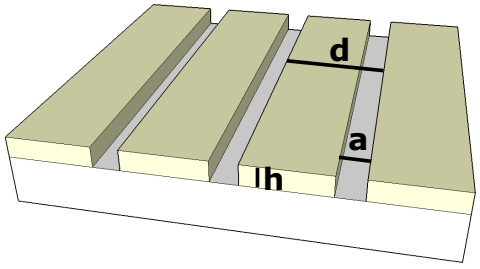


Figure 3.13 Schematic representation of a nanoslit array.

Resonance condition

The transmission of such array is obtained using the CMT by including enough diffraction orders and waveguide modes to obtain convergence. The spectra are presented in Fig 3.14 for the case of a period of $0.55\mu m$ and slit opening $0.1\mu m$ for 3 different thickness. The spectra show perfect agreement with finite element simulation (red dashed lines), and no normalization is used for either of the curves. The resonance features in this graph are defined

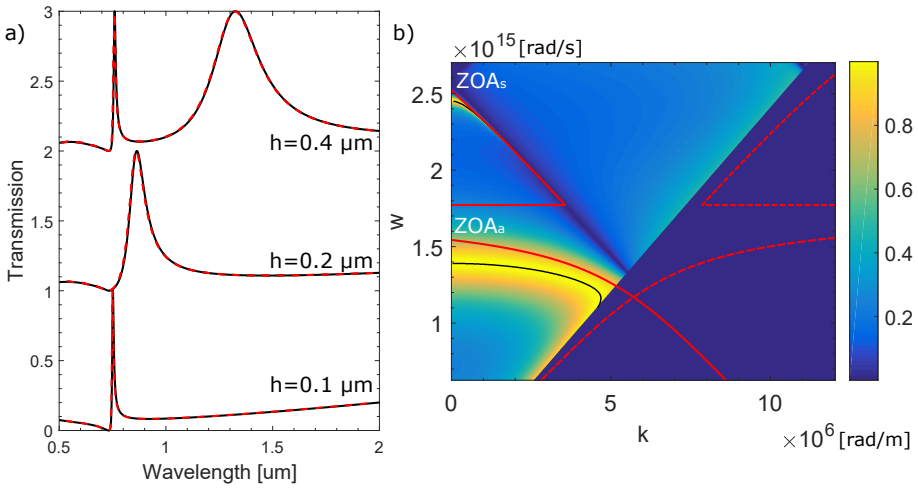


Figure 3.14 a) Transmission spectra of nanoslit arrays obtained using the model based on CMT (black line) and a numerical simulation using FEM (red dotted line) for period of $0.55\mu m$ with slit size $a = 0.1\mu m$ for 3 different thickness b) Dispersion relation of a slit array with parameters $d = 0.55\mu m$, $a = 0.1\mu m$ and $h = 0.4\mu m$. The red lines correspond to the zero-order approximation (ZOA) dispersion relation given by Eq 3.44 for the symmetrical and asymmetrical cases. The black lines are resonance conditions given by Eq 3.42.

by a strict minima, followed by a resonant peak reaching full transmission. The minima

corresponds to the Wood Anomaly condition of the plane wave, given by the relation :

$$k_z = 0 \tag{3.40}$$

This condition occurs when $k_w n = k_w n sin(\theta) + 2\pi/d$, which corresponds to a diffraction order with its orientation parallel to the surface of the metal. The admittance diverges when this condition is met. Since the admittance plays the role of the density of state of the considered diffraction order Bravo-Abad et al. (2004a), all the light will emerge as that diffraction order, which does not couple to fields inside the hole. This condition for the (1,0) diffraction order also marks the *subwavelength* condition for a PEC since it occurs when the period of the array is equal to the wavelength. For wavelength longer than the wavelength of the Wood Anomaly, a resonant peak appears which corresponds to the maxima in transmission. The origin of this resonance can be understood by looking at its dependence upon its incident wavevector, as presented in the dispersion relation of Fig 3.14. For slit arrays, the condition of resonance can be viewed as the condition of constructive interference of a Fabry-Perot interferometer. The main difference with the resonant modes of a conventional transparent slab is that the reflection coefficients at each interfaces have an imaginary part which will contribute to the phase shift of the propagating wave. If we consider only the fundamental modes propagating inside the holes, and we write the reflection and transmission coefficients as a complex number $\rho = |\rho|e^{i\theta}$ and $\tau = |\tau|e^{i\theta_\tau}$ and use the relation $|\tau_{12}||\tau_{23}| = 1 - |\rho_{21}||\rho_{23}|$, we can write the total transmittance as

$$T = |t| = \frac{1}{1 + \frac{4R}{(1-R)^2} e^{i(\theta + 2q_z h)}} \tag{3.41}$$

where $R = |\rho_{12}||\rho_{23}|$ and $\theta = \theta_{21} + \theta_{23} = arg(\rho_{21}) + arg(\rho_{23})$. This equation emphasizes the condition of full transmission whenever :

$$\theta + 2q_z h = 2\pi \tag{3.42}$$

This is the condition presented by *Marquier et al* Marquier et al. (2005) and plotted as the black line in Fig 3.14. Depending on which factor of Eq 3.42 $q_z h$ or θ contributes the most to the phase shift, the resonance is said to have a "cavity" type or a "surface mode" type Marquier et al. (2005).

In this figure the dispersion relation obtained using the zero-order approximation is plotted with the red line. This relation for the case of nanoslit arrays can be retrieved considering

that $S_0 = \sqrt{a/d}$ and $q_{z0} = k_w n_2$, which leads to :

$$\beta_s = k_w n_s \sqrt{1 + \frac{S_0^4 cot^2(q_z h/2) n_s^2}{n_h^2}} \tag{3.43}$$

$$\beta_a = k_w n_s \sqrt{1 + \frac{S_0^4 tan^2(q_z h/2) n_s^2}{n_h^2}} \tag{3.44}$$

for symmetrical and antisymmetrical resonances respectively, where n_s is the refractive index at the surfaces when they are equal, that is $n_1 = n_3 = n_s$, and n_h is the refractive index inside the hole. The propagation constant for this resonant condition is greater than the light line as is plotted in the dashed red line in Fig 3.14b) ; the coupling of this resonant state must thus be achieved through an evanescent wave. In this subwavelength regime, a diffraction order other than zero will have a tangential wavevector greater than k_w meaning they can couple to this resonant state. The red line represents the condition $k = k_r - \beta$, where k_r corresponds to the reciprocal wavevector $k_r = 2\pi/d$ of the periodic medium. In the dispersion relation graph, this is equivalent to a symmetry operation on the half Brillouin axe ($k = \pi/d$). This means that the structure possesses dispersive resonant states with wavevector higher than the wavector of light in the medium, which can only be excited via the higher diffraction orders. This condition represents a reasonable approximation for the position of the maxima of resonance for the dimension considered since the zero order is the most contributing factor in the coupling coefficient G which marks the dependency of the resonance (see Eq 3.39).

Sensitivity and resolution

Sensitivity of the nanoslit array implies a modification of the resonance condition of the array as a function of a change in refractive index and so a shift in the wavelength of resonance. As a first approximation we can turn to the zero-order approximation to determine a sensitivity relation by taking advantage of its simple analytical equation. If we look at Eq 3.44 we consider impinging light to be at normal incidence (the case of interest for sensing with nanohole arrays) and consider the case of similar refractive index n for all medium, we can obtain the following resonant condition using $\beta_a = k_x = 2\pi/d$:

$$\lambda_r = nd\sqrt{1 + S_0^4 tan^2(q_z h/2)} \tag{3.45}$$

Sensitivity will then be define as the derivative of this relation in regard to the refractive index, which leads to :

$$S = \frac{d\lambda}{dn} = \frac{\lambda_r}{n} \tag{3.46}$$

The sensitivity for a PEC slit array is simply proportional to the resonant wavelength of the array just like in a simple slab resonator. Using CMT we can determine the sensitivity with the consideration of all diffraction order and guided modes using the full calculation for two different refractive index and use $S = \frac{\Delta\lambda_r}{\Delta n}$. In Fig 3.15a) the sensitivity of the nanoslit array

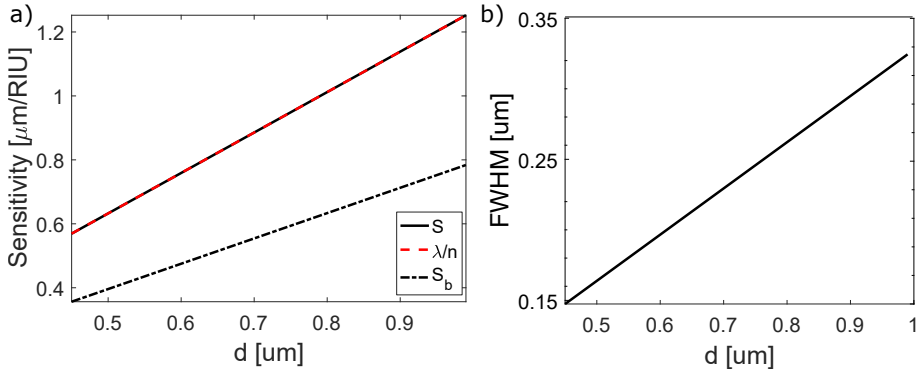


Figure 3.15 a) Sensitivity and b) FWHM of the slit array obtained using CMT as a function of period with slit width $a = 0.2d$ and thickness $h = 0.2d$. The sensitivity equation given by the zero-order approximation of Eq 3.46 is given by the dashed black lines.

is plotted and superposed with the value λ_r/n obtained from Eq 3.46. The curve shows a perfect match, even if this last equation was derived under the zero-order approximation. In fact, if we consider the full calculation of the factor G, we need to consider higher diffraction orders. While this action might change the value of the square root on the right side of the Eq 3.25 and change the wavelength of resonance, the derivative will still be equal to λ/n since the other diffraction orders have similar dependency upon refractive index change. Mathematically, this arises from the dependency of the transcendental equation upon the incident wavevector. Bulk sensitivity is defined whenever we consider region 3 as a substrate for which the refractive index does not vary, so the refractive index change is occurring in region 1 and 2. For the case considered in Fig 3.15 this leads to a bulk sensitivity which scales as a fraction of the total sensitivity. This proportion is a consequence of the field distribution around the structure at the wavelength of resonance and thus scales as the proportion of the fields which is contained in Region 3, in we rely on the waveguide perturbation theory presented in Eq 3.3. This will be described in greater details in the next section.

Discussion of the sensitivity of the array in the case of a PEC is equivalent to considering its resonant wavelength since the two are directly proportional. For small thicknesses of the metal film compared to the period, the resonance is very close to the Wood Anomaly condition. As we can see from Eq 3.45 the factor $tan(q_z h/2) \approx 0$, and in that case and the wavelength of resonance will approach $\lambda_r \approx nd$ and $S \approx d$. For larger thicknesses, the increased phase factor

of the propagation inside the hole will lead to resonances at higher wavelengths, and so the sensitivity will be greater. An important point to consider is that higher sensitivity doesn't necessarily lead to improve sensing performances. The FWHM, presented in Fig 3.15b), increases at the same rate as the sensitivity. So the improved sensitivity is counterbalanced by lower peak definition. The resolution, according to eq 3.2, will thus depend upon the depth of the peak. The effect of the slit width upon the properties of the array is presented in Fig 3.16. When the slit width is small an improve quality factor is observe which is due

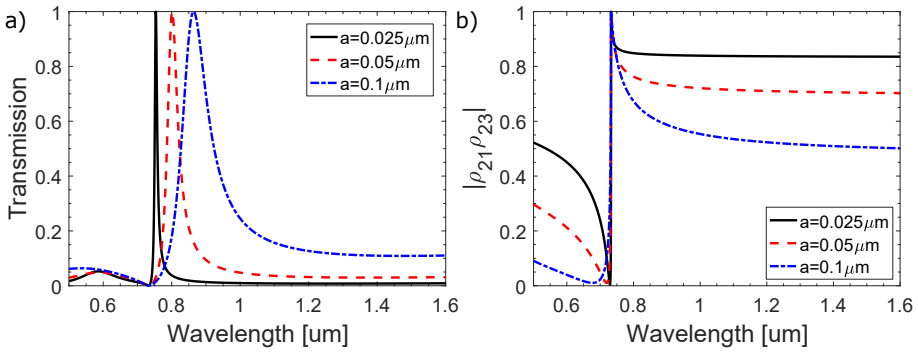


Figure 3.16 a) Transmission spectra and b) Reflection coefficient for a nanoslit array of period $d = 0.45\mu m$ and thickness $0.2\mu m$ for 3 different slit widths.

to better FWHM and depth of the peak, as can be observed in Fig 3.16 a). In fact, reducing the width increases the reflectivity of the interface. If we look at Eq 3.41 we can retrieve the equivalent notion of the Finesse of the peak as for a Fabry-Perot resonant, which is equal to $F = 4R/(1-R)^2$. In this zero-order approximation, we can write the reflection coefficient :

$$R = |\rho|^2 = \frac{|Y_\alpha - G|^2}{|Y_\alpha + G|^2} \tag{3.47}$$

where $G = na/d$ and $Y_\alpha = n$ for the case of a PEC. Reducing the slit width increases the reflectivity of the array, which is equivalent to improving its Finesse. This in turn improves the precision at which we can determine the position of the maxima, and by consequence the resolution. We can also observe a slight blue shift of the position of the peak since the phase factor relative to the reflection is reduced for narrower slit.

The resolution of the array is plotted in Fig 3.17 as a function of the period of the array. Since we deal with 3 factors a, d and h, we consider 3 cases of interest : 1- The ratio of the slit width and the thickness is maintained compared to the period of the array for all values ($a = 0.4h = 0.2d$). In this case the resolution is constant and *independent* of the period, which is consistent with the intuitive idea that a structure with no dispersion must show similar optical properties if all ratios are constant compared to the wavelength. 2- The slit

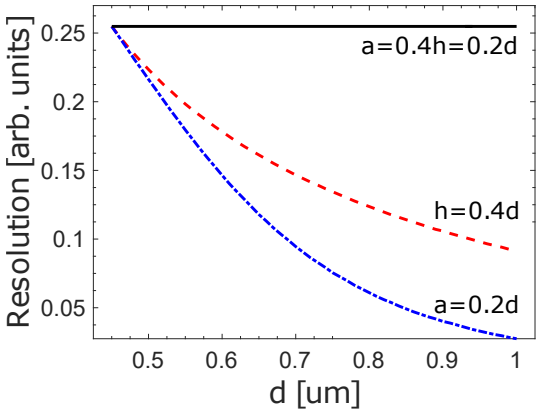


Figure 3.17 Resolution of the array (Eq 3.2) for 3 different cases. 1- The slit width and thickness $a = 0.4h = 0.2d$ are kept proportional to the period. 2- Thickness is kept proportional $h = 0.4d$ while slit width is constant $a = 0.1\mu m$. 3- Slit width is kept proportional to the period $a = 0.2d$ while the thickness is kept constant $h = 0.2\mu m$

width ratio to the period is maintained for all values and the thickness is maintained at $0.2\mu m$ (h=0.4d). This is the same as reducing the thickness of the metal compared to the other parameters and thus moves the resonance closer to the Wood Anomaly. Since the Wood Anomaly leads to a minima in resonance, the peak is in a certain way "cut" and narrower, leading to better resolution. 3- The thickness ratio to the period is maintained for all values and the slit width is maintained at $0.1\mu m$ (a=0.2d). Reducing the width of the array with the other parameters constant (red dashed line) significantly improves the quality factor of the peak and so its resolution, as was pointed out in the discussion of the slit width. For a PEC the guidelines for sensing would be to use a slit as small as possible with a metal thickness as small as possible too.

Fields distribution and surface sensitivity

The total normalized bounded fields calculated with CMT is given in Fig 3.18a), and the decomposition of the different diffraction order and guided mode inside the slits in b). The total field norm is the sum of all diffraction orders, weighted by their respective reflection or transmission coefficient. Strong localization is found at the apex of the slit which is a region of strong overlapping between the electromagnetic waves inside and outside the holes.

In Fig 3.19a), the shift in wavelength associated with changes in refractive index of certain region only (1-3 or 2) is plotted. In Fig 3.19b) the surface sensitivity coincides with the proportion of $|E|^2$ which is contained at the surface. This is consistent with the "type" of resonance, which shows a stronger surface character for small thicknesses of the metal layer.

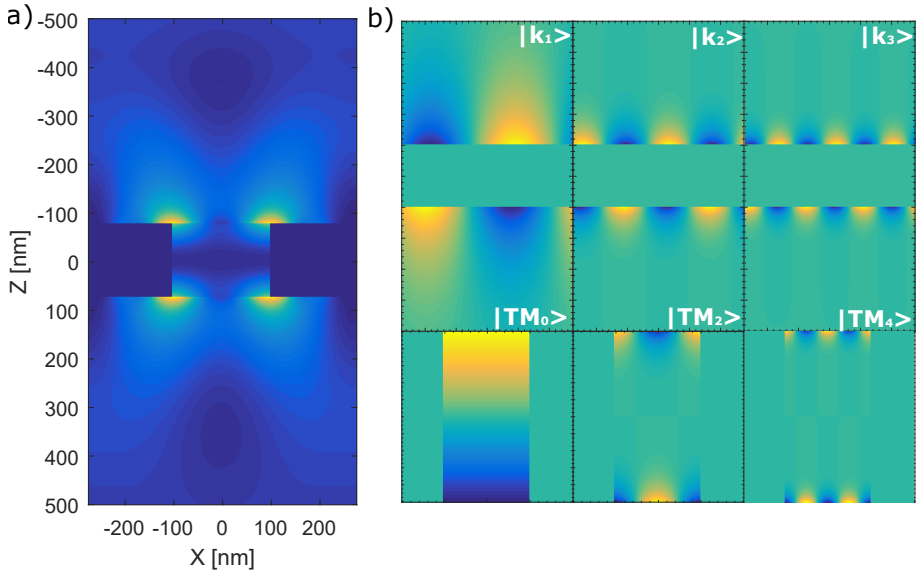


Figure 3.18 a) Electric fields norm $|E|$ obtained using CMT for a nanoslit of period $d = 0.55\mu m$, slit width $a = 0.1\mu m$ and thickness $h = 0.2\mu m$. b) Fields in region 1-3 given by the diffraction orders (+1), (+2) and (+3) and fields inside the slit for TM modes 0,2 and 4. These last 3 graphs have been cropped for improved visualization.

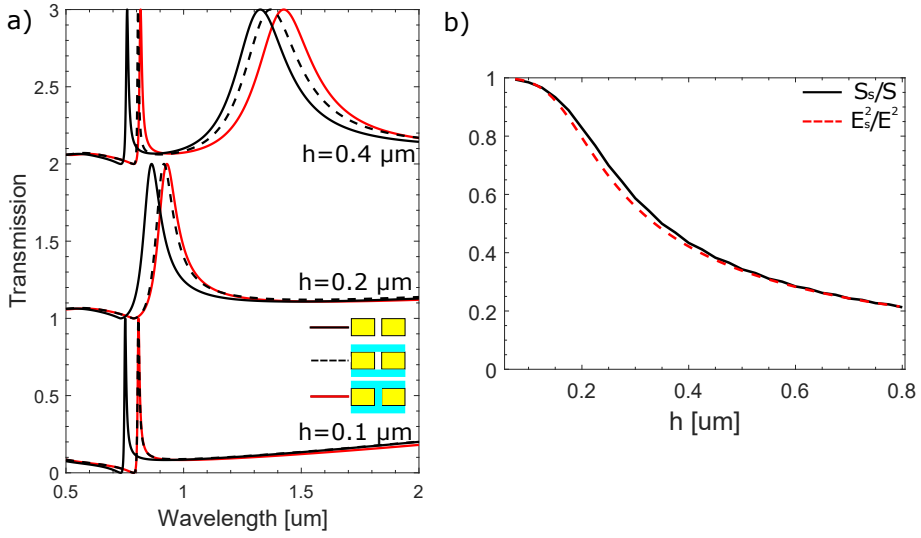


Figure 3.19 a) Transmission spectra for slit period $0.55\mu m$ and slit opening $a = 0.1\mu m$ the 3 different thickness and different refractive index for the different regions. The red line corresponds to a refractive index of 1.33 for all region. The black dashed line are the transmission with a change of refractive index to 1.43 for the surfaces of the slit only. The black line represents the shift for a change of refractive index in all region. b) Black line - Percentage of the shift in resonance peak position due to the change of refractive index at the surface as a function of thickness. Red dashed line - Field integral percentage of the field contained on the surfaces of the array.

3.6.2 Case of real metal

Considering the dispersion of a metal changes the resonance properties of the array. The propagation of light at the surface will contain losses since an imaginary part is now included in the scattering coefficients via the impedance factor of the metal z_s. Furthermore, the propagation inside the slit will penetrate the side walls, leading to a modification of the value of the propagation constant, as described by Eq. 3.11. In this review we focus on gold as the material of the nanostructures since it is the metal that is the most reported in experimental applications of nanohole array sensing and has the advantageous properties of being non-reactive and being an excellent conductor. The data of gold from *Johnson and Christy* Johnson and Christy (1972) is used.

Resonance Condition

In Fig 3.20 the transmission spectra of gold nanoslit using CMT is plotted and superposed with the results of finite element simulation for a structure of period $d = 0.55\mu m$ and slit width $a = 0.1\mu m$ for 3 different thicknesses. The minima associated with Wood Anomaly is

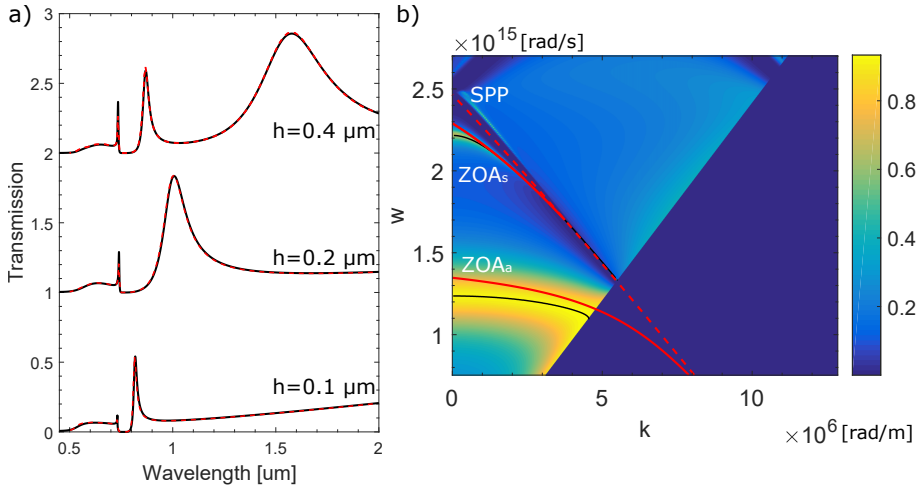


Figure 3.20 a) Transmission spectra of nanoslit arrays obtained using CMT for period of $0.55\mu m$ with slit size $a = 0.1\mu m$ with gold as the metallic layer (black lines) for 3 different thickness. The red dashed line corresponds to numerical simulations using FEM. b)Dispersion relation of nanoslit array of dimensions $d = 0.55\mu m$, $h = 0.4\mu m$ and $a = 0.1\mu m$. The red lines are the dispersion relation obtain under the ZOA (Eq 3.50). The black lines are resonance conditions given by Eq 3.42. The red dashed line corresponds to the dispersion of an SPP on a flat surface, and coincides with the Wood anomaly following Eq 3.48. .

broadened when losses of the metal are included. A slight red shift is also present which can be taken into account mathematically by considering that the minima condition is now given

by :

$$k_z + z_s k_w n_s^2 = 0 \tag{3.48}$$

This relation is actually equivalent to the SPP dispersion relation in Eq 3.36 when considering SIBC Garcia-Vidal et al. (2010). If we take into account the factors $f_k^{\pm}$ and $f_\alpha^{\pm}$ in the dispersion relation obtained within the zero-order approximation we arrive to the following dispersion relations :

$$\beta_a = n_s k_w \sqrt{1 - n_s^2 \left(i \tan\left(q_z h/2\right) S_0^2 / Y_\alpha + z_s (S_0^2 - 1)\right)^2} \tag{3.49}$$

$$\beta_s = n_s k_w \sqrt{1 - n_s^2 \left(i \cot\left(q_z h/2\right) S_0^2 / Y_\alpha - z_s (S_0^2 - 1)\right)^2} \tag{3.50}$$

The dispersion relation after the symmetry operation around the Brillouin axe is plotted in Fig 3.20b) (red line). We can observe a strong redshift of the condition of resonance, which is due to a smaller propagation inside the hole constant for the case of the real metal (factor q_z) and a change in surface propagation (factor $z_s(S_0^2 - 1)$). An interesting feature of the resonance for the case of thin metallic layer is that a broadening of its peak leads to a small maxima on both side of the Wood minima, as can be observed on Fig 3.20a), and was also experimentally observed by *Lee et al* Lee et al. (2012).

Sensitivity and Resolution

Sensitivity of the array is plotted in Fig 3.21a) (red dashed-dotted line), and compared to Eq 3.46, which is the result for a PEC. The sensitivity for this case highlights the effect of the metal dielectric constant. The modification in the resonant properties can be describe with the term $zs(S_0^2 - 1)$ in Eq 3.50 which is related to the surface mode and the term q_z which accounts for the change in resonance due to the propagation in a lossy parallel plate waveguide. Both contribution modifies the position of the resonance but have small dispersive behavior and so will only slightly change the sensitivity of the array.

In Fig 3.22a) the transmission spectra of a slit array for 3 different slit width is presented to highlight the effect of this parameter. The situation is quite different than for the case of a PEC. First, SIBC implies losses for the coupling factor G which reduces the absolute value of the reflection parameters (Fig 3.22b)) compared to the PEC case. Also, reducing the slit width redshifts the position of the resonance. Indeed, for the TM modes of slab waveguides with metal interfaces, the surface plasmon on each interfaces interact with each other Gordon and Brolo (2005); Collin et al. (2007), which reduces the transverse wavevector component and thus increase the value of the wavevector in the propagation direction. This also leads to a greater imaginary component of this propagation constant, which is relative to propagation

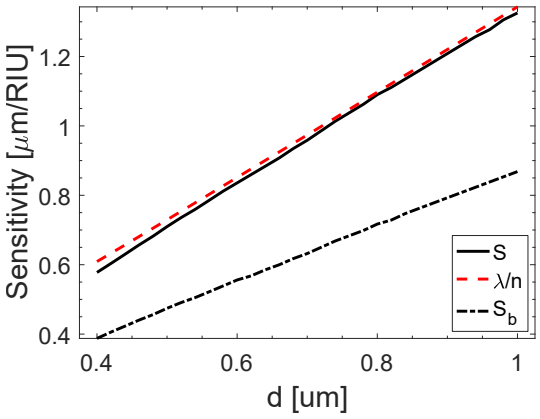


Figure 3.21 a) Sensitivity of the nanoslit array as a function of period for a slit width of $0.2d$ and thickness of $0.2d$. The Red lines accounts for the total sensitivity (change of refractive index in all regions) and the red dashed-dotted line for bulk sensitivity only (change of refractive index in region 1-2). The black dashed curve represents the perfect conductor sensitivity case of λ/n.

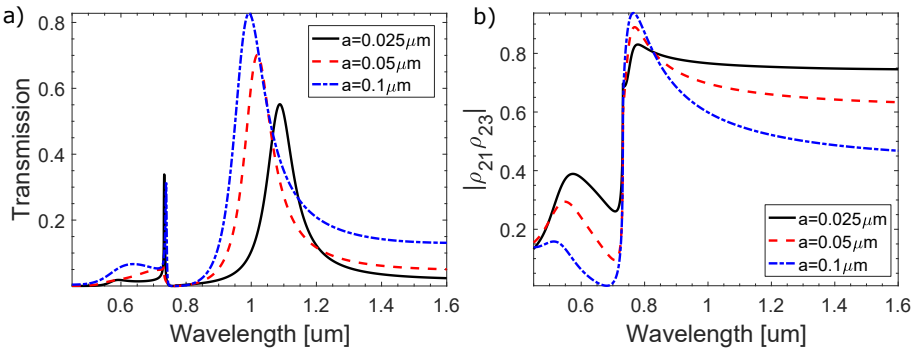


Figure 3.22 Transmission spectrum and b) Reflection coefficients as a function of wavelength for nanoslit array of period $0.45\mu m$ and thickness $0.2\mu m$ for 3 different slit width.

losses. Ensuing is a redshifted peak with lower depth. The values of the propagation constant for 3 different thickness of a slit array can be seen in Fig 3.23, along the one for a PEC.

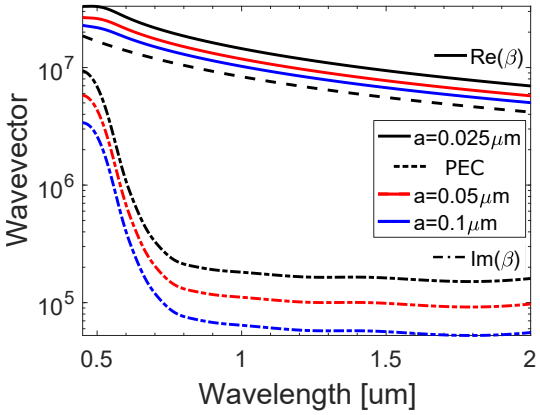


Figure 3.23 Real and Imaginary values of the propagation constant as a function of wavelength for nanoslit array of period $0.45\mu m$ and thickness $0.2\mu m$ for 3 different slit width. The dashed line corresponds to the value for a PEC of width $a = 0.025\mu m$.

The FWHM and depth are not monotone functions of the period for real metals since the Wood Anomaly and metal losses greatly influences the shape of the resonant peak. Reducing the thickness of the metal array leads to a conflict with the broadened Wood Anomaly which "hides" the resonance feature, while increasing the thickness leads to a broadened peak. A small slit width increases losses in the propagation inside the hole, while a large one leads to poorer resonant quality factor. A compromise needs to be made and optimal values of the parameters can be found for each period of the array, and are represented in Fig 3.24b). The resolution for the period of $0.55\mu m$ (see Eq 3.2) is plotted in a 2-D graph in the inset of Fig 3.24a) as a function of period and thickness. Optimal values of the slit width ranges in between $0.3 - 0.4d$ times the value of the period, while for thickness it ranges in between $0.1 - 0.2d$. Resolution is improved as we move to longer wavelengths where the losses due to the metal have generally lesser effects on the resonance.

Field distribution and surface sensitivity

CMT is used to calculate the field distribution and is plotted in Fig 3.25a) the field for the case of a $0.55\mu m$ array with $0.1\mu m$ opening at different thickness. Also presented is a plot of the percentage of the field contained inside a layer of thickness L on the surface. For a thickness of $0.1\mu m$ most of the field are concentrated on the surface and extend further away from the interface. This is what could be expected from a surface type resonance. For a thicker film of $0.4\mu m$ the modes inside the slit include a strong proportion of the total

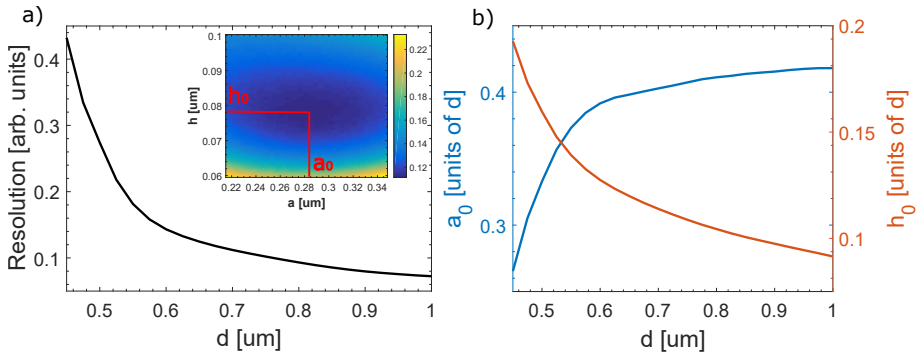


Figure 3.24 a) Resolution of the array at the optimal thickness and slit width. *Inset* Resolution as a function of slit width and array thickness for a period of $0.7\mu m$ b) Optimal thickness and slit width as a function of the period.

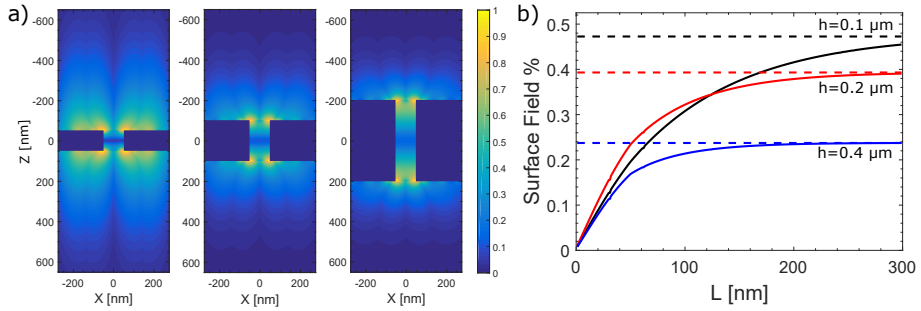


Figure 3.25 a) Electric field norm $|E|$ for a nanoslit array of period $0.55\mu m$ and slit opening $0.1\mu m$ for 3 different thickness $h = 0.1\mu m$, $0.2\mu m$ and $0.4\mu m$. b)Field percentage contained within a layer of thickness L on the top surface of the array for 3 different thickness of the metal film considered. The dashed line corresponds to the field percentage for the whole surface.

fields. The plot of Fig 3.25 features the percentage of the field that is located inside a layer of thickness L on the top surface of the structure (Region 1). For the thinner metal layers this proportion can reach up to 0.45. Since we are dealing with symmetrical scenarios another 0.45 is located in the substrate in region 3 and the rest inside the indentation. For thicker metal layers this proportion of surface field is greatly reduced which limits the sensing capacities of such dimensions for the case of thin layer sensing. We can also observe that the resonance for thinner metal extend more inside the sensing medium and reach their maximal value of the field integral for thicker sensing layers.

3.6.3 Case $n_1 \neq n_3$

Resonance condition

We now consider a higher refractive index substrate of $n = 1.51$ (glass). The transmission spectrum for a period of $0.55\mu m$ and slit width $0.1\mu m$ for different thicknesses is provided in Fig 3.26a) for gold using CMT (black full line) and finite element simulation (red dashed line). The presence of a higher refractive index on one end of the array will lead to a slight redshift

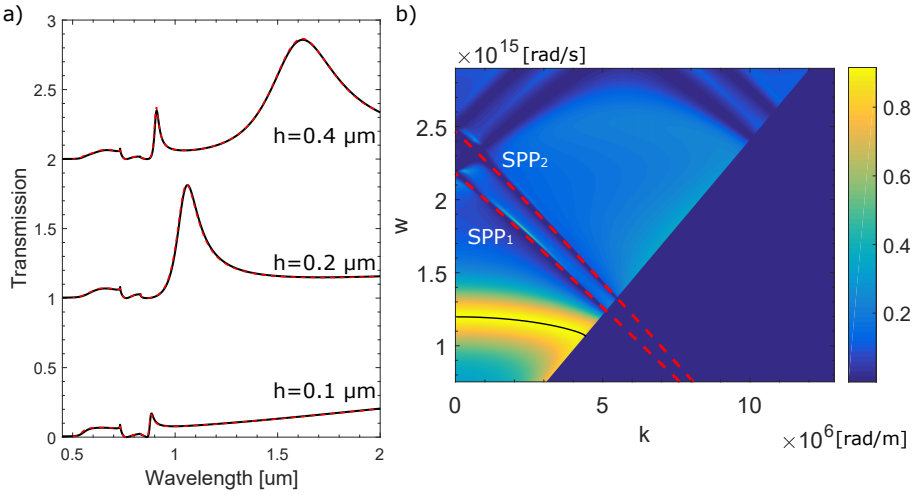


Figure 3.26 a) Transmission spectra obtained with CMT for a nanoslit array of period $0.55\mu m$ and slit width $0.1\mu m$ for 3 different thickness with the refractive index of glass ($n_3 = 1.51$) for region 3. The dotted red line is the result obtained with numerical simulation based on FEM. b) Dispersion relation for a nanoslit array of dimensions $d = 0.55\mu m$, $a = 0.1\mu m$ and $h = 0.4\mu m$ with gold as the metal and glass as the substrate. The black line corresponds to the resonance condition given by Eq 3.42. The red dashed lines corresponds to the dispersion of an SPP on a flat surface with the index of region 1 and 3, and coincides with the Wood anomaly following Eq 3.48.

of the position of the resonance since the reflection coefficient ρ_{23} changes dependence. The

most important addition in the transmission spectrum is the presence of a second Wood Anomaly for the glass interface which forces a minima at longer wavelength (see Eq 3.40). This can interfere with the resonance maxima. The effect of this second Wood Anomaly is also represented in the dispersion relation of Fig 3.20b) where a minima "cuts" into the symmetrical mode line at higher frequency. One way to avoid the detrimental effect of this second Wood Anomaly is to have the metal film thick enough for the peak to move away from it.

Sensitivity and Resolution

Only the bulk sensitivity is relevant for the case of higher index substrate, and its value is plotted in Fig 3.27a) as a function of the period for a thickness of $0.4d$ and slit opening of $0.2d$. This sensitivity is compared to the results obtained for a matching index substrate. The bulk sensitivity is reduced, even though the resonance is shifted towards higher wavelengths. This is due to a higher concentration of the fields located inside the region of the substrate. Fig 3.27b) plots the reflection coefficient as a function of the wavelength which shows a shift of the maxima towards higher wavelength. In Fig 3.28b) we find that the optimal values of the

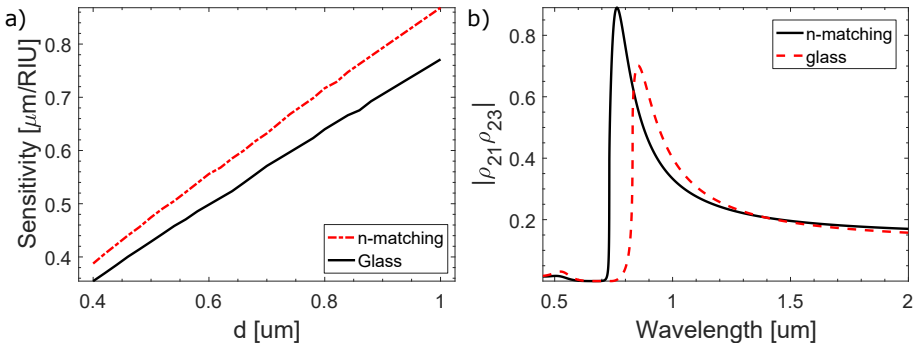


Figure 3.27 a) Bulk sensitivity as a function of period of a nanoslit array with gold as the metal for the case of matching refractive index (red line) and glass as the substrate (black line) for a slit array of thickness $0.4d$ and slit width$0.2d$. b) Reflection coefficient product ρ_{21} and ρ_{23} as a function of wavelength for a slit array of period $d = 0.55\mu m$, slit width $a = 0.2d$ and thickness $h = 0.4d$

thickness reaches higher values of $0.28 - 0.32d$ to distance the peak from the Wood Anomaly and retrieve optimal peak condition. Broadening of the peak due to the effect of the slit width is less critical in that case and the optimal width is found to range around $0.03 - 0.09d$. We find the resolution of the array to be constant as a function of the periodicity. The overall performances are highly reduced and we can conclude that a matching index substrate would improve the sensing performances of slit arrays.

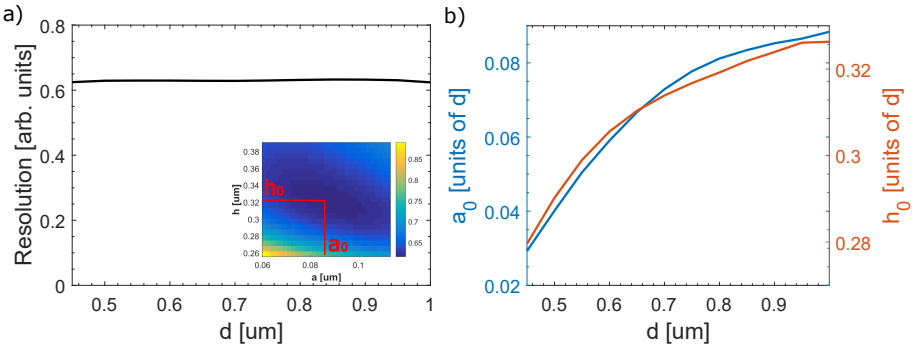


Figure 3.28 a) Resolution of the array at the optimal thickness and slit width *Inset* Resolution as a function of slit width and array thickness for a period of $0.7\mu m$ b) Thickness and slit width that gave the optimal resolution.

Fields distribution and surface sensitivity

Fields distribution for this case of nanoslit array is plotted in Fig 3.29. Again as the metal film thickness is increased most of the field will be located inside the slit. For small thickness for which the resonance is close to the Wood Anomaly on the glass substrate, strong divergence of the fields inside the substrate are observed which is detrimental to the sensing performances. The fields on the top surfaces only reach 30%.

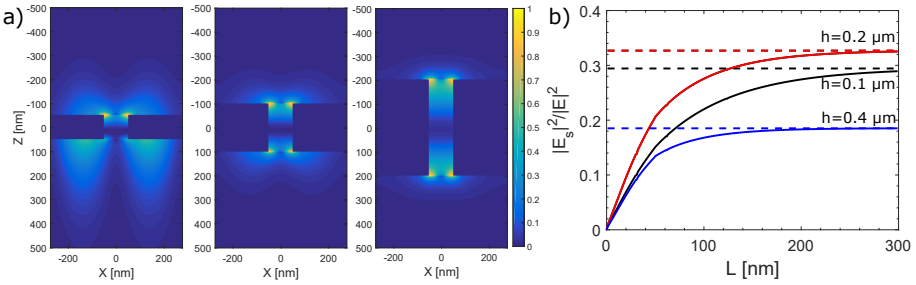


Figure 3.29 a) Electric field norm $|E|$ for a nanoslit array of period $0.45\mu m$ and slit opening $0.1\mu m$ for 3 different thickness $h = 0.1\mu m$, $0.2\mu m$ and $0.4\mu m$ with glass as a substrate.
b)Field percentage contained within a layer of thickness L on the top surface of the array for 3 different thickness of the metal film considered.

3.6.4 Nanoslit arrays - Conclusions

— Sensitivity for the nanoslit array is given by λ/n which is an exact solution for the case of a PEC and an excellent approximation whenever a finite dielectric constant is considered for the metal film.

— The FWHM increases in the same manner than the sensitivity for a PEC so the

performances of the array will depend only on the quality factor or shape of the sensing peak.

— For a PEC with similar refractive index in region 1 and 3 the FWHM and depth of the peak improves for a smaller slit width since it improves the reflectivity at both interfaces, leading to sharper resonant peak. A smaller thickness is also preferable since it moves the peak closer to the minima induced by the Wood Anomaly, which again reduces the FWHM.

— Whenever we deal with a real metal, the thickness of the array should be large enough for the resonance to move away from the broader Wood Anomaly minima, which is detrimental to the sensing performances of the array. For higher refractive index of the substrate the metal layer will need to be thicker to achieve improved sensing performances.

— For sensing a compromise must be made for both parameters a, h. While a smaller slit width leads to improve quality factor of the peak, it can also lead to losses in the propagation of the waves inside the indentation. A small thickness leads to improved FWHM, but also leads to obstruction of the peak with the Wood Anomaly. Optimal values can thus be found. This value ranges around $a = 0.3 - 0.4d$ and $h = 0.1 - 0.2d$ for a matching index substrate and $a = 0.05 - 0.1d$ and $h = 0.28 - 0.32d$ for the case of glass as the substrate.

— A matching index substrate improves the quality of the sensor by allowing a thinner metal layer to be used without getting affected by the Wood anomaly of the glass interface.

— No matter what the substrate is, at least $\approx 50\%$ of the surface field will be located inside of it which means that the bulk sensitivity can only reach about half its ideal value of λ/n. For thin film sensing an even bigger proportion of the sensitivity will be loss since a portion of the fields is located inside the hole. This proportion increases as the thickness increases.

3.7 2-D Square Nanohole array

In this section we analyse the sensing properties of square hole array which is illustrated in Fig 3.30. This structure is represented by periodic hole of dimension a, spaced apart of d in a metal film of thickness h. The properties of square hole arrays differ significantly from the ones of nanoslit array presented in the previous section. This is mainly due to the different nature of the propagation of light inside the hole, which is now characterized by a cutoff frequency.

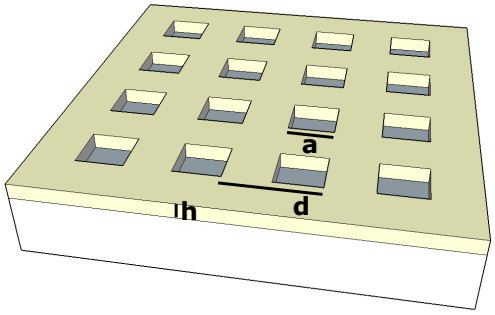


Figure 3.30 Schematic representation of a square nanohole array

3.7.1 Case of perfect electrical conductor

Resonance Condition

The transmission spectra obtained with CMT for square nanohole array of period $0.55\mu m$ and hole size $0.2\mu m$ with a PEC is presented in Fig 3.31a) for several thickness. The transmission

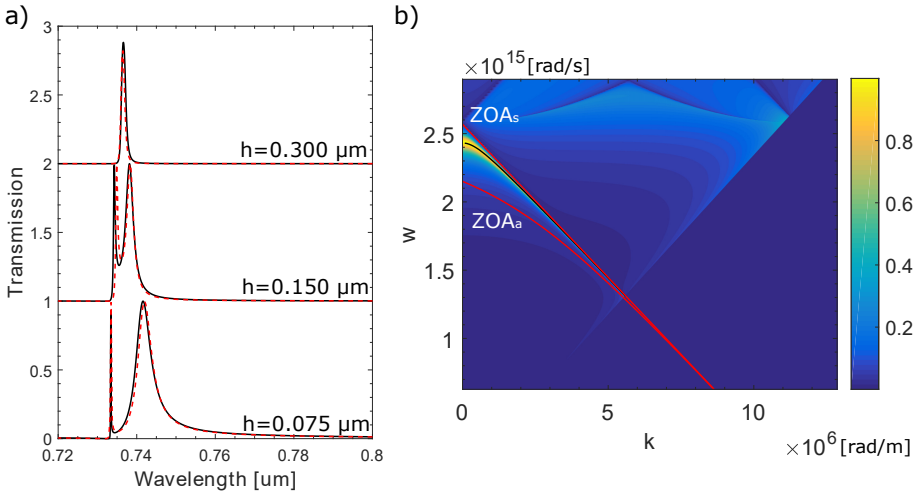


Figure 3.31 a) Transmission spectra of square nanohole arrays obtained using CMT (black lines) for period of $0.55\mu m$ with hole size $a = 0.20\mu m$ for 3 different thickness. The red dotted lines correspond to numerical results obtained using FEM. b) Dispersion relation of a square hole array with parameters $d = 0.55\mu m$, $a = 0.25\mu m$ and $h = 0.075\mu m$. The red lines corresponds to the ZOA dispersion relation given by Eq 3.54. The black lines are resonance conditions given by Eq 3.51

is characterized by a strict minima due to the Wood Anomaly, for which the condition can be expressed by Eq 3.40. For small thicknesses of the metallic layer, two transmission maximas occurs for wavelengths very close to the Wood Anomaly, which corresponds to asymmetrical and symmetrical resonant modes of the structure. For small hole size the resonance occurs for

frequencies below its cutoff frequency, so the propagation of light is evanescent and does not contribute to the phase shift. This is indicative of the different nature of the resonance for this type of cavity which resembles more a truly bound surface mode of the interface Garcia-Vidal et al. (2010). Full transmission can still occur even for evanescent propagation. This is due to the reflection coefficients reaching values greater than 1 ; the restriction of current conservation $|\rho| \leq 1$ only applies to propagating waves, a point highlighted by *Martin et al* Martin-Moreno et al. (2001). Evanescent waves only require $Im(\rho) \leq 1$. Resonance for this structure occurs when the reflection amplitude compensates the loss in amplitude of the evanescent propagation, which can be described by :

$$|\rho_{12}||\rho_{23}| = 1/e^{-2|q_x|h} \tag{3.51}$$

Thus, the resonance of square hole array can be viewed as the contribution of two "atomic modes" of both interfaces coupled to each other through the evanescent waves inside the hole to form a "molecular" mode Garcia-Vidal et al. (2010). The way the two resonances influence each other will vary upon the dimensions of the array. For thick enough layers, the exponential decay will be too high compared to the magnitude of the reflection and the transmission won't reach 1, but will still exhibit a maxima in transmission Martin-Moreno et al. (2001). The resonance of the array is illustrated with the dispersion relation in Fig 3.31b). In the zero-order approximation the overlap integral is reduced to :

$$S_0 = \frac{2\sqrt{2}a}{\pi d} \tag{3.52}$$

The propagation constant of the first mode (TE_{10}) is given by :

$$q_z = \sqrt{(k_w n_2)^2 - (\pi/a)^2} \tag{3.53}$$

Using these variables into Eq 3.39, we can determine an analytical dispersion relation for the resonance :

$$\begin{aligned} \beta_s &= k_w n \sqrt{1 + \frac{S_0^4 tan^2(\phi) k_w^2 n^2}{(k_w n)^2 - (\pi/a)^2}} \\ \beta_a &= k_w n \sqrt{1 + \frac{S_0^4 cot^2(\phi) k_w^2 n^2}{(k_w n)^2 - (\pi/a)^2}} \end{aligned} \tag{3.54}$$

These relations are plotted on the dispersion relation calculated using CMT. Contribution of higher diffraction orders is more important in this type of resonance which leads to a stronger

bend of the dispersion relation near the Brillouin zone and to a poorer approximation of the resonance condition with the zero order approximation. The resonance condition given by Eq 3.51 is plotted in the black curves in Fig 3.31b) and gives exact position of the resonance *as long as* $\lambda < 2a$. Otherwise, the mode inside the hole is propagative and the condition will be given by the same condition as the one for the nanoslit array given in Eq 3.42.

Sensitivity and Resolution

Using the zero order approximation we can define a resonant wavelength for the case of the square hole array using Eq 3.54 for the case of a (+1,0) diffraction order exciting the resonance :

$$\lambda_r = dn\sqrt{1 + \frac{S_0^4 tan^2(\phi) k_w^2 n^2}{(k_w n)^2 - (\pi/a)^2}} \tag{3.55}$$

Derivative of this expression in regard of the refractive index leads to the definition of sensitivity of the array which gives :

$$S = \frac{d\lambda_r}{dn} = \frac{\lambda_r}{n} \tag{3.56}$$

The sensitivity and the FWHM calculated using CMT are plotted in Fig 3.32 along with the results obtained using this last equation. Sensitivity is exactly proportional to λ_r/n even if

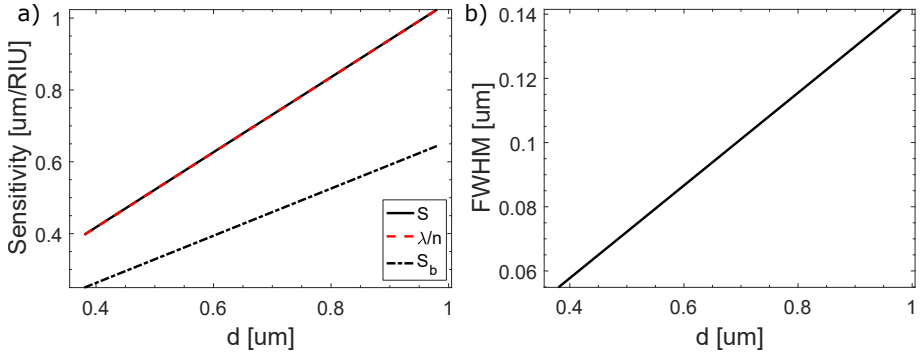


Figure 3.32 a) Sensitivity and b) FWHM of the square nanohole array obtained as a function of period with constant opening of the slit $a = 0.45d$ and thickness $h = 0.2d$. The sensitivity equation given by the zero order approximation of Eq 3.46 is given by the dashed black lines.

this last equation was obtained using the approximation of the zero order only. As was the case for the slit array, all other diffraction orders considered in the sum of G will modify the value of the position of the resonant wavelength, but the derivative with regards to the refractive index holds the same relationship with the resonant wavelength for a PEC. The FWHM also depends linearly on the position of the resonance, so the resolution of the array will be dependent on the quality factor of the peak only.

In order to highlight the effect of the size of the hole, the transmission spectrum of the square hole array is presented for 3 different hole size, as well as the value of the reflection coefficient (Fig 3.33). Having a smaller hole size again leads to a higher value of the coefficient reflection and thus improves the quality factor of the resonance. It also brings closer together both resonant modes since the propagation factor associated with the tan/cot functions are reduced. The product of the reflection coefficient can reach values as high as $|\rho_{21}\rho_{23}| = 800$ for a PEC ; these high values compensate the amplitude lost relative to the evanescent propagation inside the holes.

Resolution of the array is plotted as a function of the period in Fig 3.34 for 3 different cases : 1- The ratio of a, h in comparison to d is kept constant (black curve). For a PEC, the optical properties of a structure are similar for a constant ratio of the dimension of the array compared to the wavelength. The resolution is in that case *independent* of the period. 2-Only the ratio $h = 0.4d$ is kept constant, and $a = 0.225\mu m$. This case of a constant thickness compared to the other parameters shows poorer sensitivity as the thickness decreases. An interesting discussion in Martin-Moreno et al. (2001) highlights the fact that the width of the resonance will depend upon the lifetime of the surface mode with value given by $t_{rad} \approx 1/ck_z$. For small thicknesses the surface mode couple more strongly to radiative modes and will thus lead to a broaden peak. 3-Only the ratio $a = 0.5d$ is kept constant, and $h = 0.1\mu m$. Reduction of the relative size of the hole (red dashed line) has a similar effect than for slit arrays and increases the reflection at the interface, which reduces the FWHM, and improves resolution.

Field distribution and surface sensitivity

The field for a square array are plotted in Fig 3.35 Image a) of Fig 3.35 presents a side view of the nanohole at the plane $Y = 0$. Strong localization of the fields is located at the apex of

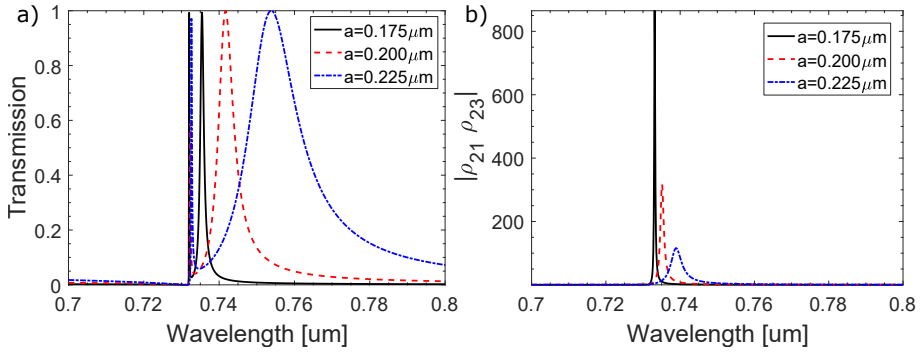


Figure 3.33 a)Transmission spectra and b) Reflection coefficient for a square hole array of period $d = 0.55\mu m$ and thickness $h = 0.075\mu m$ for 3 different hole sizes

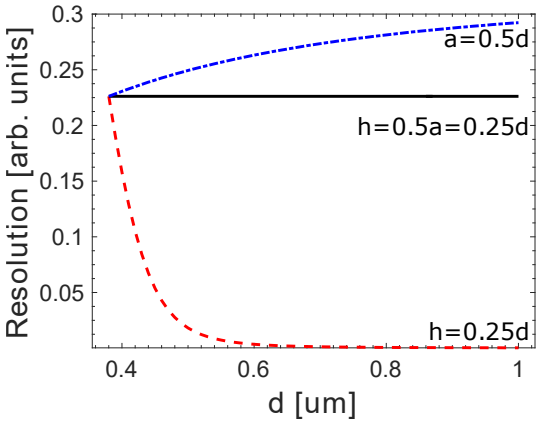


Figure 3.34 a) Resolution of the square hole array (Eq 3.2) for 3 different cases. 1- The hole size and thickness $a = 0.5h = 0.25d$ are kept proportional to the period. 2- Thickness is kept proportional $h = 0.25d$ while the hole size is constant $a = 0.1\mu m$. 3- Hole size is kept proportional to the period $a = 0.5d$ while the thickness is kept constant $h = 0.2\mu m$

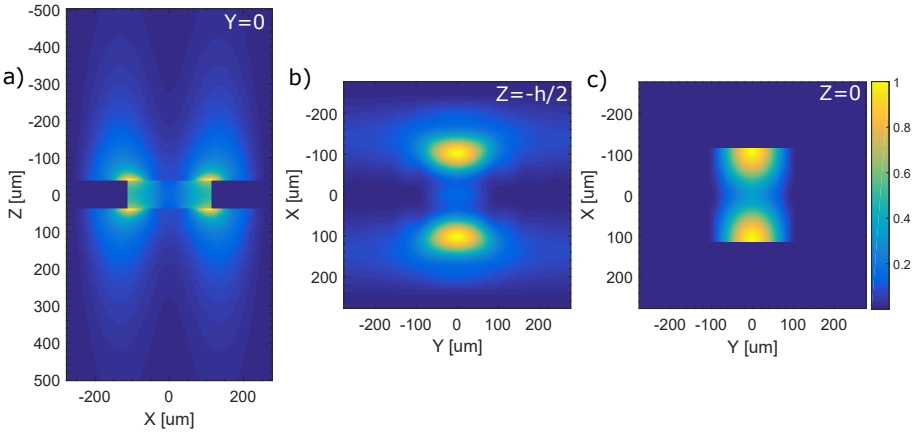


Figure 3.35 a) Electric Field Norm $|E|^2$ at plane coordinate $Y = 0$ of a square hole array of period $0.55\mu m$, thickness $h = 0.075\mu$ and hole width $a = 0.225\mu m$. b) Fields at the upper interface of the hole ($Z = -h/2$). c) Fields inside the hole ($Z = 0$) which corresponds to the summation of rectangular waveguide TM and TE modes.

the structure where the coupling between plane waves of Region 1 and 3 and guided modes in region 2 is maximum. A top view of the electric field at the interface $z = -h/2$ in Fig 3.35b) shows in greater details the field localization at the interface of the hole in region 1, which corresponds to a summation of impinging light and reflected diffraction orders. The way all the diffracted orders reflect (with their respective amplitude) and interferes with each other gives the electric field its shape near the hole. The plot in 3.35c) shows the $|E|$ fields inside the hole, which corresponds to a summation of guided modes. The strong contribution of the $|E_x|$ field of the TE_{10} and TM_{12} which are sinusoidal function of x and y are evident. The overlap between the two fields illustrates the way the optical transmission mechanism takes place.

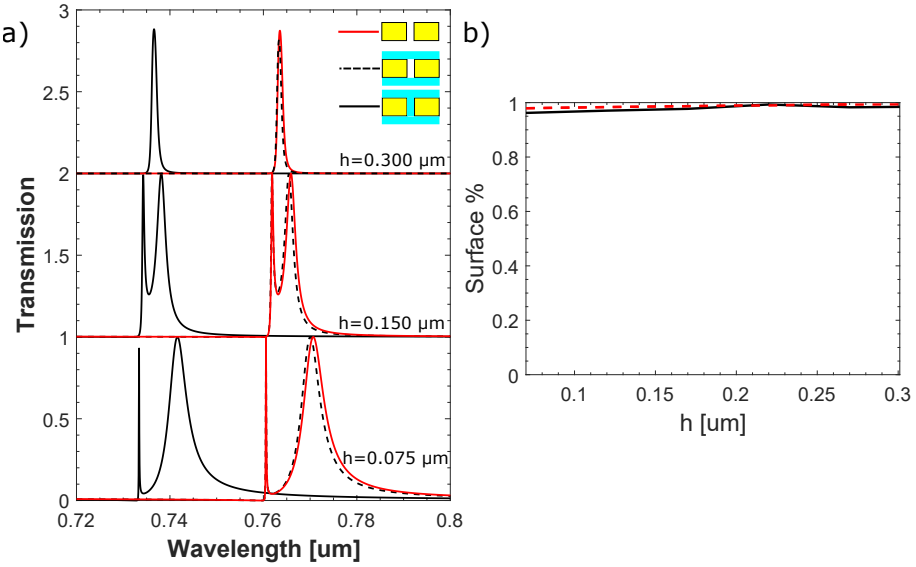


Figure 3.36 a) Transmission spectra for square nanohole period $0.55\mu m$ and slit opening $a = 0.2\mu m$ for 3 different thickness and different refractive index for the different regions. Red line is for a refractive index of 1.33 for all region. Black dashed line is the transmission for a refractive index to 1.43 inside the holes only (Region 2) and the dotted black line for this change for the surfaces of the holes only (Region 1 and 3). The black line represents the shift for a change of refractive index in all regions. b) Black line - Percentage of the shift in resonance peak position due to the change of refractive index at the surface as a function of thickness. Red dashed line - Field integral percentage of the field contained on the surface of the array.

In Fig 3.36a) the shift of the peak upon changes of refractive index for the surfaces only, for the hole only and for all region is plotted. Most of the shift is a consequence of a change of refractive index at the surface. This is another feature of the truly surface bound state of the resonance for square hole array, which concentrates most of the light on the surface. We can see in Fig 3.36b) that this proportion is almost constant near 95%.

3.7.2 Case of real metal

In this section we use SIBC in order to implement the effect of considering finite dielectric constant for the metal. The data of gold from *Johnson and Christy* Johnson and Christy (1972) are used for gold. The propagation constant inside the hole is also modified to meet the conditions of penetration inside the metal walls using Eq 3.15.

Resonance conditions

The transmission spectra of nanosquare arrays of periodicity $d = 0.55\mu m$, hole size $a = 0.2\mu m$ and several thicknesses is plotted in Fig 3.37a) for the case of gold (black line). In order to show the agreement with numerical methods the transmission spectra obtained with FEM is plotted in dashed red lines. The effect of the losses induces by the gold metal broadens the

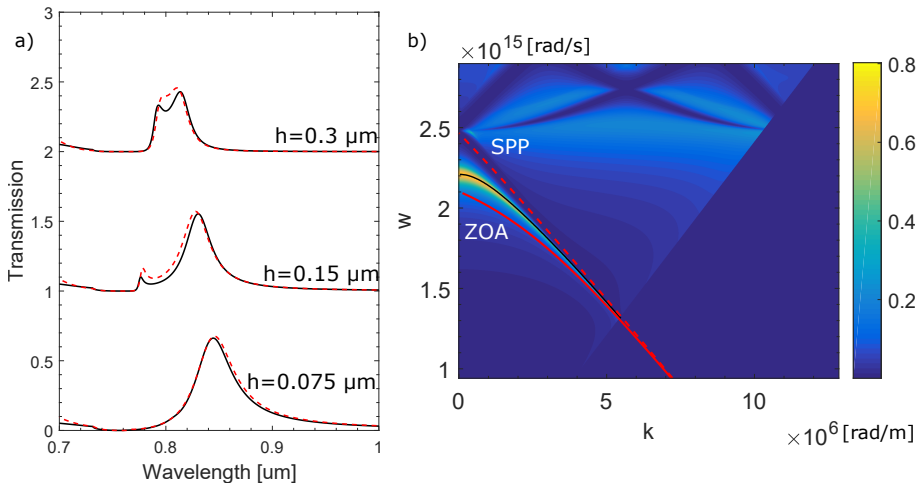


Figure 3.37 a) Transmission spectra of square nanohole arrays obtained using CMT for period of $0.55\mu m$ with hole size $a = 0.2\mu m$ for the case of gold metal (black lines). Results of FEM simulation is plotted in red dashed lines b)Dispersion relation of nanoslit array of dimensions $d = 0.55\mu m$, $h = 0.075\mu m$ and $a = 0.2\mu m$. The red dashed line is the dispersion relation obtained using the ZOA (Eq 3.50). The black lines are resonance conditions given by Eq 3.51. The red dashed line corresponds to the dispersion of an SPP on a flat surface, and coincides with the Wood anomaly following Eq 3.48.

Wood Anomaly condition up to the point that the asymmetrical mode only emerges under certain dimensions of the array. The peak is redshifted and its transmission is reduced : this is due to the reflection coefficient's magnitude not fully matching the losses induced by the evanescent propagation.

The dispersion relation with the consideration of the metal can be retrieve using Eq 3.50, and is plotted in Fig 3.37 as the red line. The relation is red-shifted compared to the PEC case,

which is mainly due to an increase in the propagation constant value of the mode inside the hole, which leads the resonant condition of Eq. 3.51 towards longer wavelength. Alongside the dispersion relation of the nanohole array is the one for SPP excited on a flat surface (red dashed curve). For a square hole array with a hole size small enough to be above cutoff, the propagation inside the hole won't contribute to the resonance condition and the resonance will be a consequence of the bounded surface mode. The maxima is thus always next to the Wood Anomaly. This resonance resembles a SPP with a similar wavevector, but affected by a small phase delay which can be attributed to the presence of the hole, which changes the effective conductivity of the metal Liu and Lalanne (2008).

Sensitivity and resolution

The sensitivity of the array is plotted in Fig 3.38. The bulk sensitivity corresponds to the black dashed-dotted line which takes values of about half the full sensitivity since, for the case of $n_1 = n_3$, the fields are equally distributed between the two interfaces. An interesting case of sensitivity for changes of refractive index for all regions is plotted in the full black line and compared to the value λ/n. The sensitivity is very similar to the perfect metal case, as was pointed out for the slit array case (see discussion in Section 3.6.2). Since the resonance corresponds to a bounded surface state we compare the sensitivity to the one of an SPP on a flat surface. As was observed on the dispersion relation, the presence of holes modifies the condition of resonance compared to a flat surface, which moves the resonances towards longer wavelength, and has thus an influence on the sensitivity which is proportional to the wavelength at which the resonance occurs. Since this modification is small the two sensitivities will still be similar. Although the bulk sensitivity, which is the effective sensitivity when we take into consideration the substrate, is only a fraction (0.5-0.8 for the periods considered) of the total sensitivity. The reflection coefficient includes loss when we consider a real metal and will no longer compensate fully the evanescent attenuation of the propagation inside the hole, as shown in Fig 3.39. This leads to transmission reaching lower values than for the slit arrays since the later structure could benefit from propagative propagation. The propagation constant inside the hole is greatly modified by considering the real case of the metal, as can be observed from Fig 3.40. First, the cutoff condition is highly redshifted, up to a change from 600 nm to 800 nm for the particular case of a hole size of $a = 0.225\mu m$ with gold. Penetration of the fields inside the walls extends the field distribution, which leads to a smaller transverse vector component, and thus a higher longitudinal one. This propagation factor also always include an imaginary part related to losses in the metal walls. This will influence not only the propagation factor but also the overlap integral, leading to a redshift of the reflection coefficient peaks as well as a reduction in their amplitudes (see Fig 3.39a and

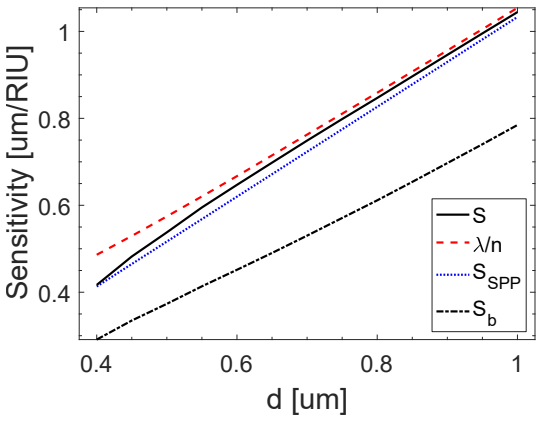


Figure 3.38 Sensitivity (black line) of a square hole array as a function of period for a hole size of $a = 0.35d$ and thickness $h = 0.3d$. The comparison with the perfect conductor case equation λ_r/n (red dashed line) and the SPP sensivitiy for a flat surface (blue dotted line). The bulk sensitivity, corresponding to a change of refractive index in region 1 and 2 only, is in the black dotted-dashed line.

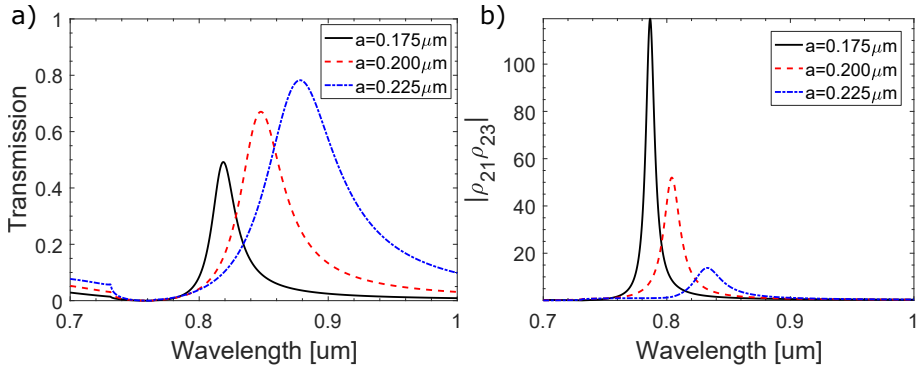


Figure 3.39 a) Transmission spectrum and b) Reflection coefficients for a gold square hole array of period $0.55\mu m$ and thickness $h = 0.150\mu m$ for 3 different hole width.

b). The FWHM and depth in this case do not depend monotonically upon the dimension of

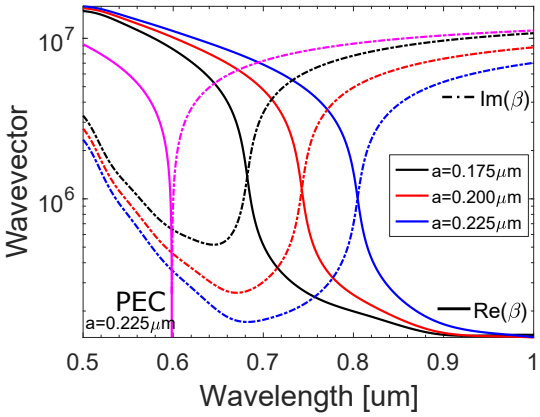


Figure 3.40 Imaginary and real components of the propagation vector inside the holes for 3 different hole width. These values are compared with the propagation constant of a square hole of $0.225\mu m$ for a PEC (magenta).

the array. Small value of the thickness leads to broad resonance peak since the lifetime of the resonance is greater on the surface, where it can couple to leaky modes. But thicknesses too large lead to strong evanescent attenuation. A small hole size also increases the evanescent nature of the propagation as well as the loss linked to the propagation inside the hole, and leads to strongly attenuated resonance, while holes too large reduce the reflectivity and thus the finesse of the resonance. Resolution of the array was calculated for different periods as a function of both hole widths and layer thicknesses, and an optimal value was determined each time, as illustrated in the inset of Fig 3.41a). The hole width and thickness that achieved this optimal resolution as well as the resolution value are plotted in Fig 3.41 a and b). The value ranges around $0.3d$ for both the thickness and hole size.

Field distribution

In Fig 3.42a) the $|E|$ fields are plotted for the plane $Y = 0$. High field concentration is located at the apex of the hole and almost no field inside the hole, which is expected since the field exhibits an exponential decay inside the holes. For the case of matching index substrate, the resonance is symmetrical and thus leads to half the surface fields being located inside the substrate. In the square hole type structure no strong field localization is observe inside the hole. The proportion of the fields located for surface sensing with the top surface usually ranges to about 40% of the total fields.

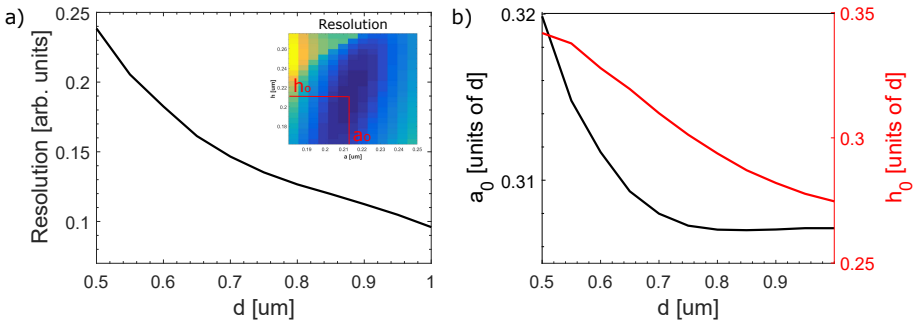


Figure 3.41 a) Resolution of the square hole array at optimal thickness and hole size as a function of the period of the array for the case of a matching index substrate. *inset* Resolution of the array as a function of hole size and thickness for a periodicity of $d = 0.45\mu m$. b) Value of the optimal thickness and hole width for each period of the square hole array.

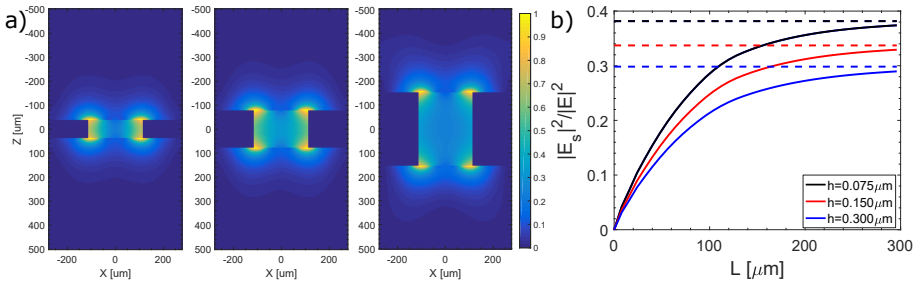


Figure 3.42 a) Electric field norm $|E|$ for a nanosquare hole array of period $0.55\mu m$ and hole opening $0.225\mu m$ for 3 different thicknesses $h = 0.075\mu m$, $0.15\mu m$ and $0.3\mu m$ with an index matching substrate. b) Field percentage contained within a layer of thickness L on the top surface of the array for 3 different thicknesses of the metal film considered.

3.7.3 Case $n_1 \neq n_3$

Resonance conditions

If we consider the presence of a glass substrate on one side of the array, the resonance exhibits a higher number of peaks and Wood minimas, as is illustrated in Fig 3.43 a). If we consider Eq 3.51, the reflection coefficient will show high values for two different wavelength which corresponds to both interfaces. The condition given by Eq 3.48 is the same for slits and square holes which leads again to multiple Wood anomalies condition as is illustrated in the dispersion relation in 3.43b). The resonant peak in this case are of smaller magnitude since they do not reinforce each other after a bouncing of the wave inside the indentation. The resonance is in a certain way "split" into its two contributions of the different interfaces, which interact with each other through the evanescent wave inside the hole.

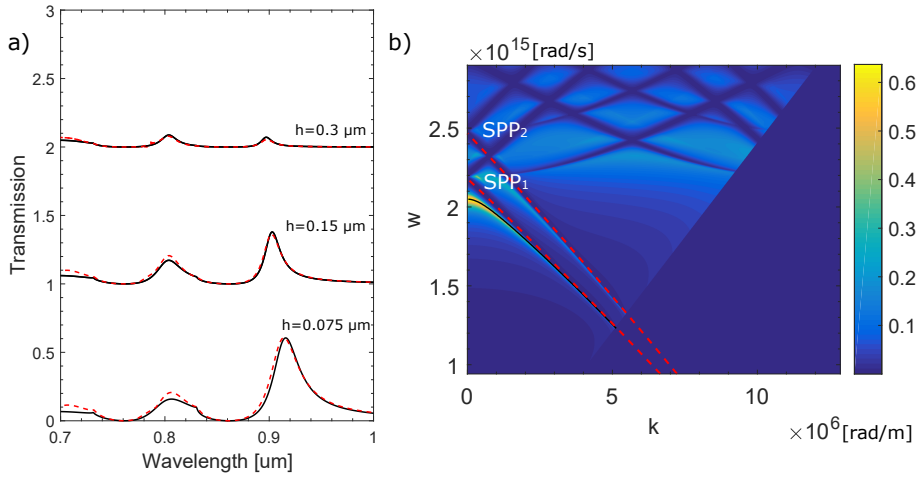


Figure 3.43 a) Transmission spectra of square nanohole array with a glass substrate obtained using CMT. The period is $0.55\mu m$ with a hole size of $a = 0.2\mu m$ and the case of gold metal (black lines) is plotted. The red dashed line correspond to numerical calculation made using FEM b)Dispersion relation of nanoslit array of dimensions $d = 0.55\mu m$, $h = 0.1\mu m$ and $a = 0.20\mu m$ with glass as the substrate. The black line is the resonance condition given by Eq 3.51. The red dashed lines corresponds to the dispersion of an SPP on a flat surface (on interface 1 and 2), and coincides with the Wood anomaly following Eq 3.48.

Sensitivity and resolution

For sensitivity of the array one needs to concentrate on the peak related to the resonant condition for the 1-2 water-hole interface, which for Fig 3.43a) corresponds to the second to last most redshift peak. A change in refractive index will only lead to strong shifts of resonant wavelength for this peak. It can be noted that a change of refractive index in region 1 and 2

still leads to a shift of the peak related to the interface $2-3$ of glass of $2\%-5\%$ approximately, because of the interaction of the resonance. The bulk sensitivity S_b, as plotted in Fig 3.44 is higher than the case of matching index since the resonance state does not exhibit high fields located inside the substrate. For this reason the bulk sensitivity almost reaches the total sensitivity of λ/n which is the limit corresponding to the PEC case. We also observe that the bulk sensitivity reaches values similar to the case of a SPP on a flat surface but with a slight decrease due to the effect of the hole on the propagation constant. Resonance

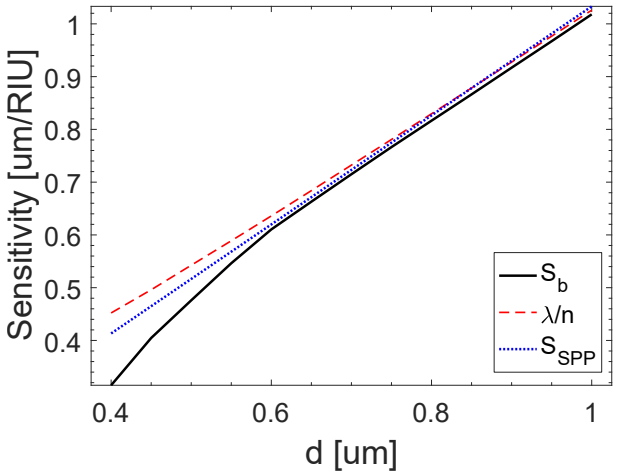


Figure 3.44 Bulk sensitivity (black line) of square hole array as a function of the period for a hole size of $a = 0.3d$ and thickness of $h = 0.25d$. The values are compared to the sensitivity of a PEC given by λ/n (red dashed line) and the sensitivity of a SPP on a flat surface (blue dotted line)

of the hole array with a higher index substrate still exhibits an optimal width and thickness for improved resolution, which is plotted in Fig 3.45. The value for the optimal thickness is a little smaller, ranging to about $0.25-0.33d$, while the hole size ranges in between $0.3-0.31d$ depending on the period.

Field Distribution

The field distribution for a square nanohole array with glass substrate are presented in Fig 3.46 a) for 3 different thickness, at the plane $Y = 0$. An interesting feature of the resonance of hole array with higher index substrate is that the coupling field at the apex is located on one interface only. This leads to a higher proportion of the total fields being located in the useful surface region for sensing as plotted in Fig 3.46b), compared to the case of a matching index. For $0.3\mu m$ film the proportion on the top surface can reach most of the surface field, with a percentage of around 55%.

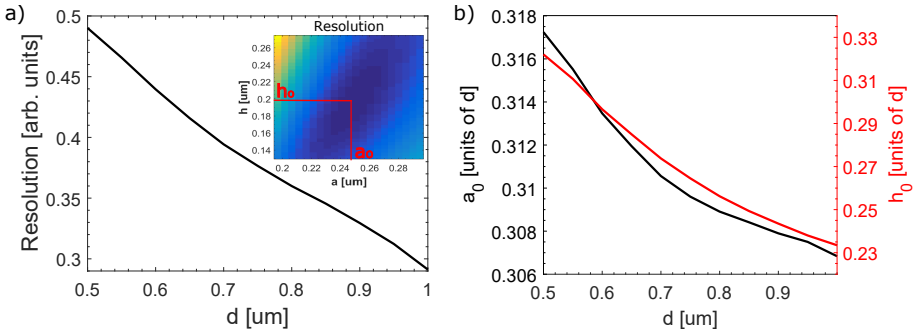


Figure 3.45 a) Resolution of the square hole array at optimal thickness and hole size as a function of the period of the array for the case of a glass substrate. *inset* Resolution measurements as a function of the hole size and metal thickness for the period $d = 0.7\mu m$. b) Optimal values of the thickness and hole size for each period considered.

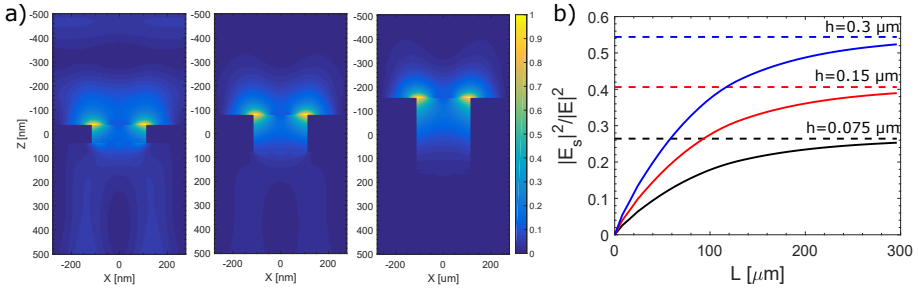


Figure 3.46 a) Electric field norm $|E|$ for a nanosquare hole array of period $0.55\mu m$ and hole opening $0.2\mu m$ for 3 different thickness $h = 0.075\mu m$, $0.15\mu m$ and $0.3\mu m$ with glass as the substrate. b) Field percentage contained within a layer of thickness L on the top surface of the array for 3 different thickness of the metal film considered.

3.7.4 Square hole arrays - Conclusion

— Sensitivity for nanosquare array with PEC reaches λ/n. For a real metal this value is a very good approximation.

— The square hole array is characterized by a cutoff frequency, which depends upon the hole size. The transmission properties will thus be greatly influence by that parameter.

— For a PEC the FWHM increases in the same fashion than the sensitivity, so the sensing resolution will depend upon the quality factor of the resonant peak.

— Reducing the thickness of the array leads to broader resonant peaks since the lifetime of the resonance is diminished. Having a too large thickness induces a high evanescent attenuation and leads to small transmission only. A compromise must be made to achieve optimal performances.

— For the hole size, having a too small hole leads to an increased cutoff frequency and an increased evanescent attenuation. Furthermore, losses relative to propagation in the hole for a real metal will also increase. Having a large hole leads to broad peaks since the reflectivity at the interface is diminished. A compromise must thus be made to achieve optimal sensing performances.

— An optimal thickness and hole size can be retrieve for each period and corresponds to a maximal quality factor of the peak. For the case of matching refractive index substrate this value ranges at around $0.4 - 0.5d$ for the hole size and $0.3 - 0.4d$ for the thickness. For the case of a glass substrate these values reach $0.4 - 0.35d$ and $0.08 - 0.12d$. Note that for a circular hole array an approximate equivalent diameter can be expressed by the quick formula $r = 1.84a/\pi$, where r is the radius and a the side of the square.

— Resonances with nanohole array usually have little fields located inside the hole. Furthermore, when a different index is used for the substrate, the resonance will be resulting from the surface mode of a single interface, leading to most of the field located on that interface. This is an advantage for thin film sensing.

3.8 Conclusion

The sensitivity and resolution properties of both 1-D nanoslit array and 2-D nanosquare arrays have been reviewed. Using coupled mode theory, the transmission properties and resonance conditions of this type of nanostructure were studied through their parameters of periodicity, hole size and metal thickness.

The mechanism of resonance for a PEC involves the multiple diffraction of light at the surface, for which the rate of change of the resonant wavelength scales as λ/n. Since the dielectric

constant of the metal has negligible effect on the dispersion relation, this relation is a good approximation when the metal is not a PEC. Sensitivity at the top surface is weighted by the proportion of the fields located in this region, which unfortunately usually means that it is reduced to at least to half the total sensitivity. This is the reason why performances of nanohole arrays are usually low compared to SPR sensors based on the Kretschmann configuration.

Since the FWHM is proportional to λ, the optimal resolution has more to do with the quality factor of the resonance than the wavelength of resonance. It was determined that optimal resolution may be achieved with specific dimension for both types of arrays. These dimensions can also be tuned for optimal sensing of a specific layer layer thickness.

Using a matching index substrate led to improve bulk sensitivity for both nanoslit arrays and nanosquare hole array. This is a consequence of improved quality factor of the resonance since it is reinforce by both surfaces. For nanoslit array a large portion of the field is always located inside the substrate, and an other portion may be located inside the hole when the thickness is large, leading to lower surface sensing capabilities.

Experimental reports of performances of nanoholes do not to this day match the performances of SPR system based on Kretchmann configuration, and, even thought it was demonstrated in this paper that the nature of the resonance in nanohole array based sensors limits the achievable performances, the limits of detection are still comparable. Fully integrated multiplexed system are starting to prove their actual efficiency at performing complete profile of analytes. The great advantages of high-throughput makes nanohole array a interesting tool for medical diagnostic, and should lead to even greater applications in the years to come.

CHAPITRE 4 ARTICLE 2 : OPTICAL TRANSMISSION THEORY FOR METAL-INSULATOR-METAL PERIODIC NANOSTRUCTURES

Cet article publié dans *Nanophotonics* correspond à un modèle pour la transmission de nanostructure périodique dans un système métal-diélectrique-métal à l'aide de la méthode des modes couplés. Le but était de comprendre plus en détail les propriétés optiques du matériau. Cet article mettait de l'avant plus particulièrement une méthode pour calculer les propriétés optiques de structure en lames, qui comportent des réseaux de diffraction. Il s'agit donc d'un problème classique de Fabry-Pérot, mais dont les réflexions aux interfaces comportent différents coefficients possibles, selon les ordres de diffraction excités. Il faut donc considérer une infinité de chemins différents, qui peuvent réfléchir une infinité de fois aux interfaces. Ce problème fut résolu en introduisant une méthode originale, appelée méthode des matrices de connexion, qui fait intervenir des séries géométriques de matrices.

4.1 Auteurs

André-Pierre Blanchard-Dionne et Michel Meunier

4.2 Abstract

A semi-analytical formalism for the optical properties of a metal-insulator-metal periodic nanostructure using coupled-mode theory is presented. This structure consists in a dielectric layer in between two metallic layers with periodic one-dimensional nanoslit corrugation. The model is developed using multiple-scattering formalism, which defines transmission and reflection coefficients for each of the interfaces as a semi-infinite medium. Total transmission is then calculated using a summation of the multiple paths of light inside the structure. This method allows finding an exact solution for the transmission problem in every dimension regime, as long as a sufficient number of diffraction orders and guided modes are considered for the structure. The resonant modes of the structure are found to be related to the metallic slab only and to a combination of both the metallic slab and dielectric layer. This model also allows describing the resonant behavior of the system in the limit of a small dielectric layer, for which discontinuities in the dispersion curves are found. These discontinuities result from the out-of-phase interference of the different diffraction orders of the system, which account for field interactions at both inner interfaces of the structure.

4.3 Introduction

Surface plasmons are the oscillations of conductive electrons that propagate at the interface of dielectrics and highly conductive metals. They are excited in resonance with electromagnetic waves using momentum matching with the parallel wavevector of the incident wave. With the arrival of fabrication techniques that can achieve resolution well below the wavelength of electromagnetic waves in the visible spectrum, new structures in metals have opened up possibilities to couple and manipulate such surface waves (Barnes et al., 2003). These nano-plasmonic devices have shown to have very unique properties ; they canconcentrate light well below the diffraction limit (Gramotnev and Bozhevolnyi, 2010; Choo et al., 2012), they can lead to large field amplification (Schuller et al., 2010), as well as achieve long-range propagation of the surface waves (Oulton et al., 2008). They constitute a good way of designing materials with unique properties (Shen et al., 2005; Drezet et al., 2008), as well as novel optical devices (Ferry et al., 2008; Ebbesen et al., 1998).

In this letter, we develop an analytical formalism for a combination of two structures of interest : (i) a metalinsulator- metal (MIM) structure, with (ii) periodic indentation in the metal films, as depicted in Fig 4.1. Periodic corrugations in metal thin films have shown to exhibit interesting optical properties ever since it was first reported that nanohole arrays lead to extraordinary optical transmission (Ebbesen et al., 1998). These structures constitute a unique way to couple to surface waves (Genet and Ebbesen, 2007). As the understanding of the transmission mechanism improved, the high transmission observed in this structure were linked not only to the surface plasmon waves but also to surface waves of the corrugated surface for the case of perfect electrical conductors (PECs) (Pendry et al., 2004). Planar MIM structures, on their part, have been investigated theoretically for decades now (Economou, 1969) and have gain interest recently with new experimental demonstrations (Choo et al., 2012; Kurokawa and Miyazaki, 2007; Hill et al., 2009) as well as extended analysis for integration into nanoscale devices (Dionne et al., 2005). The optical properties of such a multilayer structure with periodic corrugation can be obtained using the coupled mode theory. The proposed model includes the calculation of the reflection and transmission coefficient of the interfaces as a semi-infinite medium and a multiple path calculation. This last part corresponds to the combinative solution of a multilayer Fabry-Perot in which one layer acts as a diffraction grating layer. The model is developed in order to obtain physical insights into the resonant states involved in the transmission of light through such a structure.

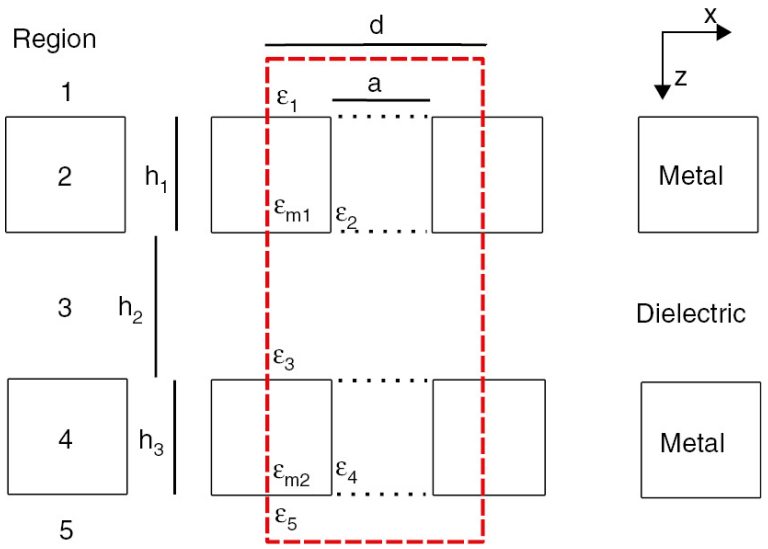


Figure 4.1 Unit cell representation of the periodic MIM structure. The dashed rectangle represents the structure with periodicity d ; slit width a ; and thicknesses h_1, h_2, and h_3 for the top metal, dielectric, and bottom metal layers, respectively.

4.4 Theoretical model

4.4.1 Scattering Coefficient

The theoretical model presented here uses the coupled mode theory in the multiple scattering formalism (Martin-Moreno et al., 2001; Bravo-Abad et al., 2004b; Garcia-Vidal and Martin-Moreno, 2002; Martín-Moreno and García-Vidal, 2008; Garcia-Vidal et al., 2010). The structure studied in this paper consists in a dielectric layer of thickness h_2, in between two corrugated metallic layers of thicknesses h_1 and h_3. The periodicity of the system is d and the slit width is a. The dielectric constants of region i are given by ϵ_i (for the metallic layer, this corresponds to the dielectric constant of the material inside the slits), and ϵ_{m_j} for the metals. For simplicity of the method and annotation, as well as for a focus on the interesting case of coupling to surface waves, we consider here only the one-dimensional case of slit arrays, for which the field is invariant along the y-axis, and the p-polarized wave. The metal is considered to be a perfectly flat PEC, but could be implemented as a real metal using surface impedance boundary conditions (Garcia-Vidal et al., 2010). The magnetic fields for each layer are defined as solutions to the Helmholtz equation for the considered medium, whether it is a plane wave in a dielectric medium or a guided wave inside the indentation of the metallic layers, as depicted in Fig. 4.2. The notation used for the fields is the one presented in a review article (Garcia-Vidal et al., 2010) where $|k\rangle = e^{i(k_0+k_r n)x}$ represents the parallel component (or x-component) of the electromagnetic field of a plane wave, with the

wavevector $k_{0_i} = k_w\sqrt{\epsilon_i}\sin\theta_i$ with θ_0 the incident angle and $kw = w/c$ the wavevector of light in free space. The waves in dielectric media are represented by a Bloch combination of plane waves $k = k_0 + k_r n$, which represents the different diffraction orders n of the grating. This representation is valid for an infinite array of slits. For the guided modes inside the slits, $|\alpha\rangle = \frac{C_t}{\sqrt{a}}\cos\frac{(m(x+a/2))}{a}$ represents the parallel component of the guided TM m mode for parallel-plate waveguides [18], where C_t is a normalization constant relative to the waveguide mode and equals 1 if $m = 0$ and $\sqrt{2}$ if $m > 0$. The z-component of the wavevectors is retrieved using $k_w^2 = k^2 + k_z^2$ for the plane wave and $k_w^2 = q_z^2 + (m\pi/a)^2$ for mode m inside the slits.

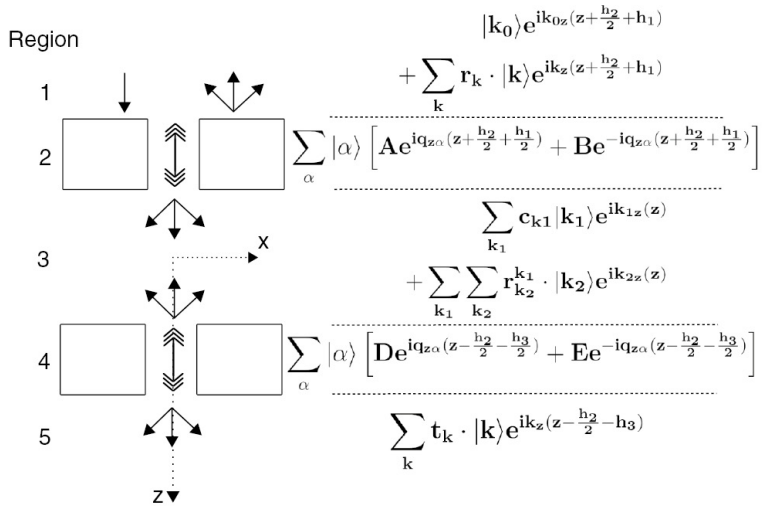


Figure 4.2 Field definition for each region of the structure.

The transmission and reflection coefficients are obtained, using the convention given in Ref. (Garcia-Vidal et al., 2010), by matching the fields at each interface and then taking a projection over all $\langle k|$ for the electric fields and over all $\rangle\alpha|$ for the magnetic part. This leads to a set of equations for each interface, as follows :

1. Interface 1-2

$$(G_{\alpha\alpha} + iY_\alpha)\tau_\alpha^{12} + \sum_{\alpha\neq\beta} G_{\alpha\beta}\tau_\beta^{12} = 2iY_{k_0}\langle k_0|\alpha\rangle$$
$$\rho_{k_1}^{12} = -\delta_{k_0,k_1} + \sum_\alpha \langle k_1|\alpha\rangle\tau_{\alpha,k_1}^{12} \tag{4.1}$$

2. Interface 2-3

$$(G_{\gamma\gamma} + iY_\gamma)\rho^{23}_{\alpha\gamma} + \sum_{\beta\neq\gamma} G_{\alpha\beta}\rho^{23}_{\alpha\beta} = iY_\gamma\delta_{\gamma\alpha} - G_{\gamma\alpha}$$
$$\tau^{23}_{\alpha,k} = \langle k|\alpha\rangle + \sum_{\beta} \rho^{23}_{\alpha\beta}\langle k|\beta\rangle \tag{4.2}$$

3. Interface 3-4

$$(G_{\alpha\alpha} + iY_\alpha)\tau^{34}_{\alpha} + \sum_{\alpha\neq\beta} G_{\alpha\beta}\tau^{34}_{\beta,k} = 2iY_k\langle k|\alpha\rangle$$
$$\rho^{34}_{k_1,k_2} = -\delta_{k_1,k_2} + \sum_{\alpha}\langle k_2|\alpha\rangle\tau^{34}_{\alpha,k_1} \tag{4.3}$$

where τ^{12}_{α} represents the transmission coefficient for interface 1–2 of mode α, and $Y_k = \epsilon_i k_w/k_z$ represents the admittance of p-polarized wave. $Y_\alpha = q_z/k_w$ is the admittance of the TM mode inside the slit. $\rho^{23}_{\alpha\gamma}$ represents the reflection coefficient of mode α into mode γ, and $\tau^{34}_{\alpha,k}$ represents the transmission into mode α of incoming k wavevector. $G_{\alpha\alpha} = i\sum_k Y_k\langle k|\alpha\rangle\langle\alpha|k\rangle$ describes the coupling term of incident wave to the waveguide mode α with plane vectors $|k\rangle$, and must run over a sufficient number of diffraction orders. It includes, for each wavevector, the overlap integral for one-dimensional slit arrays :

$$\langle k|\alpha\rangle = \frac{C_t ik}{\sqrt{ad}}\int_{-a/2}^{a/2}\cos(m\pi a(x+a/2))e^{ikx}dx$$
$$= \frac{C_t ik}{\sqrt{ad}}\frac{e^{ika/2}\cos(m\pi) - e^{-ika/2}}{(m\pi/a)^2 - k^2} \tag{4.4}$$

The reflection and transmission terms for all the other interfaces can be retrieved by applying Eqs. (1)–(6) in a similar way. In region 3, the waves are represented by a superposition of incoming diffraction orders and reflected ones, denoted by k_1, k_2.

4.4.2 Multiple path calculation

Because of the difference of impedance of each medium involved in the MIM structure, the waves that propagate inside this structure will experience multiple reflections and transmissions at each interface. These reflections can occur an infinite number of times, and their summation is represented by a geometric series. Transmission "loops" can be defined inside the structure in order to enumerate every possible path of light inside the structure. In a multilayer system like the MIM structure, each layer and combination of layers will behave as a possible "loop" of the transmission. Fig. 4.3 represents the different loops possible in the four-interface MIM structure. The total transmission becomes a complex summation of

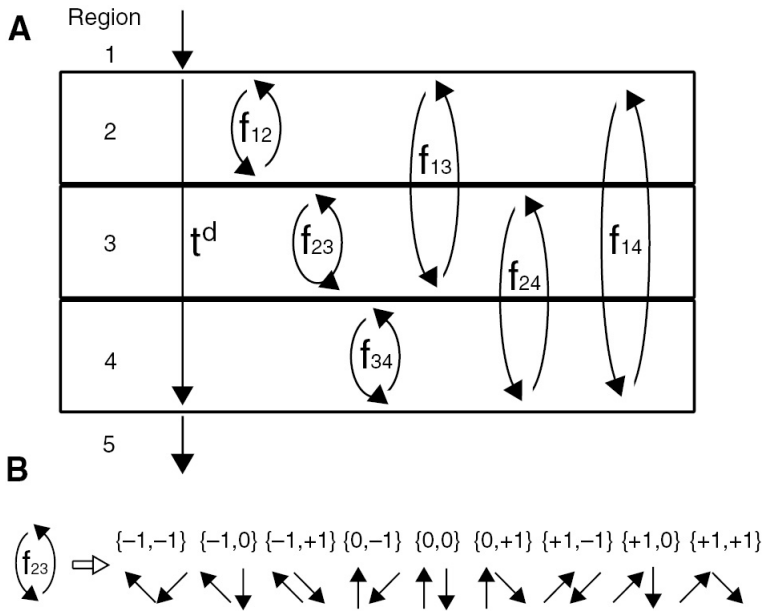


Figure 4.3 (A) The different loops inside the MIM structure. (B) The expansion of loop f_{23} by taking into account the first diffraction orders.

all possible paths, which will define how the fields inside each layer interact with each other. Light can be transmitted directly, as represented by the td arrow in Fig. 4.3, or can go through a series of loops of the system before being transmitted. Loops can also exist inside other loops. Waves inside the slits can propagate as different modes of the parallel plate waveguide, so all possible loops containing these regions can be expanded into the different combinations of the guided modes considered. Furthermore, plan waves in region 3 can propagate as diffraction orders of the periodic system, as described by the indices of the reflection and transmission coefficients $\tau^{34}_{\alpha,k}$, $\tau^{23}_{\alpha,k}$, $\rho^{34}_{k_1,k_2}$ $\rho^{32}_{k_1,k_2}$. Every loop containing this region, i.e. f_{23}, f_{13}, f_{24}, and f_{14}, must be expanded into combinations of diffraction orders both coming back and forth. In Fig. 4.3B, an example of the different loop combination of f_{23} is given for orders –1, 0, +1.

In this calculation, a sufficient number of diffraction orders and guided modes must be taken into consideration. Whenever $\epsilon_i k_w \sin(\theta) + \frac{m2\pi/d}{<} k_w\sqrt{\epsilon_i}$, the diffraction order inside the medium becomes evanescent, and so the term e_h will become significantly small. As for the guided modes, as only the fundamental mode for the metallic slits couples strongly to the plane waves of regions 1, 3, and 5, only this mode is considered for the remainder of the article. The loop factors, with diffraction order (–1, 0, +1) considered for region 3 and only the transverse electric and magnetic (TEM)-guided mode considered in regions 2 and 4 ($\rho^{23}_{|0\rangle,|0\rangle}$

is written ρ^{23}), can be expressed as

$$\begin{aligned} f^{12} &= \rho^{23}\rho^{21}e_{h_1}^2 \qquad\qquad f^{34} = \rho^{45}\rho^{43}e_{h_3}^2 \\ f_{k_1,k_2}^{23} &= \rho_{k_1,k_2}^{34}\rho_{k_1,k_2}^{32}e_{h_2}(k_1)^2e_{h_2}(k_2)^2 \\ f_{k_1,k_2}^{13} &= \rho_{k_1,k_2}^{34}\tau_{k_2}^{32}\rho^{21}\tau_{k_1}^{23}e_{h_1}^2e_{h_2}(k_1)^2e_{h_2}(k_2)^2 \\ f_{k_1,k_2}^{24} &= \rho^{45}\tau_{k_1}^{43}\rho_{k_1,k_2}^{32}\tau_{k_2}^{34}e_{h_3}^2e_{h_2}(k_1)^2e_{h_2}(k_2)^2 \\ f_{k_1,k_2}^{14} &= \rho^{45}\tau_{k_1}^{43}\rho^{21}\tau_{k_2}^{23}\tau_{k_2}^{34}e_{h_2}(k_2)e_{h_2}(k_1)e_{h_1}^2e_{h_3}^2 \end{aligned} \tag{4.5}$$

where k_1 is the parallel wavevector of light going forward and k_2 is the one going backward, $e_{h_2}(k) = e^{iq_zh_2}$ represents the propagation term inside the dielectric layer, and $e_{h_j} = e^{ik_{k_{z_j}}h_j}$ the one for the metallic layers. The direct transmission of light in the structure is represented by

$$t_k^d = \tau^{12}\tau_k^{23}\tau_k^{34}\tau^{45}e_{h_1}e_{h_2}(k)e_{h_3} \tag{4.6}$$

with k wavevector inside the dielectric layer. The total transmission coefficient is given by

$$t = \sum_k t_k^d(1 + A_{14}) \tag{4.7}$$

where A_{14} represents the considered summation of every possible combination of loops of the system. This is achieved using the following matrix form :

$$A_{14} = \mathbf{V_k^{in}} \times [\mathbf{I} - \mathbf{T_k}]^{-1} \times \mathbf{V_k^{out}} \tag{4.8}$$

where $\mathbf{V_k^{in}}$ is a vector representing the initial loop of a certain combination, $\mathbf{I}$ is the identity matrix, $\mathbf{T_k}$ is a matrix of a subsequent loop with the corresponding connecting coefficient, and $\mathbf{V_k^{out}}$ represents the exit coefficient of the final loop considered. The middle term in Eq. (11) is a geometric series of matrices that sums up all possible combination of paths, in the same way a simple geometric series sums up all paths of a single layer. These vectors and matrices take the form

$$\begin{aligned} \mathbf{V_k^{in}} &= \begin{bmatrix} a^{12}f^{12}a_{k_1,k_2}^{23}f_{k_1,k_2}^{23} & \dots & a_{k_1,k_2}^{14}f_{k_1,k_2}^{14t} \end{bmatrix} \\ \mathbf{T_k} &= \begin{bmatrix} a^{12-12}f^{12} & a_{k_1,k_2}^{12-23}f_{k_1,k_2}^{23} & \dots & a_{k_1,k_2}^{12-14}f_{k_1,k_2}^{14t} \\ a^{23-12}f^{12} & a_{k_1,k_2}^{23-23}f_{k_1,k_2}^{23} & \dots & a_{k_1,k_2}^{23-14}f_{k_1,k_2}^{14t} \\ \vdots & \vdots & \ddots & \vdots \\ a^{14-12}f^{12} & a_{k_1,k_2}^{14-23}f_{k_1,k_2}^{23} & \dots & a_{k_1,k_2}^{14-14}f_{k_1,k_2}^{14t} \end{bmatrix} \\ \mathbf{V_\alpha^{out}} &= \begin{bmatrix} t_{k_2}^{12} & t_{k_2}^{23} & \dots & t_{k_2}^{14} \end{bmatrix}^T \end{aligned} \tag{4.9}$$

where a_{k_1,k_2}^{xy-ab} represents a connecting coefficient that uses the previous wavevector k_1 as the incoming wavevector for the reflection coefficient of the next loop. The exit coefficient $t_{k_2}^{23}$ inputs the correct transmission coefficient for the considered path, using the wavevector of the last loop. It is to be noted that the vectors and matrices of Eqs. (12) and (13) use the loop factors f_{13t}, f_{24t}, and f_{14t} , which consider the loop with a summation of the previous possible loop that can exist inside. Finer details are provided in the Supplementary Information section. The total transmission of the system is given by $T = |t|^2$. A Matlab code for the implementation of the model is available in the Supplementary Information section.

4.5 Results

4.5.1 Transmission in the subwavelength regime with a thick dielectric layer

In Fig. 4.4, the transmission spectra of a nanostructured MIM is presented for the case of PEC and dielectric constant $\epsilon_1 = \epsilon_2 = \epsilon_3 = 1$. The dimensions, relative to the period of the system d, are $h_1 = h_3 = 2d$, $h_2 = 1.6d$, $a = 0.25d$. The curves obtained for the transmission spectrum of this structure with a finite element simulation via the COMSOL software is superposed and shows perfect agreement. The time of calculation is 10^2 faster with the model for a similar resolution on the number of wavelength steps. This improvement in calculation time rises to 10^3 when only the zero diffraction order is considered inside the dielectric layer (which is valid in the subwavelength regime for thick dielectric layers). In the case of a two-dimensional structure calculation, this improvement factor would rise to another 10-fold. The transmission is characterized by a series of resonant peaks spaced apart in multiples of the length of the different cavities of the structure. As no radiative losses from the surface roughness of the layer as well as no absorption losses from the metal are included in the model, full transmission (T=1) is reached for resonant wavelengths. In the lower panel, the phase term associated with the wave propagation of loop f_{12} and f_{13t} is represented. This phase term is obtained by using $\phi = atan(Im(f)/Re(f))$. It includes both the phase shift from the optical propagation and the phase shift resulting from the reflection on the interface, and for f_{12} this is given by $\phi = \phi_1 + \phi_2$, where $\phi_1 = q_{z\alpha}h_1$ and $\phi_2 = atan(Im(\rho)/Re(\rho))$. The loop $f_{13t} = \frac{f_{13}}{(1-f_{12})(1-f_{23})}$ represents the loop of the combination of layers 1 and 2, with the geometric summation of the inner loops f_{12} and f_{23} included. The resonances of the system occurs when $Real(e^{i2\phi}) = 1$ for both loops. This condition for loop f_{12} means that modes from the metallic layer individually can emerge as a resonant state of the system. The other resonances occur for a combination of both the metallic layer and the dielectric layer (loop f_{13t}). No resonance from the dielectric layer only is observed, which is consistent with the fact that light needs to travel through the metallic layer first, which only allows resonant

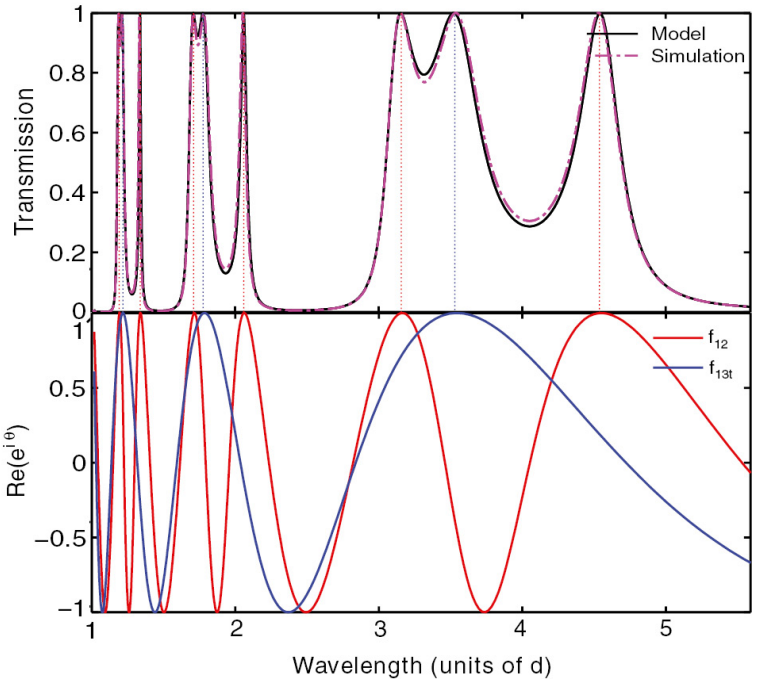


Figure 4.4 Transmission of the MIM periodic structure for dimensions $a = 0.25d$, $h_1 = h_3 = 1.6d$, and $h_2 = 2d$.

modes to go through.

In Fig. 4.5, the dispersion curves of the structure are represented, with the $Real(e^{i2(\phi_1+\phi_2)}) = 1$ condition represented by the black dashed line for the f_{12} modes and gray dashed lines for the f_{13t} modes. For a small incident wavevector, the resonances associated with the metallic layer behave like Fabry-Perot cavity modes with no dependence over the tangential wavevector component kx (Bravo-Abad et al., 2004b) as the propagation vector for this loop is given by the TEM mode of the slits $q_z = kw$. The modes of f_{13t} behave as dielectric core and metallic cladding waveguide modes, but phase shifted as it includes a propagation inside the metallic slit as well as the propagation inside the dielectric bounded by metallic layers. A remarkable bending of all curves occurs close to the "folding" of the light line, which is a well-known feature of periodic corrugation inside a metallic film (Pendry et al., 2004). This bending is connected to the coupling to modes of the corrugated surface and is represented through the admittance of the modes reaching high values close to the Wood anomaly condition $k_z = 0$ (Pendry et al., 2004). The resonant state can thus be described as having either a cavity-like character (ϕ_1) or a surface mode character (ϕ_2) (Garcia-Vidal et al., 2010; Marquier et al., 2005), depending on which phase factor is contributing more to the resonance.

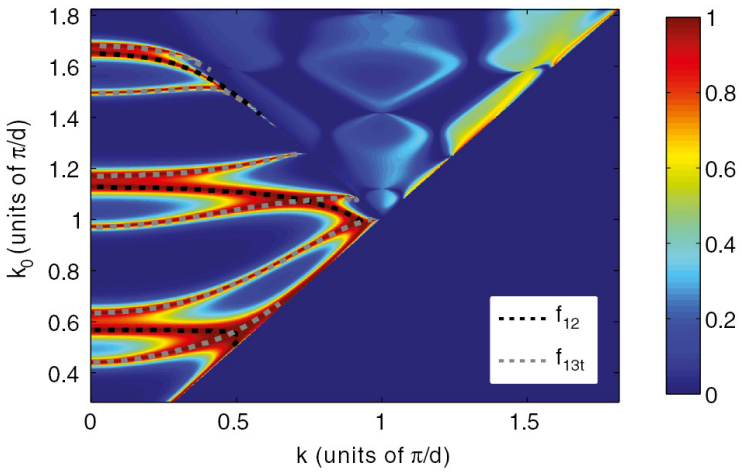


Figure 4.5 Dispersion curves of the MIM structure with dimensions $h_1 = h_3 = 1.6d$, $a = 0.25d$, and $h_2 = 2d$. The dashed black line represents the resonance condition for the f_{12} loop and the gray dashed line for the f_{13t} loop.

4.5.2 Transmission in the subwavelength regime with a thin dielectric layer

In the subwavelength regime considered throughout this paper, the diffraction orders inside the dielectric are evanescent. They will only contribute significantly to the total transmission when the dielectric layer is decreased to a size where the exponential decay is small. The resonances in this case emerge from the summation of the contribution of every diffraction order. Such a situation is represented in the dispersion graph of Fig. 4.6. The curves in panel A show resonances relative to a MIM structure with dimensions $h_1 = h_3 = 1.6d$, $a = 0.2d$, $h_2 = 0.5d$. An important property to observe from this graph is the discontinuities in the resonant behavior of the system, reminiscent of bandgaps in the dispersion relation of planar MIM structure (Dionne et al., 2005). The transmission coefficient for the direct transmission term with (B) $k = k_0$ and (C) $k = k_0 - k_r$ wavevectors are plotted in the subpanel (the transmission factor for the $+1$ diffraction order is negligible). These graphs show the transmission coefficient reaching values close to 1 and -1 near the same region, which indicate resonant states that are out of phase with one another, leading to no field being transmitted through the total structure. This direct transmission factor includes the interaction term of the field localized at both surfaces, which influences their respective propagation, as in a planar MIM structure.

In conclusion, a MIM structure presents resonant behavior that resembles a combination of the modes of a corrugated metallic film with the Fabry-Perot modes of a dielectric layer. These modes can in fact be described using the phase condition of unity for a loop containing both layers, as well as modes of the loop of the metallic layer only. When the evanescent

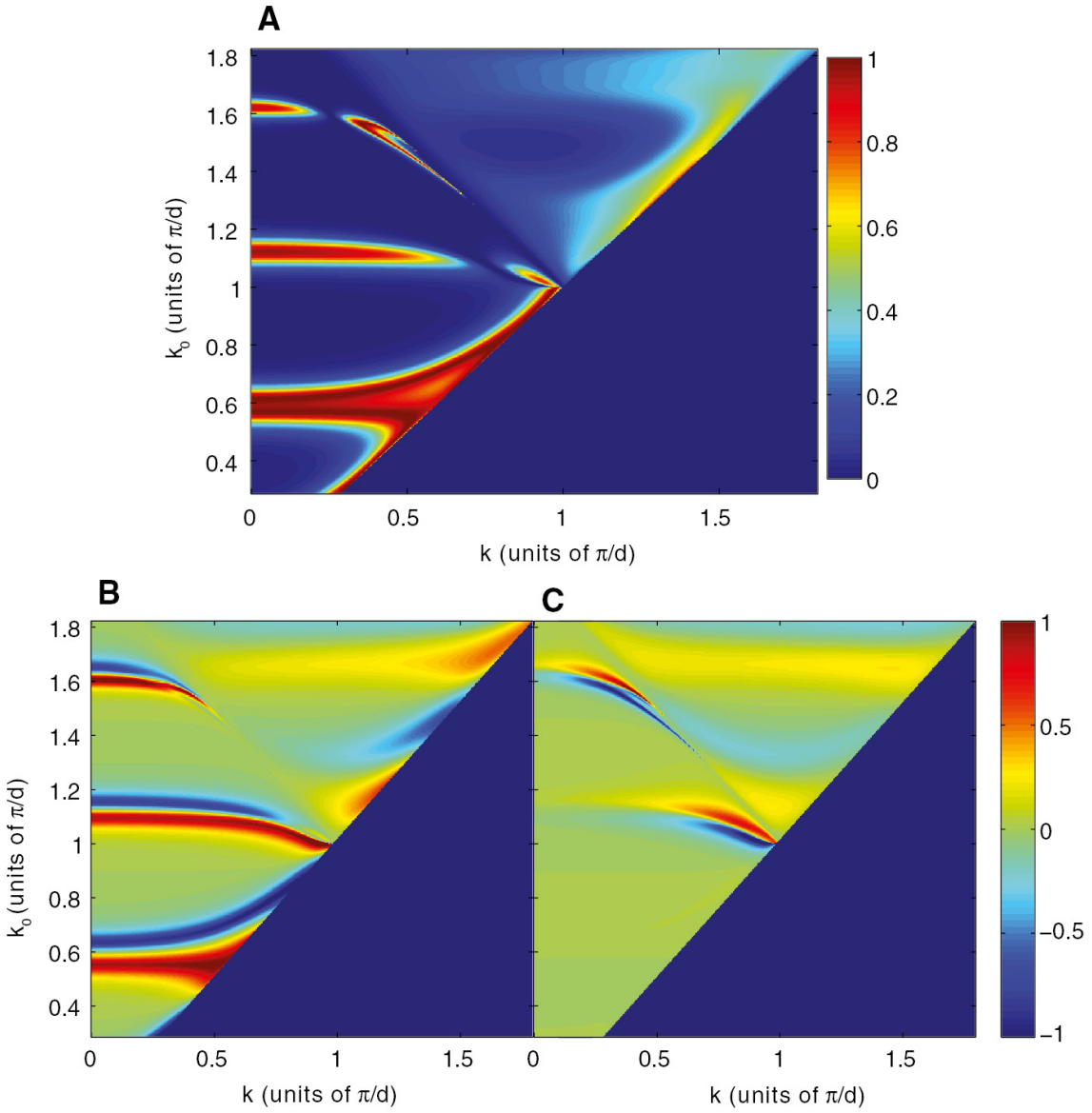


Figure 4.6 (A) Dispersion relation for MIM structure with $h_1 = h_3 = 1.6d$, $a = 0.25d$, and $h2 = 0.5d$. Discontinuities in the dispersion curves can be found for the upper branches. Subpanel : transmission coefficient with diffraction order (B) 0 and (C) –1 considered for the direct transmission term t^d.

higher-order diffraction modes inside the dielectric become considerable, the surface fields on both surfaces influence the resonance behavior of the system, as in a MIM structure. Destructive interference from these fields creates discontinuity in the dispersion curves where no transmission is observed.

CHAPITRE 5 ARTICLE 3 : ELECTRON BEAM LITHOGRAPHY USING A PMMA/P(MMA 8.5 MAA) BILAYER FOR NEGATIVE TONE LIFT-OFF PROCESS

Cet article publié dans *Journal of Vacuum Science and Technology* présente une nouvelle recette de nano-fabrication pour une méthode de lift-off. Il s'agit d'une bicouche de PMMA et de son co-polymère, le P(MMA 8.5 MAA). Lorsque surexposées, ces résines deviennent de contraste négatif. De plus, puisque la sensibilité de la PMMA est légèrement supérieure, un profil de "undercut" est toujours obtenu en une seule étape d'exposition et de développement. Cette méthode a permis d'obtenir des résolutions intéressantes pour les structures d'intérêt et à servi à produire les structures pour la section 7.

5.1 Auteurs

André-Pierre Blanchard-Dionne et Michel Meunier

5.2 Introduction

Electron beam lithography has become one of the most widespread nanofabrication tool for both industrial and academic research purposes (Vieu et al., 2000; Broers et al., 1996). The short wavelength of electrons and the availability of great focusing equipment allows for one of the best resolution available, combined with a great flexibility in writing (Manfrinato et al., 2013; Duan et al., 2010a). It is a technique of great interest to study the properties of devices at the nanoscale level and to develop applications such as data storage (Baek et al., 2005), nanoelectromechanical systems (Craighead, 2000; Maier et al., 2001), plasmonic devices (Okamoto et al., 2004; Barbillon et al., 2007), or semiconductor technology components (Borgström et al., 2007). Because this technique consists in a lithographic process, further steps are required in order to obtain the desired final structures. The patterned resist serves as a mask for etching or as a mask for deposition in a lift-off process. The availability of different resist materials and procedures becomes crucial in order to efficiently achieve any desired structure. In this paper, we present a lift-off process using a bilayer of poly methylmethacrylate (PMMA) and copolymer P(MMA 8.5 MAA) as negative tone resists. While these commonly available resists are normally used as a high resolution positive-tone resist, overexposing them induces crosslinking of the polymer molecules, leaving only the exposed regions unetched by organic solvants(Zailer et al., 1996; Hoole et al., 1997; Duan et al., 2010b; Teh

et al., 2003). It has been demonstrated that PMMA can achieve a similar resolution in the negative and the positive tones (Hoole et al., 1997; Duan et al., 2010b). Furthermore, using the bilayer, an undercut profile is achieved after development, which is crucial for obtaining a proper removal of the patterned resist and metallic layer on top during the lift-off step. The undercut profiles are highly important in the case of liftoff of isolated features, for which the removal of the material cannot start from the edges and propagate toward the structure. This method represents an additional high resolution process for the negative tone lift-off that compares in resolution to other reported methods that usually use hydrogen silsesquioxane (HSQ) as the top layer such as HSQ/PMMA(Yang et al., 2008b), HSQ/HPR (Piciu et al., 2007), and HSQ/novolak bilayers (van Delft et al., 2000). It is an easy to implement recipe suitable for thick metallic deposition and gives great wall verticality, which is of great interest whenever the deposited material is part of the final structure.

5.3 Experiment

The procedure to achieve the lift-off process is schematically presented in Fig. 5.1. A first layer of P(MMA 8.5 MAA) copolymer (9% in ethyl lactate) was spin-coated on a glass substrate covered with a 100 nm indium tin oxide layer (Sigma-Aldrich) using a Brewer Science 200cbx spin coater and was oven baked at 140 C for 30 min in order to evaporate any excess solvent in the resist. A second layer of PMMA 950 (2% in anisole) was then spun on top of that layer and soft-baked at 170 C for 30 min. For the results presented here, the thickness was usually set to 340 nm for the copolymer layer and 75 nm for the PMMA, but different thicknesses could be used depending on the thickness and the resolution desired for the final structure. The bilayer was then patterned using electron beam lithography (Raith eLine Plus system at an acceleration voltage of 20 kV and a beam current of 230 pA. The development of the resist was achieved by gently manually agitating the sample in acetone for about 240 s. The sample was then placed in a high vacuum chamber inside an Edwards electron beam evaporator where a 100 nm gold layer was deposited on top of the pattern. The electron beam was accelerated at a tension of 7.5 kV at an emission current of 280 mA toward a gold filled crucible to heat the sample at a sufficient temperature for evaporation. Dry etching of the underlying resist was achieved by an O2 plasma at 500 W at a pressure of 200 mTorr for 15 min using a PVA Tepla GIGAbatch 310 plasma asher. The sample was then rinsed in acetone in an ultrasonic bath for about 5 min to remove any undesirable etching residues.

Crosslinking behavior of 495 and 950 k PMMA resists as well as the P(MMA 8.5 MAA) copolymer resist was characterized by performing the atomic force microscopy (AFM) measurements of exposed patterns for each resists taken separately. Silicon was used as a substrate

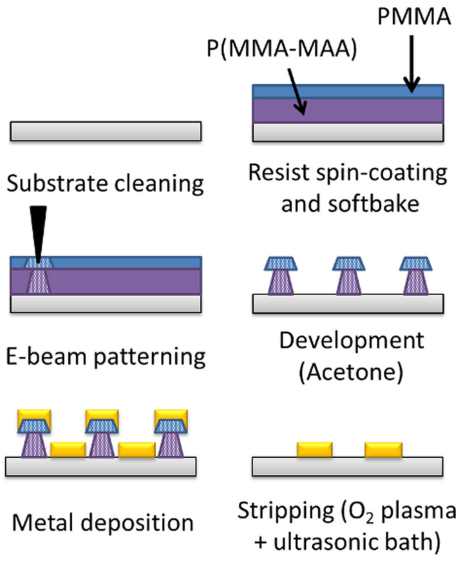


Figure 5.1 Process flow of the lift-off procedure based on the negative tone PMMA/P(MMA 8.5 MAA) resist bilayer.

for those characterization measurements. The layers were soft-baked and then < patterned using a voltage of 20 kV and a current of 230 pA, for different doses. The patterns for the characterization were made of circles of 200 nm diameter separated by a 600 nm period. The width and thickness of the developed patterns for the different resists are presented in Fig. 5.2.

The cross-linking sensitivity for all three resists can be retrieved from Fig.5.2(a) which plots the thickness of the features as a function of exposure dose. The exposure gave significant structures starting at a dose of 80 mC/cm2 for both PMMA resists and at 65 mC/cm2 for the copolymer, identified as the gel dose of the resist (Feller, 2008) . It then reached a plateau at doses of 100 or 120 mC/cm2 , respectively, which corresponds to full cross-linking of the polymer molecules. No significant differences were observed for the two PMMA resists of different molecular weight (495 and 950 K). According to Greeneich's equation (Dobisz et al., 2000) which describes the average molecular weight of polymer molecules upon exposure, with a relatively small exposure, most of the PMMA molecules in both resists should be cleaved into smaller fragments of similar low molecular weight. This dose corresponds to the positive tone resist sensitivity and represents 1%–10% of the total dose used for crosslinking. The crosslinking events thus begin with the same state of the polymer molecules, and so, the initial molecular weight of the material has a little effect on the final size. A significant difference was observed for the P(MMA 8.5 MAA) copolymer, probably due to the different nature of the material. As can be observed from the data in Fig. 5.2(b), the cross-linked

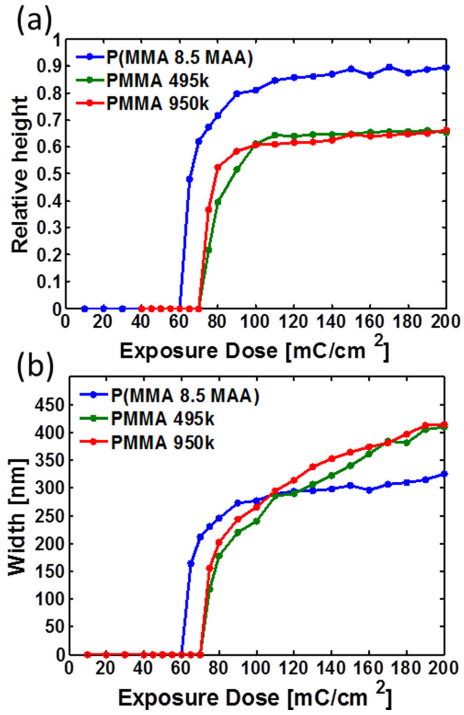


Figure 5.2 (a) Relative height and (b) width of the patterned features as a function of exposure dose with silicon as the substrate. The implemented width of the features was 200 nm.

state of the molecule starts at a lower dosage, but the width of the features remains always smaller than the PMMA resist for high enough doses, making it an ideal undercut layer for the bilayer system. This difference in size can be attributed to the significantly different chain lengths of the cross-linked polymer molecules(MicroChem, 2001) as well as the different three-dimensional organization of the polymer (Ku and Scala, 1969) after cross-linking.

The diameters of the developed structures are wider than what is implemented in the e-beam lithography software for doses that corresponds to a narrower diameter of the underlying copolymer resist. A small adjustment thus needs to be made to obtain correct dimensions of the features, which depends on many factors such as the beam current, the acceleration voltage, and the nature of the substrate. We also observe in Fig. 2(a) that the polymer is reduced to about 60% of its initial thickness for the PMMA resists after exposure and development when fully cross-linked. The degree of swelling for the cross-link molecules is less compared to the linear molecule (MicroChem, 2001), and this reduction in thickness can thus be associated with solvent evaporation in the material (Teh et al., 2003). This reduction was 90% for the copolymer case, which involved a different solvent (ethyl lactate) as well as a different density of cross-links. It is to be noted that different development times were tested and had no effect on the final size of the features, as long as it was sufficiently long to assure

that the unexposed regions were fully etched.

5.4 Results and discussion

In order to demonstrate the advantage of the bilayer, scanning electron microscope images of the structures were taken after the deposition of gold and after stripping of the resist. The larger PMMA layer on top of the P(MMA 8.5 MAA) layer creates an undercut profile that will allow the etching molecules to reach the underlying resist during the lift-off [Figs. 4(a), 4(c) and 4(e)]. Negative photoresist exhibit strong positive slopes [see Figs. 3 and 4(e)] upon exposure due to forward electron scattering which renders any stripping of the deposited material difficult since material can be deposited on the sides of the features, forming a continuous layer. In the case of the bilayer, the material was easily lifted using O2 plasma dry etching. Note that residues of the liftoff are cleaned using ultrasonic agitation in acetone.

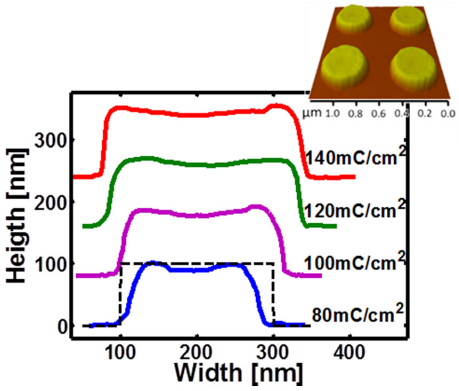


Figure 5.3 AFM measurements of the cross-section of the PMMA 495 resist on silicon for several doses (dashed line represents the implemented cross-section of the feature). Inset : 3D plot of the AFM measurement of the PMMA 495 k features on silicon.

Usage of the cross-linked material gives great advantages compared to other conventional electron beam resist. The cross-linked PMMA is a very robust and resistant material, making it a versatile material for MEMS fabrication either as a sacrificial layer or as a component of the MEMS itself.11,14 It can also reach high aspect ratio pillars (around six for the case considered here) without collapsing upon manipulation. A very good regularity of the individual patterns was found on patterned windows of 100 lm. As shown in Fig. 5.5, a lift-off process of 50 nm features was achieved using this material for a gold layer thickness of 100 nm, yielding an aspect ratio of 2 for the structured deposited material.

This technique thus represents an easy fabrication process in order to achieve great resolution with a high aspect ratio for the pattern transfer through lift-off. Although a larger exposure

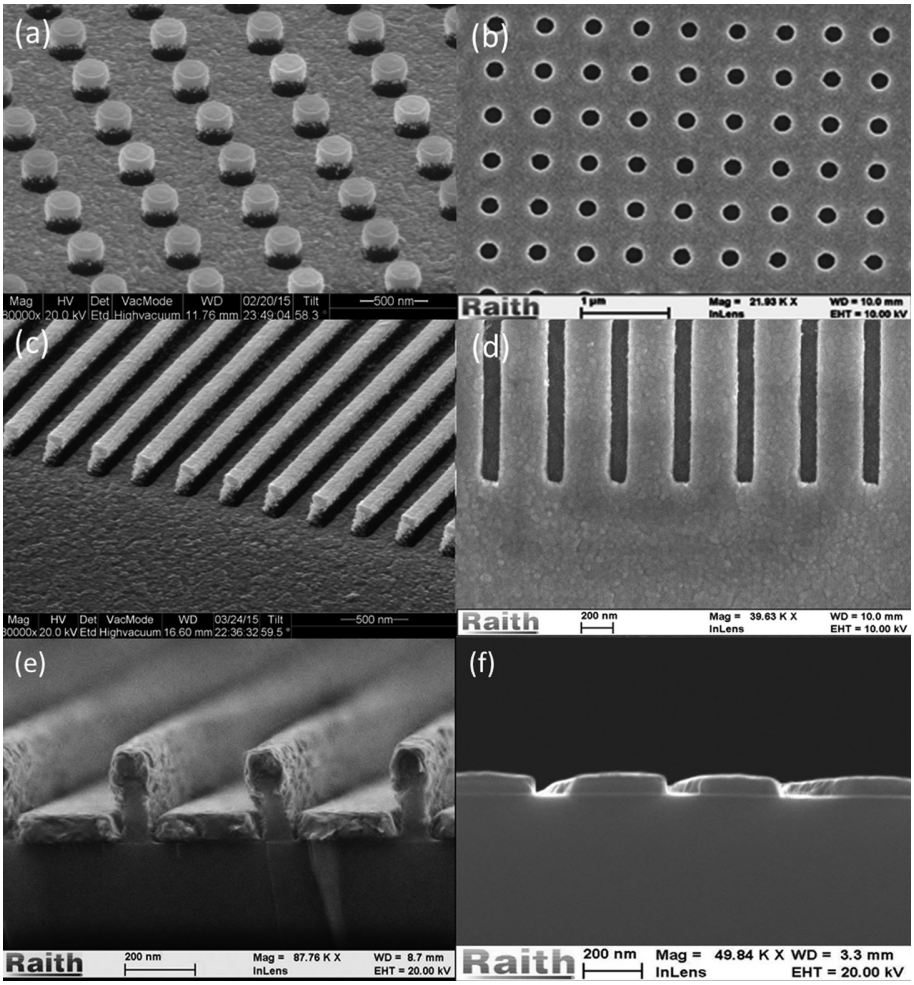


Figure 5.4 (a) Nanohole array and (c) nanoslits array after metal deposition showing an undercut profile. (b) and (d) Nanoholes and nanoslits after lift-off. (e) and (f) Cross-section of the nanoslits configuration before and after lift-off. The final slit structure is 100nm wide, 100 nm thick ; the slits are 400 nm apart.

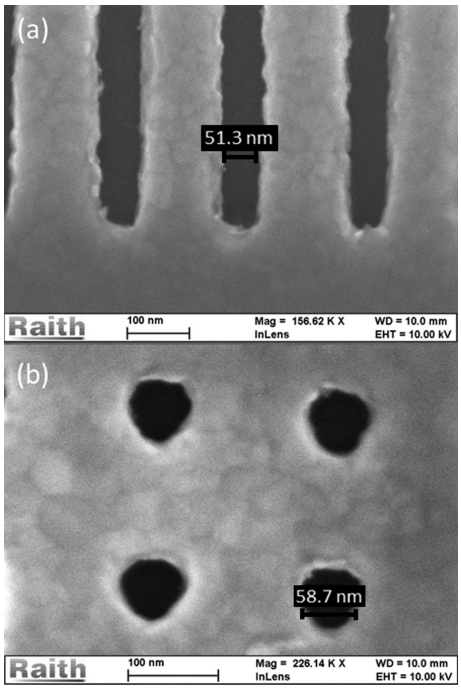


Figure 5.5 (a) Nanoslits of 51 nm and (b) nanoholes of 58 nm dimension both with a 200nm pitch and 100nm thickness of gold.

dose is required compared to other reported methods, notably one using a HSQ/PMMA bilayer (Rommel et al., 2013; Yang et al., 2008b) no optimization steps other than the exposure are required since the development is noncritical and the bottom layer naturally develops into a narrower structure. The resist used, PMMA, is a commonly available and low-cost electron beam resist. Stripping is made through O2 plasma, making the technique compatible with most substrates. The recipe implemented in this study was optimized for thicker deposited material (100 nm). While the resolution achieved of 50 nm is larger than other reported resolutions (Rommel et al., 2013) , it is comparable when the aspect ratio is taken into consideration. The presented method thus represents a viable alternative with similar fabrication capabilities than the other commonly used negativetone processes.

In Fig. 5.6, we show the transmission spectrum of a 475 nm period nanohole array of 190 nm diameter holes in a 100 nm thin gold film that exhibits extraordinary optical transmission (Ebbesen et al., 1998). These structures were obtained using a 340/75 nm bilayer of P(MMA-MAA)/PMMA bilayer at an exposure dose of 130 mC/cm2. The resonant peaks can be identified, which are related to coupling of light with surface waves of the highly conductive metal. A good agreement is found for the experimental results compared with the simulation of the ideal case using COMSOL finite-element method, which shows the quality of the fabrication process. A slight increase in the full width at the half maximum for the resonance

peaks is attributable to the surface aspect of the metallic structures, which was considered perfectly flat in the simulations.

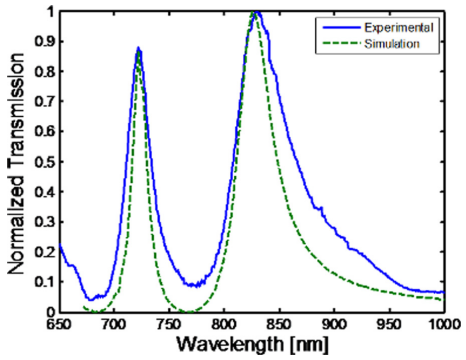


Figure 5.6 Experimental and simulated transmission spectrum of nanohole arrays of 475nm period, 190nm diameter and 100 nm thick gold layer with water as the medium.

5.5 Summary and Conclusion

The process suggested in this paper represents an easy to implement nanofabrication method of great resolution for thick lift-off of a negative tone resist. The bilayer of widely available PMMA/P(MMA 8.5 MAA) resists helps to achieve an undercut profile without any other steps than the development itself. A resolution of 50 nm was presented for closely stacked structures of 100 nm thicknesses. Other resolution and/or thickness of the deposited material could be achieved using different thicknesses of the resists. This method is of great interest for many applications involving nanoscale features, as was demonstrated for the extraordinary transmission of nanohole arrays.

5.6 Acknowledgement

The authors acknowledge the financial contribution from the National Science and Engineering Research Council of Canada (NSERC), as well as the technical help from Yves Drolet, Christophe Clément, and Marie-Hélène Bernier from the Microfabrication Lab (LMF) of Polytechnique Montreal.

CHAPITRE 6 ARTICLE 4 : INTENSITY BASED SURFACE PLASMON RESONANCE SENSOR USING A NANOHOLE RECTANGULAR ARRAY

Cet article publié dans *Optics Express* demontre une méthode expérimentale pour effectuer de la biodétection à l'aide de structures de nanotrous. Il avance une méthode pour améliorer les performances de ce type de capteur, en exploitant sa nature bi-dimensionnelle. En effet, le signal de chacune des polarisations -X et -Y est utilisé comme signal autoréférencé ce qui amplifie la sensibilité et réduit le bruit.

6.1 Auteurs

André-Pierre Blanchard-Dionne, Laurent Guyot, Sergiy Patskovsky, Reuven Gordon, Michel Meunier

6.2 Abstract

We show high resolution measurements of a surface plasmon resonance (SPR) sensor based on a rectangular nanohole array in a metal film. This SPR setup uses balanced intensity detection between two orthogonal polarizations of a He Ne laser beam, which allows for sensitivity improvement, noise reduction and rejection of any uncorrelated variation in the intensity signal. A bulk sensitivity resolution of 6.4×10^{-6} RIU is demonstrated. The proposed methodology is promising for applications in portable nanoplasmonic multisensing and imaging.

6.3 Introduction

The extraordinary transmission of light through nanostructured arrays of subwavelength holes (Ebbesen et al., 1998) in thin gold films and its relation to surface plasmon resonance (SPR) (Ghaemi et al., 1998) has recently inspired researchers to use these devices for label-free biosensing (Brolo et al., 2004). The diffraction properties of the periodic structure allows for light momentum enhancement, thus allowing excitation of surface plasmon polaritons. Such excitation of surface waves increases the amount of light scattered inside the holes, giving rise to precise peaks in the transmission spectrum at the resonance wavelength. Since the conditions of plasmon excitation are extremely sensitive to the refractive index (RI), the shift of the resonance wavelength is used for real-time detection and studies of biological binding

events. The surface plasmon's propagation constant can be retrieved by solving Maxwell's equation at the interface of a metal and a dielectric, which yields bounded modes for TM polarization. In the approximation that the holes do not change the dispersion relation of the plasmon, and that there is no strong coupling between the two interfaces of the film, the wavelength that satisfies the condition of resonant excitation of these bounded modes for a diffraction array at normal incidence is given by (Ghaemi et al., 1998) :

$$\lambda = \left[\left(\frac{m}{a_x}\right) + \left(\frac{n}{a_y}\right)\right]^{-1/2} \sqrt{\frac{\epsilon_m n_a^2}{\epsilon_m + n_a^2}} \tag{6.1}$$

where m and n are integer diffraction orders of light on the grating, a_x and a_y are the periodicities of the array in the x and y axes, and n_a and ϵ_m are the refractive index and the dielectric constant of the surrounding medium and of the metal, respectively.

Such plasmonic systems based on nanostructured hole arrays are known to provide new properties and advantages over the conventional Kretschmann SPR sensor configuration : the collinear setup allows for easy integration, hence giving great miniaturization possibilities and permitting incorporation into a microfluidic cell with high-throughput and multiplexed sensing (Sinton et al., 2008; Ji et al., 2008; Eftekhari et al., 2009; Yanik et al., 2010). The applications of modern nanofabrication technologies allow for low-cost and large-scale fabrication of regular plasmonic metallic nanostructures on different dielectric or semiconductor substrates (Kwak et al., 2005; Skinner et al., 2008).

Despite a number of advantages, nanohole arrays show sensitivity and resolution orders of magnitude lower compared to conventional SPR devices (Brolo et al., 2004; Yanik et al., 2010; Hwang et al., 2008; Yang et al., 2009; Lee et al., 2009; Lesuffleur et al., 2008). So far, resolution of 6.6×10^{-5} RI units (RIU) has been demonstrated (Hwang et al., 2008). In general, it has been suggested that grating coupler-based surface plasmon sensor exhibit lower sensitivities than prism-coupler ones (Homola et al., 1999), and devices based on extraordinary transmission are usually affected by a low signal-to-noise ratio since the transmitted intensity is usually of about 5% (Ghaemi et al., 1998). In this article, we improve the resolution of the nanohole array configuration by using polarization modulation, a biperiodic array and balanced detection. This configuration retains the collinear geometry that is favoured for integration into a portable SPR device, and also uses only a single laser source and intensity detection.

6.4 Basic Idea and Approach

The performance of portable nanoplasmonic sensing and imaging systems depend on the complexity and cost of the excitation/detection system. An intensity interrogation approach with one or several fixed wavelength sources is well suited for such applications because it can provide an efficient and simple system, using a low-cost and stable monochromatic laser diode sources in combination with 2D CCD camera detector. However, the resolution of such reported intensity systems is low, typically $10^{-4}RIU$ (Yang et al., 2009). Intensity based sensors must also be corrected for any changes in intensity that are not correlated with the displacement of the resonance peak, such as changes in light absorption through the addition of tested analytes, or source intensity noise. To reduce such spurious intensity changes, differential systems with a reference or calibration channel can be realized by introducing structure with identical sensing characteristics (Yang et al., 2009; Lee et al., 2009). Here, we exploit polarization diversity within a biperiodic nanohole array to achieve self-referencing and thereby reduce the spurious contributions to the noise.

We report a resolution-enhanced nanohole array sensor based on the intensity measurements of a single wavelength source. In this setup, we use the transmission signal of two orthogonal polarizations impinging on a rectangular nanohole array (inset of Fig. 1), as was introduced previously (Eftekhari et al., 2008). The periods in x and y of the array are chosen in order to have one peak below the source's wavelength, and one above, as shown in Fig. 1. A modification of the refractive index close to the metal surface thus gives rise to an increase in transmission for one polarization and a decrease for the other one, and the difference between the two corresponds to the detection signal. This method allows up to double the sensitivity of the sensor since it uses the variation of two slopes instead of only one. Furthermore, with a careful choice of the position of the peaks and of the working wavelength the initial calibration point can be set to zero amplitude, allowing for better contrast in the detection signal and better noise reduction by having similar amplitude on the two polarizations.

6.5 Fabrication, design and optimization of the nanohole rectangular array

The two-dimensional nature of nanohole array offers the possibility of having distinct transmission features for orthogonal polarizations. These resonant properties are dependent on the many parameters of the array, such as the periodicity, the size of the holes and the thickness of the metal layer. Optimization of the sensing performances relies on the proper choice of these parameters for operation at 632.8 nm wavelength and in an aqueous environment.

Figure 2(a) shows an example of a nanohole array with periods $380nm \times 420nm$. The gold

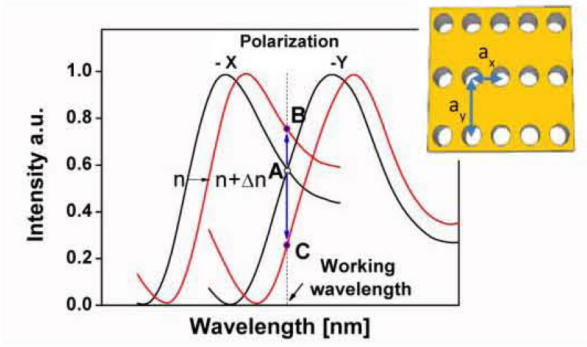


Figure 6.1 Principle of the proposed technique using a nanohole rectangular array with different periodicities ax and ay along the two main axes. The transmission spectrum of such a structure is shown with resonant peaks at different wavelength for the two orthogonal polarizations. The point of intersection (Point A) corresponds to the initial calibration point. The change in refractive index (red curves) shows an increase of intensity for one polarization (point B) and a decrease for the other polarization (point C).

layer samples were obtained from Platypus Technologies and nanostructured by Focused Ion Beam (FIB) milling with a FEI DB-234, using a 30 kV acceleration voltage and 30 pA ion current. The thickness of the film was 100 nm and was chosen to be a few times the skin depth of gold in order to be optically opaque while reducing the exponential decrease of the guided modes inside the holes. The diameter of the holes is chosen to be of 200 nm in order to be before the cut-off frequency of any guided modes in the holes (Laux et al., 2009). This allows optimization of the transmitted intensity while reducing spurious noise from, for example, the intensity fluctuations of the source or absorption of the laser in the analyte. The choice of the periodicity determines the position of the resonant peaks. Structures can easily and precisely be tuned in order to meet the requirements of a specific application. In the case of the proposed sensor, the wavelength of a He-Ne source was chosen since highly stable laser sources and high performance optical equipment are widely available. The periods of the array were chosen with the help of Eq. (1) in order to have one peak below $632.8nm$ and one above. It has to be noted that the transmission peak wavelength, when measured experimentally, is red-shifted in comparison to what is calculated. The simple dispersion relation is therefore incomplete to fully take into account the phenomenon of extraordinary transmission. Interference between the resonant state (the surface plasmon) and a continuum of state (light scattered into the hole) gives rise to a red-shifted asymmetric peak typical of a Fano-type resonance (Genet et al., 2003). Also, the holes themselves can give rise to resonances (Koerkamp et al., 2004) which will affect the position of the transmission maxima. Therefore, when a precise position of the transmission peak is critical, a slight correction in

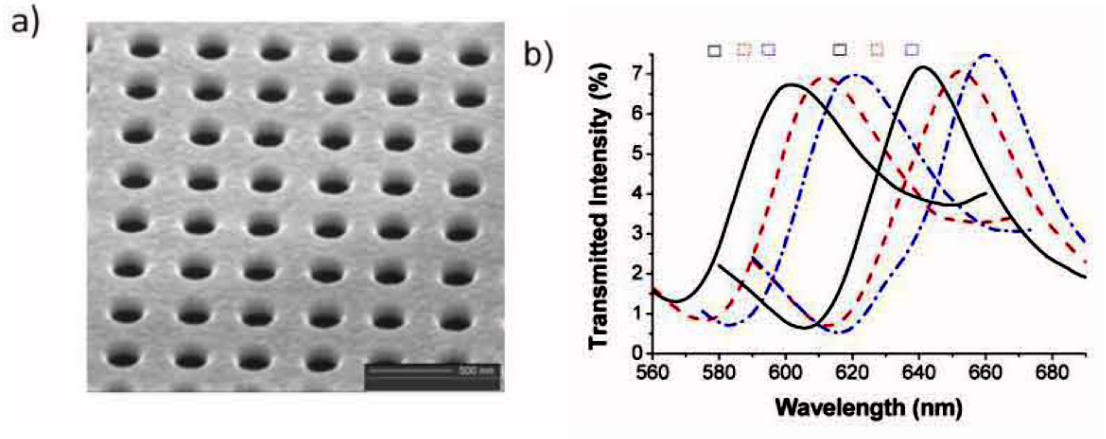


Figure 6.2 (a) Scanning electron microscopy image of an example of a nanohole rectangular array 380 nm x 420 nm (b) Transmission spectra of nanohole rectangular arrays with period 380 x 415nm (solid line), 390 x 425 nm (dashed line) and 395 x 435 nm (dotted-dashed line). The positions of the peaks are red-shifted of (from left to right 28 nm, 27 nm, 29 nm, 28 nm, 29 nm, 26 nm in comparison to the dispersion relation (square dots).

the period must be taken into account when fabricating the nanohole array. In Fig. 2(b), the transmission spectra of several nanohole rectangular arrays are presented, as well as the wavelength of resonance calculated with Eq. (1).

Since the position of the curves translates to longer wavelengths with an increase in refractive index, the dynamic range of the sensor will correspond to the range between the working wavelength and the position where the slopes vanish. Therefore, having the maxima of the right peak as close as possible to the right of the source's wavelength will increase the dynamic range of the sensor. Making the curves intersect at the source's wavelength can still be managed by adjusting the optical setup in order to suppress or increase the intensity of a particular polarization (see the instrumental methodology section below). The choice of period was made at 380×420 nm to increase dynamic range while having the steepest parts of the curves at the source's wavelength.

6.6 Instrumental Methodology

To test the nanoplasmonic structures in liquid, the experimental set-up illustrated in Fig. 4 was developed. A stabilized He-Ne laser was used as the source. Spatially filtered and polarized light passes through a Photo-Elastic Modulator (Hinds Instruments) and a quarter-wave plate in order to periodically modulate the state of polarization of light from linear to circular at a frequency of 50 kHz. Fine rotation of the second polarizer also serves for initial

equalization of the two orthogonal polarizations intensities to perfectly match the intersection point at the source's wavelength. Indeed, changing the orientation of this polarizer modulates the transmitted intensities by factors :

$$\cos(\theta)^2 + \cos(\theta)\sin(\theta) \tag{6.2}$$

for polarization along the x axis,

$$\sin(\theta)^2 + \cos(\theta)\sin(\theta) \tag{6.3}$$

for polarization along the y axis, where θ is the orientation of the polarizer. The changes in intensities for both polarizations are illustrated in Fig. 4(b). After transmission through

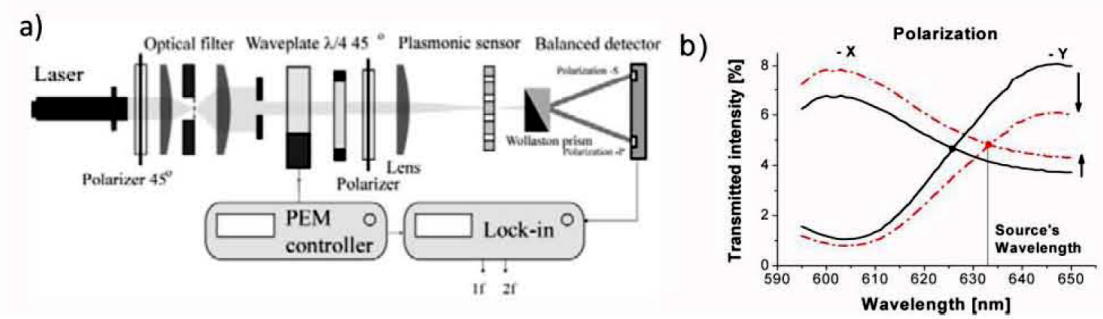


Figure 6.3 (a) Schematics of the optical setup used for the sensing experiment. (b) Adjustment of the initial calibration point by rotating the second polarizer from 45° to 35°. The intensities for both polarizations intersect at the source's wavelength.

the nanohole array, the beam is split in its two polarization components using a Wollaston prism towards a balanced photodetector (Nirvana Detector, New Focus), that together with a lock-in amplifier (Stanford Research System) allows for significant noise rejection at all the frequencies that differ from the modulation frequency. An open and flow-injection measurement cell was used for tests in liquid.

6.7 Results and Discussion

The wavelength sensitivity of the nanohole array was evaluated from the shift of the maxima when the solution was changed from water to pure ethanol, as shown in Fig. 5(a) . Shifts of 9.9 nm were recorded for the y polarization and for the x polarization, which corresponds to an estimated sensitivity of $396 nm RIU^{-1}$, when considering the difference of 0.025 RIU between the two solutions (Dorsey, 1940; Arce and Soto, 2005). The sensitivity in terms of change in

intensity was calculated by multiplying the slopes of the peaks by the wavelength sensitivity. The slopes at the source's wavelength were of $4.3\%nm^{-1}$ for the polarization along the y axis and $3.0\%nm^{-1}$ along the x axis (the slope on the red side of the resonant peak is lower, as can be expected from the shape of the Fano resonance peak), which corresponds to an intensity sensitivity of $1700\%RIU^{-1}$ and $1200\%RIU^{-1}$ respectively, for a total of $2900\%RIU^{-1}$ for the balanced detection. The sensitivity of this setup corresponds to an almost two-fold improvement compared to the sensitivity of a square array in similar conditions, since it corresponds to the addition of the displacement of two transmission peaks instead of only one. The intensity difference between the two polarizations was recorded as a function of time

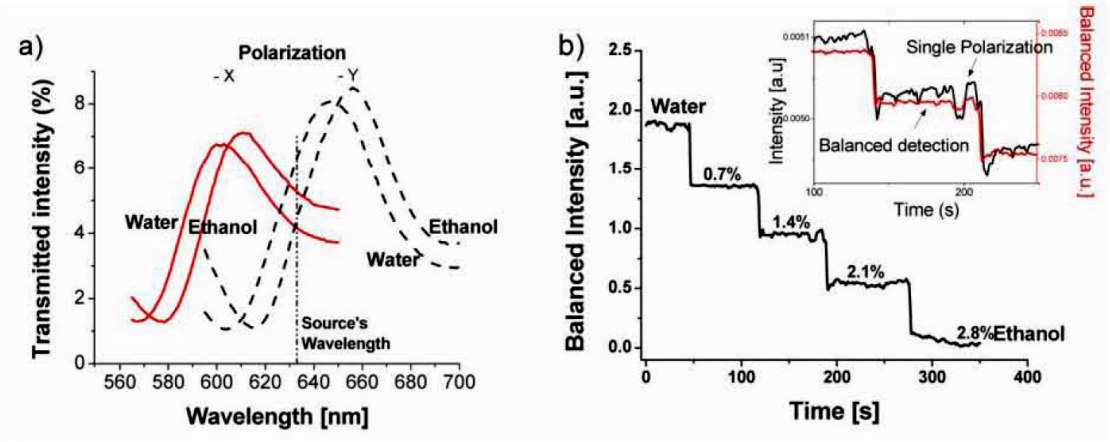


Figure 6.4 (a) Transmission spectra of the nanohole array with 380 x 420 nm as periods in water and ethanol. (b) Responses of the sensing system for small increase of ethanol. Insert : Noise levels from the signal of the balanced detection and from the signal of a single polarization.

with different concentrations of ethanol successively added to water in order to measure the maximum resolution of the system (Fig. 5(b)). Every step represents an addition of a small amount of ethanol, in order to obtain a 0.7% concentration difference, which corresponds to 1.7×10^{-4} RIU change. The signal to noise ratio (SNR) achieved is 27.4, allowing for a detection sensitivity of 6.4×10^{-6} RIU. The SNR was determined by taking the difference between the mean value of the signal for the bottom and top part of each step, divided by the standard deviation of the signal at those levels.

In order to demonstrate the improvement accomplished by the balanced detection of the rectangular array, the signal coming from one polarization only was compared to the signal from the balanced detection, as shown in the inset of Fig. 5(b). The single polarization signal in this case corresponds to the signal that is obtained from a single periodicity, which would be analog to the signal obtained from a square array on the presented setup. The SNR

obtained from the single polarization is 5 times lower than the one obtained from the balanced detection, clearly demonstrating the advantage of such detection method. The dynamic range was calculated by using a 10% sensitivity decreasing as range limits, which corresponds to a spectral shift of 20 nm or to a change in refractive index of 0.05 RIU.

The proposed experimental setup benefits from several features in comparison to the previous intensity based nanohole sensing systems [11–13]. First, two slopes are used instead of only one, allowing for a greater change in intensity to be measured (approximately double) from a modification of refractive index. Also, the problem of uncorrelated (i.e., spurious) intensity fluctuations is solved by the use of the two polarization components and balanced detection, which rejects the common fluctuations of the signal. Noise originating from the light source is reduced this way. Overall, the polarization modulation, bi-periodic array and balanced detection allow for an overall sensing system with significantly improved SNR. Despite the sensitivity being low in comparison to conventional angular-based SPR devices [14], the very low noise of this setup allows for similar sensing performance.

6.8 Conclusion

We demonstrated the use of a rectangular nanohole array with polarization modulation and balance detection in order to increase the performance of a nanohole array intensity based biosensor. A resolution of 6.4×10^{-6} RIU is achieved, which is an improvement in comparison to previously reported nanohole array sensors [10]. Since this type of sensor has such a small footprint, many arrays can be integrated into a chip in order to realize a multiplexed sensor, using a simple laser diode as the source and a 2-D CCD camera. Balanced detection would require the splitting of the light emerging from each array (using a Wollaston prism) and using two areas on the camera. Together with microfluidic channels, this structure and detection scheme could contribute to the realization of a fully integrated and highly sensitive sensor which can find many applications in the area of detection of chemical and biological species, or for the study of biomolecular interaction.

6.9 Acknowledgements

The authors acknowledge the financial contribution from the Natural Science and Engineering Research Council of Canada and Canadian Institute for Photonics Innovations, and the NSERC Strategic Network for Bioplasmonic Systems (Biopsys).

CHAPITRE 7 ARTICLE 5 : MULTIPERIODIC NANOHOLE ARRAY FOR HIGH PRECISION MULTIPLEXED SENSING

Dans cet article soumis à *ACS Photonics*, une structure originale de nano-trous est présentée afin de concevoir un biocapteur optique. Il s'agit d'un réseau de colonnes de nano-trous ayant chacune une période différente, en ordre croissant. De cette façon, la condition de résonance est rencontrée pour une seule colonne (ou ensemble de colonne), et le profil de résonance est obtenu. Le maxima d'intensité est utilisé comme signal, tout comme avec un capteur SPR conventionnel. Ce montage permet d'exploiter la possibilité de multiplexage des échantillons de nano-trous, tout en conservant un montage monochromatique simple. La performance est également accrue puisque cette méthode permet de rejeter le bruit corrélé du système optique.

7.1 Auteurs

André-Pierre Blanchard-Dionne et Michel Meunier

7.2 Abstract

In this article we present a multiperiodic nanohole array structure for improved sensing. The structure consists in a series of rows of nanoholes each with a different period, in ascending order. A monochromatic source illuminates the structure and a resonance condition is met for the row with a momentum matching Bloch wave, which leads to extraordinary optical transmission. This way, the profile of the resonance peak is fully obtained, and the sensing signal can be retrieved using the spatial position of the transmission maxima. This setup requires a simple optical setup while achieving increased resolution and accuracy. A resolution of $8.4^{-6}RIU$ is achieve which is comparable to SPR system based on the Kretchmann configuration.

7.3 Introduction

Ever since nanohole arrays were shown to exhibit extraordinary optical transmission (Ebbesen et al., 1998) and were used for sensing (Brolo et al., 2004), there has been a considerable amount of research done in order to optimize their performances. Indeed, early demonstrations of sensing resolution were usually low ($1 \times 10^{-4} - 1 \times 10^{-5} RIU$)(Hwang et al., 2008;

Im et al., 2011; Escobedo et al., 2011; Lee et al., 2012; Jia et al., 2013) compared to SPR devices which typically range in the $1 \times 10^{-6} - 1 \times 10^{-7} RIU$. A number of authors have implemented different strategiesin order to improve the resolution of the device, such as crossed polarizers (Tetz et al., 2006), bragg mirrors on the edges of the holes (Lindquist et al., 2009), different shapes such as double-hole arrays (Lesuffleur et al., 2007) or elliptical holes (Tellez et al., 2013), dual periodic system (Blanchard-Dionne et al., 2011; Eitan et al., 2015) or dual wavelength systems (Escobedo et al., 2011; Chang et al., 2011) or using a different collimation angle (de Menezes et al., 2015). Even with all these method, most applications of nanohole arrays to sensing still rely on simplistic interrogation methods like wavelength interrogation via a spectrometer (Jia et al., 2013; Wittenberg et al., 2012; Soler et al., 2017; Li et al., 2017), or direct intensity measurements (Im et al., 2014).

If we consider typical SPR sensors based on the Kretchmann configuration, usually 3 types of interrogation (Piliarik and Homola, 2006) are possible. The first one, an intensity scan at a fixed angle measures the difference in intensity of the reflected light after a change in refractive index as the sensing signal. The wavelength scan and the angular scan use the position of a maxima or minima of the spectrum for sensing. As was pointed out by a theoretical analysis of the sensors' performances (Piliarik and Homola, 2009), these two last interrogation methods usually lead to improved performance since the signal isn't affected by correlated type noise. The angular scan is usually the method of choice since it allows for a simpler optical setup. For nanohole array typed sensors, the picture is quite different, since the resonance is achieved using a linear collimation optical system. Integration of the device into an imaging system is easily implemented, and with the small footprint of each nanohole array, high multiplexing can be achieved. Angular scans are thus never used, and the systems usually rely on an intensity or wavelength interrogation.

In this paper we present a 4th type of interrogation method which consists in a scan of the hole array periodicity. Since the coupling mechanism of the incident light to surface waves relies on the diffraction of light by the array, changing the period will lead to a change of the diffracted light wavevector. Obtaining the spatial intensity profile of the transmitted light for a structure with incremental increases of the period thus results in a wavevector scan, just like an incremental change of the wavelength of light or of the incident angle would. The optical setup used for this sensing device remains a very simple monochromatic microscope with high acquisition frequency and retains the capacity for high multiplexing.

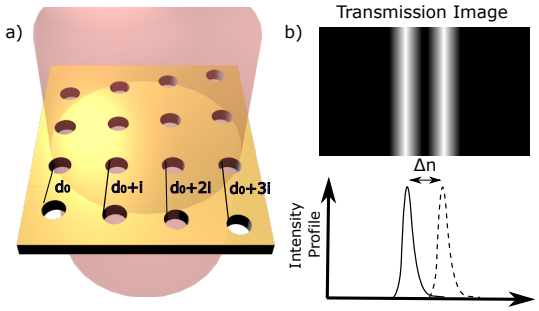


Figure 7.1 a) Multiperiodic nanohole array. Each column has a periodicity equal to $d_0 + ni$, where d_0 is the initial period, n is the number of the column and i is the increment. b) The transmission image of the structure will exhibit a bright fringe for column with periods that match the resonant condition of the array. Changing the refractive index will move the fringe and the position of the maxima is the sensing signal.

7.4 Approach and Experimental Setup

The structure we use consists in circular hole arrays with period varying from 500-600 nm with an increment of 1 nm. The spacing in the other dimension was fixed at 700 nm. The hole array were fabricated using E-beam Lithography (Raith E-Line Plus) in a lift-off process (Blanchard-Dionne and Meunier, 2015). A gold layer of 100 nm was deposited using a E-beam evaporator with a 2nm Chrome adhesion layer. A PDMS microfluidic chip with 3 channels was used to deliver the solutions to a 3x3 sensor array. The sensor assembly was fixed to a rotary stage in order to align the sample with the beam.

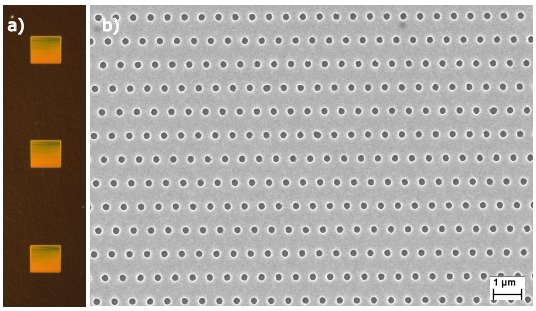


Figure 7.2 *Reflection* image of the multiperiodic nanohole array under white light illumination, using crossed polarizers. The sample reflects a different color which is dependent of the periodicity. c) Nanohole array with changing period (the total sample goes from 500-600nm) in the x axis and a 700 nm period in th y axis. The hole size is 180 nm and the thickness of the gold film is 100 nm.

The optical setup consists in a laser diode source (Thorlabs) at 785nm on a diode controller (Newport), which goes into a spatial filter (Newport), towards the nanohole array sensors.

Light is collected via a microscope using a 25x microscope objective (Nikon) and a camera (Q-imaging). The signal was analysed in a Labview interface. A detection window was set around the transmission maxima of the sample and the intensity was recorded as a function of the spatial position in the X axis, using a summation in the Y axis. The signal was recorded as a function of time and the position of the maxima was determined using the centroid method. It should be noted that the resolution of the system depends on the magnification, which in counter parts limits the multiplexing capabilities of the device.

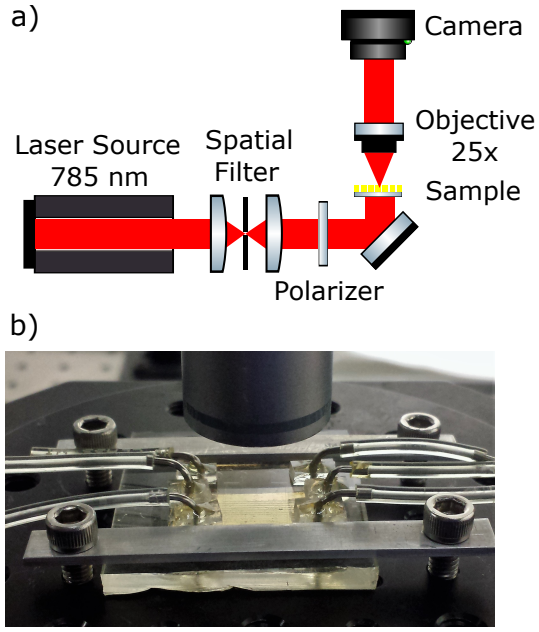


Figure 7.3 The optical setup consists in a home made microscope with a monochromatic laser diode source, a spatial filter and polarizer. The microscope objective was 25x. b) The PDMS microfluidic chip with 3 parallel channels.

7.5 Results and discussion

In order to test the performance of the device, a sensitivity measurements as well as a real-time resolution evalutation were performed. The sensitivity was measured by taking 2 images of the multiperiodic array with solutions of different refractive index, water (1.3296(Hale and Querry, 1973)) and ethanol (1.3577(Rheims et al., 1997)). The difference in the position of the maxima was determined to be 38 pixels on the camera. Since the extent of the 70 μm sample on the camera was 300 pixels and that every line was distant of 0.7 μm and represented a shift of 1 nm of periodicity one from another, we can conclude that the sample's sensitivity was $S = 1352 px/RIU = 450.7 nm/RIU$.

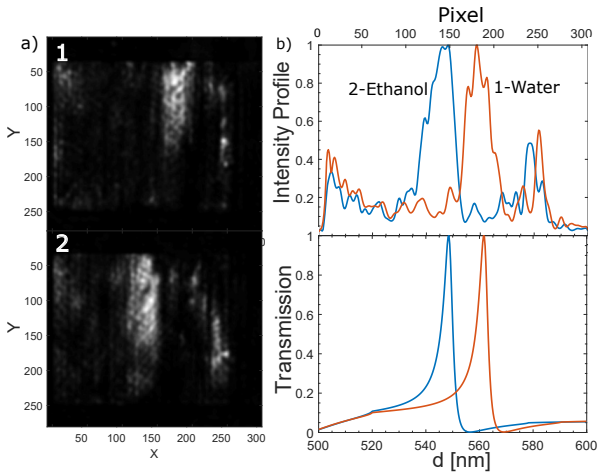


Figure 7.4 Transmission image of the multiperiodic nanohole array sample with 1) water and 2) ethanol as the surrounding medium. b) *top* Measured transmission profile of the images of the arrays. The intensity was integrated along the y-axis and plotted as a function of the x-axis. *bottom* Transmission intensity of the nanohole array as a function of the period as calculated using coupled mode theory.

Coupled Mode Theory (Garcia-Vidal et al., 2010; Blanchard-Dionne and Meunier, 2017) was used in order to model the optical properties of the arrays as a function of the array period. The transmission spectra are given in Fig 7.4b), with a theoritical sensitivity of $462.6nm/RIU$, which is very similar to the one measured. The resolution of the system was measured by alterning solution from water to a small concentration of ethanol (2%). The position of the maxima was recorded as a function of time using the centroid method. The resolution corresponds to the minimal increment of refractive index that would be detectable by the system, which we represent using $R = \frac{\Delta n}{SNR}$ where SNR is the signal to noise ratio. For a change of refractive index of $6 \times 10^{-4} RIU$ the SNR recorded was 71.2 for a resolution of $8.4 \times 10^{-6} RIU$.

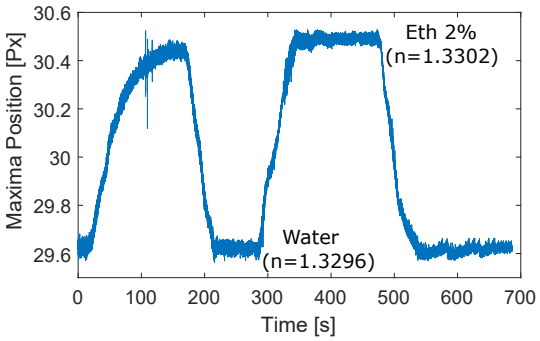


Figure 7.5

This setup accounts for several advantages compared to multiplexed devices using a simple intensity measurement. First, since the signal relies on the position of a maxima, the monitoring of a change in refractive index will be directly accountable for by a change in the resonant property of the system. This is important when we consider that the signal is obtained via transmission, which can be altered by the composition of the sensing medium itself, and is susceptible to any contaminants in the solution. The resulting sensor isn't only improved in performance by reducing spurious noise and correlated noise but also in accuracy. It also improves the multiplexing capabilities of the sensor since systems that rely on a spectrometer either slow down greatly the acquisition rate for each sensor, or can only use 1-D images since the other dimension is used for the grating of the spectrometer.

CHAPITRE 8 DISCUSSION GÉNÉRALE

8.1 Discussion sur la méthode de modélisation employée

La méthode des modes couplés a permis de relever la dépendance en indice de réfraction de la résonance, qui se distingue d'une résonance due à des SPPs. Je crois que la réalisation du fait que, pour un PEC, la dérivée par rapport à l'indice de réfraction résulte simplement en $S = \lambda_r/n$ où λ_r est la longueur d'onde de résonance et n l'indice de réfraction témoigne de la sensibilité de la partie "géométrique" de la résonance, qui ne présente pas de dispersion, et qui varie de la même façon qu'un résonateur optique simple. La considération de la constante diélectrique du métal produit quelques effets. Elle introduit des pertes dues à la propagation de l'onde de surface mais également dues à la propagation du mode guidé à l'intérieur de l'indentation. Elle décale la résonance vers le rouge (plus grande longueur d'onde) puisque la constante de propagation du mode guidé à l'intérieur de l'indentation est diminuée due à la pénétration de l'onde à l'intérieur des parois du métal. D'ailleurs pour des ouvertures étroites, les modes TM sont affectés par l'interaction du champ de surface d'une paroi à l'autre, véhiculé par les plasmons de surface (verticaux). Bien que ceci a de multiples effets sur la position spectrale de la résonance, sa dépendance reste proportionnelle approximativement à $S = \lambda_r/n$ car le caractère dispersif du métal affecte négligemment la dispersion de la résonance. Ceci va en accord avec le fait rapportée que, lorsque la distance entre les trous est faible, la résonance provient de l'interaction de l'ensemble des ondes diffractées à la surface des trous et ressemble en caractère à un mode géométrique.

Je crois que la modélisation a également pu clairement établir la différence notable entre les types de structures 1-D de nano-fentes et 2-D de nano-trous. Cette différence est due au caractère différent de l'onde de propagation à l'intérieur du trou, qui est toujours propagative pour une nano-fente et évanescente pour un nano-trou (lorsque $a < \lambda/2$, ce qui est généralement le cas). Les nano-fentes 1-D possèdent un caractère de cavitation de la résonance, comme pour un Fabry-Pérot. La plus grande concentration du champ à l'intérieur du trou est une des raisons pour lesquelles il est avantageux d'utiliser les nano-trous par rapport aux nano-fentes puisque les changement d'indice de réfraction se trouve à la surface.

Le calcul de la localisation du champ électromagnétique pour les résonances a permis d'éclairer l'efficacité de la détection selon la taille de l'analyte. Elle a également permis de réaliser que, contrairement à une résonance classique de SPR en configuration Kretchmann, le champs n'est pas uniquement concentré à la surface du métal et à l'intérieur de celui-ci mais également dans le substrat et à l'intérieur du trou, qui sont des régions qui ne sont pas atteignables

pour les molécules à détecter. La sensibilité effective ainsi que la résolution des structures nano-plasmoniques ne peuvent donc théoriquement et expérimentalement jamais atteindre les mêmes performances que la SPR, mais peuvent quand même atteindre une portion significative, jusqu'à 60% pour les réseaux de nano-trous.

8.2 Discussion sur les méthodes de fabrication employées

La première publication (chapitre 6) sur les nano-trous utilisait le FIB pour fabriquer les échantillons. Cette méthode permet d'obtenir rapidement et avec une bonne qualité des échantillons fonctionnels, mais requiert beaucoup de temps. Il est donc clair qu'un groupe de recherche qui veut s'investir dans ce type d'échantillon devrait avoir recours à des méthodes de fabrication alternatives. Les autres méthodes nécessitent un plus grand développement des étapes de fabrication, mais une fois les recettes déterminées, la fabrication peut devenir beaucoup plus rapide.

La publication sur la fabrication qui fait l'objet du chapitre 5 et qui a été la méthode employée pour les échantillons du chapitre 7 s'est avérée être une méthode fiable. Elle permet d'employer la grande qualité de la lithographie par faisceau d'électrons ainsi que sa grande précision. Elle permettait également d'obtenir un "undercut" à chaque échantillon en une seule étape d'exposition et de développement. Cette méthode employait cependant la PMMA comme résine négative, ce qui nécessite une surexposition qui nécessite plus de temps d'utilisation du faisceau d'électrons, parfois jusqu'à 10 à 50 fois. Puisque les échantillons de nano-trous ne nécessitent pas vraiment de grandes surfaces à exposer, cette limitation ne s'est pas avérée critique, mais il est clair que pour une plus grande utilisation, il serait mieux d'employer d'autres méthodes. Je tiens à mentionner la référence (Yang et al., 2008b) pour une méthode avec la HSQ, qui nécessite une étape de plus pour le développement de la résine sacrificielle, mais qui est une méthode plus rapide qui est grandement citée.

En somme, je crois qu'un des meilleurs compromis pour la fabrication d'échantillon du type de nano-trous est le transfert par pelage de motif. Cette méthode permet d'avoir la plus grande qualité d'échantillon puisqu'elle emploie la méthode la plus précise de fabrication, la lithographie par faisceau d'électron. Elle présente également l'avantage d'employer une méthodologie simple puisque les échantillons sont fabriqués sur un substrat de silicium, qui est un substrat conducteur et dont les taux de gravure sont grandement documentés. Elle représente une méthode à grande échelle puisqu'une fois le moule initial fabriqué, une grande quantité de reproductions peuvent être effectuées, moyennant quelques étapes seulement. Finalement, cette méthode possède le grand avantage de fabriquer les échantillons avec la plus faible rugosité de surface possible, puisque la surface active est celle qui faisait face au

silicium. Les rugosités de surface rapportées par les publications en faisant mention indiquent une amélioration d'un facteur 10, avec une rugosité atteignant les 0.1 nm (RMS).

8.3 Discussion sur la conception des biocapteurs

Le premier système proposé (6) faisant usage du signal des deux polarisations était une approche intéressante et performante, mais qui était démontrée dans la publication que pour un seul échantillon à la fois. L'intégration dans un système d'imagerie afin d'effectuer une détection pour plusieurs capteurs de manière simultanée s'est avérée être plus difficile. Deux approches ont été explorées, soit dans un premier temps en utilisant un polariseur tournant, et dans un deuxième temps en utilisant l'image des deux polarisations de manière juxtaposée grâce à un prisme de Wollaston. La première méthode était très bruitée due à la présence d'une perturbation mécanique du moteur tournant, et n'a pas été concluante. La deuxième méthode, bien qu'elle apporta quelques essais concluants, ne permettait pas de faciliter la détection d'un grand nombre d'échantillons à la fois puisque les deux images étaient inévitablement éloignées l'une de l'autre. L'utilisation de deux caméras apportait un problème de synchronisme dans l'analyse et ne figurait pas dans la conception d'un montage optique simple.

La deuxième idée retenue s'est d'ailleurs révélée être plus performante (7). En utilisant une approche qui permettait d'obtenir la position spatiale de la résonance pour chacun des échantillons, un capteur plus précis et plus fiable était obtenu. Je crois que pour réaliser un capteur de qualité, il est primordial d'avoir recours à la position d'un maxima, ce qui n'est possible autrement que pour les capteurs utilisant des interrogations en longueur d'onde. Comme mentionné dans la publication, cela limite la fréquence d'acquisition de ces capteurs, et donc leurs performances.

La limite au niveau du système proposé repose sur la précision du système d'imagerie quant à la position spatiale de la résonance. En effectuant un très grand grossissement de l'image, l'intensité lumineuse peut être rapportée sur un plus grand nombre de pixels et une bien meilleure détection peut être obtenue. Mais cela limite l'intérêt même du système, qui est d'imager un très grand nombre de capteurs à la fois. Un compromis dois être trouvé selon l'application souhaitée, et, dans le cas de la démonstration expérimentale de la publication, le grossissement a été restreint afin de pouvoir effectuer la détection d'au moins une centaine d'autres échantillons sur la caméra. La méthode du centroïde a d'ailleurs été choisie afin d'accélérer le traitement du signal comparée à une régression polynomiale tel que retrouvé souvent sur les capteurs SPR, qui serait lourde pour un grand nombre de capteurs.

CHAPITRE 9 CONCLUSION ET RECOMMANDATIONS

En conclusion, je crois qu'il a été démontré que les réseaux de nano-trous possèdent un potentiel intéressant dans le domaine d'application des biocapteurs. Les performances de ces capteurs sont suffisantes, leurs avantages au niveau du multiplexage est évident, et leur intégration en tant qu'outil de diagnostic complet a été démontrée. Des protocoles de fonctionnalisation sont de plus en plus développés afin de réaliser des tests tangibles de détection d'éléments pathogènes ou de marqueurs biologiques de toutes sortes, tels les marqueurs d'accidents cardiaques (Jia et al., 2013), de cancer des ovaires (Im et al., 2014), cancer du sein (Monteiro et al., 2016), de la sclérose en plaque (Wittenberg et al., 2012), de MTS tel la chlamidya et la gonorrhée (Soler et al., 2017), ou l'activité de sécrétion cellulaire (Li et al., 2017). Ces tests ont été spécifiquement développés pour profiter du mutiplexage des réseaux de nano-trous. On pourrait également penser à une intégration de plusieurs tests développés pour les capteurs SPR (Homola, 2008).

Les biocapteurs de type SPR trouvent généralement leur domaine d'application en tant qu'outil pour les biochimistes pour étudier les affinités entre un ligand et son récepteur. En effet, la très grande précision des biocapteurs, additionnée à leur capacité à effectuer une détection en temps réel, permet de déterminer avec précision les constantes de liaisons des molécules étudiées. Lorsque ces capteurs sont employés comme simple outil de diagnostic pour un test binaire de la présence d'un analyte, ils perdent leurs avantages au profit de technologies plus simple comme des tests ELISA. Cependant, de récentes applications ont noté de clairs avantages des biocapteurs basés sur les nano-trous face à la technologie d'ELISA, étant plus rapides, plus sensibles et nécessitant un moins grand volume d'échantillon (Im et al., 2014; Li et al., 2017). Les techniques d'ELISA peuvent également nécessiter beaucoup d'étapes d'attachement de tags, ce qui la technique fastidieuse. Il est donc envisageable de retrouver la technologie de biocapteurs basés sur les nano-trous pour certaines applications niches qui nécessitent une plus grande résolution.

Je crois que pour que cette technologie se développe davantage, elle devra tirer avantage de ses particularités qui la distinguent des autres types de biocapteurs. Par exemple, il pourrait être utile d'exploiter la réponse en temps réel du capteur et la connaissance des constantes d'affinité entre molécule et récepteur pour isoler davantage la réponse du seul analyte ciblé. Cela permettrait d'isoler le signal à détecter et de rejeter le signal non-spécifique. La particularité de pouvoir faire une détection en temps réel a d'ailleurs déjà démontré ses intérêts dans le cadre d'une étude des sécrétions cellulaires (Li et al., 2017). De plus, la possibilité d'utiliser

le signal de centaines de capteurs simultanément pourrait ouvrir à une analyse combinée de la réponse de la solution à plusieurs combinaisons de récepteurs et ainsi retrouver une réponse spécifique à la combinaison proposée pour éliminer la contribution non-spécifique.

9.1 Synthèse des travaux

Dans le cadre de ce doctorat, une étude à la fois au niveau expérimental et théorique a été réalisé afin de peser complètement le potentiel des structures basées sur les réseaux de nano-trous à des fins de biodétection. La modélisation des propriétés optiques de ces capteurs à l'aide de la méthode des modes couplés a permis une analyse en profondeur de leur potentiel au niveau des performances de biodétection. De plus, cette analyse a permis de cerner les valeurs des paramètres de périodicité, de taille des trous ainsi que d'épaisseur des films utilisés afin d'optimiser la résolution du capteur. Cette modélisation a également permis de faire la lumière sur les mécanismes physiques de résonance, et a donc permis de comprendre davantage le phénomène en jeu. Cela peut être utile pour les autres sphères d'application des biocapteurs. Ce travail théorique a permis la rédaction de deux articles scientifiques, un publié dans la revue "Nanophotonics" (Blanchard-Dionne and Meunier, 2017) et un autre soumis à la revue "Advances in Optics and Photonics" en juin 2017.

En deuxième partie de ce doctorat les techniques de fabrication ont été étudiées. Dans le cadre de ce doctorat, 2 méthodes de fabrication ont été employées. Une première, incluse dans la publication (Blanchard-Dionne et al., 2011), utilisait simplement le FIB. Un algorithme de correction du raccordement des fenêtres de gravure a été mise en place afin de permettre l'automatisation de la fabrication. Avec le venue du appareil de lithographie par faisceau d'électrons, une procédure a été mise en place qui a fait l'objet d'une autre publication dans la revue "Journal of Vacuum Science and Technology" uniquement sur ce sujet (Blanchard-Dionne and Meunier, 2015) puisqu'il s'agissait d'une nouvelle méthode mise en place pour la fabrication à partir de lift-off pour des résines négatives.

Finalement, une troisième partie présentait l'ensemble des travaux expérimentaux réalisés pour la conception d'un biocapteur multiplexé basé sur les réseaux périodiques de nano-trous. Ces deux publications mettaient de l'avant des méthodes pour optimiser la résolution des capteurs utilisant des schémas optiques diverses. Les premiers travaux employaient des périodicités différentes dans les axes x et y pour utiliser le signal différentiel de chacune des polarisations (Blanchard-Dionne et al., 2011) et ont été publiés dans "Optics Express". Une deuxième publication mettait de l'avant l'utilisation d'un réseau multipériodique pour la biodétection et a été soumise à "ACS Photonics" en aout 2017. Cette méthode possède l'avantage de baser le signal de détection sur un maxima de résonance et non pas un simple

signal d'intensité, tout en conservant la simplicité d'un montage optique monochromatique.

RÉFÉRENCES

A. Arce et A. Soto, “Physical and excess properties of binary and ternary mixtures of 1, 1-dimethylethoxy-butane, methanol, ethanol and water at 298.15 k”, *Thermochimica acta*, vol. 435, no. 2, pp. 197–201, 2005.

I.-B. Baek, J.-H. Yang, W.-J. Cho, C.-G. Ahn, K. Im, et S. Lee, “Electron beam lithography patterning of sub-10 nm line using hydrogen silsesquioxane for nanoscale device applications”, *Journal of Vacuum Science & Technology B : Microelectronics and Nanometer Structures Processing, Measurement, and Phenomena*, vol. 23, no. 6, pp. 3120–3123, 2005.

G. Barbillon, J.-L. Bijeon, J. Plain, M. L. De La Chapelle, P.-M. Adam, et P. Royer, “Electron beam lithography designed chemical nanosensors based on localized surface plasmon resonance”, *Surface Science*, vol. 601, no. 21, pp. 5057–5061, 2007.

A. Barik, L. M. Otto, D. Yoo, J. Jose, T. W. Johnson, et S.-H. Oh, “Dielectrophoresis-enhanced plasmonic sensing with gold nanohole arrays”, *Nano letters*, vol. 14, no. 4, pp. 2006–2012, 2014.

W. L. Barnes, A. Dereux, et T. W. Ebbesen, “Surface plasmon subwavelength optics”, *Nature*, vol. 424, no. 6950, pp. 824–830, 2003.

W. L. Barnes, W. A. Murray, J. Dintinger, E. Devaux, et T. Ebbesen, “Surface plasmon polaritons and their role in the enhanced transmission of light through periodic arrays of subwavelength holes in a metal film”, *Physical review letters*, vol. 92, no. 10, p. 107401, 2004.

H. Bethe, “Theory of diffraction by small holes”, *Physical Review*, vol. 66, no. 7-8, p. 163, 1944.

A.-P. Blanchard-Dionne, “NanoholeCal”, 6 2017. DOI : 10.6084/m9.figshare.5131519.v2. En ligne : https://figshare.com/articles/NanoholeCal_zip/5131519

——, “NanoholeCalStandalone”, 6 2017. DOI : 10.6084/m9.figshare.5131564.v2. En ligne : https://figshare.com/articles/NanoholeCal_Standalone/5131564

——, “MIM Periodic 1-D Slit Nanostructures - Couped Mode Theory”, 7 2017. DOI : 10.6084/m9.figshare.5131576.v1. En ligne : https://figshare.com/articles/MIM_Periodic_1-D_Slit_Nanostructures_-_Couped_Mode_Theory/5131576

A.-P. Blanchard-Dionne et M. Meunier, “Electron beam lithography using a pmma/p (mma 8.5 maa) bilayer for negative tone lift-off process”, *Journal of Vacuum Science & Technology B, Nanotechnology and Microelectronics : Materials, Processing, Measurement, and Phenomena*, vol. 33, no. 6, p. 061602, 2015.

——, “Optical transmission theory for metal-insulator-metal periodic nanostructures”, *Interface*, vol. 1, no. 2, p. 12, 2016.

——, “Optical transmission theory for metal-insulator-metal periodic nanostructures”, *Nanophotonics*, vol. 6, no. 1, pp. 349–355, 2017.

A. Blanchard-Dionne, L. Guyot, S. Patskovsky, R. Gordon, et M. Meunier, “Intensity based surface plasmon resonance sensor using a nanohole rectangular array”, *Optics express*, vol. 19, no. 16, pp. 15 041–15 046, 2011.

M. T. Borgström, G. Immink, B. Ketelaars, R. Algra, et E. P. Bakkers, “Synergetic nanowire growth”, *Nature nanotechnology*, vol. 2, no. 9, pp. 541–544, 2007.

J. Bravo-Abad, F. García-Vidal, et L. Martín-Moreno, “Resonant transmission of light through finite chains of subwavelength holes in a metallic film”, *Physical review letters*, vol. 93, no. 22, p. 227401, 2004.

J. Bravo-Abad, L. Martin-Moreno, et F. Garcia-Vidal, “Transmission properties of a single metallic slit : From the subwavelength regime to the geometrical-optics limit”, *Physical Review E*, vol. 69, no. 2, p. 026601, 2004.

A. Broers, A. Hoole, et J. Ryan, “Electron beam lithography—resolution limits”, *Microelectronic Engineering*, vol. 32, no. 1, pp. 131–142, 1996.

A. G. Brolo, R. Gordon, B. Leathem, et K. L. Kavanagh, “Surface plasmon sensor based on the enhanced light transmission through arrays of nanoholes in gold films”, *Langmuir*, vol. 20, no. 12, pp. 4813–4815, 2004.

Q. Cao et P. Lalanne, “Negative role of surface plasmons in the transmission of metallic gratings with very narrow slits”, *Physical Review Letters*, vol. 88, no. 5, p. 057403, 2002.

A. E. Cetin, A. F. Coskun, B. C. Galarreta, M. Huang, D. Herman, A. Ozcan, et H. Altug, "Handheld high-throughput plasmonic biosensor using computational on-chip imaging", *Light : Science & Applications*, vol. 3, no. 1, p. e122, 2014.

A. E. Cetin, D. Etezadi, B. C. Galarreta, M. P. Busson, Y. Eksioglu, et H. Altug, "Plasmonic nanohole arrays on a robust hybrid substrate for highly sensitive label-free biosensing", *ACS Photonics*, vol. 2, no. 8, pp. 1167–1174, 2015.

T.-Y. Chang, M. Huang, A. A. Yanik, H.-Y. Tsai, P. Shi, S. Aksu, M. F. Yanik, et H. Altug, "Large-scale plasmonic microarrays for label-free high-throughput screening", *Lab on a Chip*, vol. 11, no. 21, pp. 3596–3602, 2011.

H. Choo, M.-K. Kim, M. Staffaroni, T. J. Seok, J. Bokor, S. Cabrini, P. J. Schuck, M. C. Wu, et E. Yablonovitch, "Nanofocusing in a metal-insulator-metal gap plasmon waveguide with a three-dimensional linear taper", *Nature Photonics*, vol. 6, no. 12, pp. 838–844, 2012.

S. Collin, F. Pardo, et J.-L. Pelouard, "Waveguiding in nanoscale metallic apertures", *Optics Express*, vol. 15, no. 7, pp. 4310–4320, 2007.

A. F. Coskun, A. E. Cetin, B. C. Galarreta, D. A. Alvarez, H. Altug, et A. Ozcan, "Lensfree optofluidic plasmonic sensor for real-time and label-free monitoring of molecular binding events over a wide field-of-view", *Scientific reports*, vol. 4, p. 6789, 2014.

H. G. Craighead, "Nanoelectromechanical systems", *Science*, vol. 290, no. 5496, pp. 1532–1535, 2000.

D. Crouse et P. Keshavareddy, "Role of optical and surface plasmon modes in enhanced transmission and applications", *Optics express*, vol. 13, no. 20, pp. 7760–7771, 2005.

A. B. Dahlin, "Sensing applications based on plasmonic nanopores : The hole story", *Analyst*, vol. 140, no. 14, pp. 4748–4759, 2015.

F. G. De Abajo, "Colloquium : Light scattering by particle and hole arrays", *Reviews of Modern Physics*, vol. 79, no. 4, p. 1267, 2007.

F. G. De Abajo et J. Sáenz, "Electromagnetic surface modes in structured perfect-conductor surfaces", *Physical review letters*, vol. 95, no. 23, p. 233901, 2005.

F. G. De Abajo, R. Gómez-Medina, et J. Sáenz, "Full transmission through perfect-conductor subwavelength hole arrays", *Physical Review E*, vol. 72, no. 1, p. 016608, 2005.

A. De Leebeeck, L. S. Kumar, V. de Lange, D. Sinton, R. Gordon, et A. G. Brolo, "On-chip surface-based detection with nanohole arrays", *Analytical Chemistry*, vol. 79, no. 11, pp. 4094–4100, 2007.

F. de León-Pérez, G. Brucoli, F. García-Vidal, et L. Martín-Moreno, "Theory on the scattering of light and surface plasmon polaritons by arrays of holes and dimples in a metal film", *New Journal of Physics*, vol. 10, no. 10, p. 105017, 2008.

J. W. de Menezes, A. Thesing, C. Valsecchi, L. E. Armas, et A. G. Brolo, "Improving the performance of gold nanohole array biosensors by controlling the optical collimation conditions", *Applied optics*, vol. 54, no. 21, pp. 6502–6507, 2015.

J. Dionne, L. Sweatlock, H. Atwater, et A. Polman, "Planar metal plasmon waveguides : frequency-dependent dispersion, propagation, localization, and loss beyond the free electron model", *Physical Review B*, vol. 72, no. 7, p. 075405, 2005.

——, "Plasmon slot waveguides : Towards chip-scale propagation with subwavelength-scale localization", *Physical Review B*, vol. 73, no. 3, p. 035407, 2006.

E. A. Dobisz, S. L. Brandow, R. Bass, et J. Mitterender, "Effects of molecular properties on nanolithography in polymethyl methacrylate", *Journal of Vacuum Science & Technology B : Microelectronics and Nanometer Structures Processing, Measurement, and Phenomena*, vol. 18, no. 1, pp. 107–111, 2000.

N. E. Dorsey, *Properties of ordinary water-substance.* Reinhold Publishing Corporation. ; New York, 1940.

A. Drezet, C. Genet, et T. W. Ebbesen, "Miniature plasmonic wave plates", *Physical review letters*, vol. 101, no. 4, p. 043902, 2008.

H. Duan, V. R. Manfrinato, J. K. Yang, D. Winston, B. M. Cord, et K. K. Berggren, "Metrology for electron-beam lithography and resist contrast at the sub-10 nm scale", *Journal of Vacuum Science & Technology B, Nanotechnology and Microelectronics : Materials, Processing, Measurement, and Phenomena*, vol. 28, no. 6, pp. C6H11–C6H17, 2010.

H. Duan, D. Winston, J. K. Yang, B. M. Cord, V. R. Manfrinato, et K. K. Berggren, "Sub-10-nm half-pitch electron-beam lithography by using poly (methyl methacrylate) as a negative resist", *Journal of Vacuum Science & Technology B, Nanotechnology and Microelectronics : Materials, Processing, Measurement, and Phenomena*, vol. 28, no. 6, pp. C6C58–C6C62, 2010.

T. W. Ebbesen, H. J. Lezec, H. Ghaemi, T. Thio, et P. Wolff, “Extraordinary optical transmission through sub-wavelength hole arrays”, *Nature*, vol. 391, no. 6668, pp. 667–669, 1998.

E. Economou, “Surface plasmons in thin films”, *Physical review*, vol. 182, no. 2, p. 539, 1969.

F. Eftekhari, R. Gordon, J. Ferreira, A. Brolo, et D. Sinton, “Polarization-dependent sensing of a self-assembled monolayer using biaxial nanohole arrays”, *Applied Physics Letters*, vol. 92, no. 25, p. 253103, 2008.

F. Eftekhari, C. Escobedo, J. Ferreira, X. Duan, E. M. Girotto, A. G. Brolo, R. Gordon, et D. Sinton, “Nanoholes as nanochannels : flow-through plasmonic sensing”, *Analytical chemistry*, vol. 81, no. 11, pp. 4308–4311, 2009.

M. Eitan, Z. Iluz, Y. Yifat, A. Boag, Y. Hanein, et J. Scheuer, “Degeneracy breaking of wood’s anomaly for enhanced refractive index sensing”, *ACS Photonics*, vol. 2, no. 5, pp. 615–621, 2015.

C. Escobedo, S. Vincent, A. Choudhury, J. Campbell, A. Brolo, D. Sinton, et R. Gordon, “Integrated nanohole array surface plasmon resonance sensing device using a dual-wavelength source”, *Journal of Micromechanics and Microengineering*, vol. 21, no. 11, p. 115001, 2011.

C. Escobedo, “On-chip nanohole array based sensing : a review”, *Lab on a Chip*, vol. 13, no. 13, pp. 2445–2463, 2013.

C. Escobedo, A. G. Brolo, R. Gordon, et D. Sinton, “Flow-through vs flow-over : analysis of transport and binding in nanohole array plasmonic biosensors”, *Analytical chemistry*, vol. 82, no. 24, pp. 10 015–10 020, 2010.

U. Fano, “The theory of anomalous diffraction gratings and of quasi-stationary waves on metallic surfaces (sommerfeld’s waves)”, *JOSA*, vol. 31, no. 3, pp. 213–222, 1941.

R. L. Feller, “Thoughts about crosslinking”, *WAAC newsletter*, vol. 30, no. 3, pp. 16–20, 2008.

V. E. Ferry, L. A. Sweatlock, D. Pacifici, et H. A. Atwater, “Plasmonic nanostructure design for efficient light coupling into solar cells”, *Nano letters*, vol. 8, no. 12, pp. 4391–4397, 2008.

F. Garcia-Vidal et L. Martin-Moreno, “Transmission and focusing of light in one-dimensional periodically nanostructured metals”, *Physical Review B*, vol. 66, no. 15, p. 155412, 2002.

F. Garcia-Vidal, L. Martin-Moreno, et J. Pendry, "Surfaces with holes in them : new plasmonic metamaterials", *Journal of optics A : Pure and applied optics*, vol. 7, no. 2, p. S97, 2005.

F. J. Garcia-Vidal, L. Martin-Moreno, T. Ebbesen, et L. Kuipers, "Light passing through subwavelength apertures", *Reviews of Modern Physics*, vol. 82, no. 1, p. 729, 2010.

C. Genet et T. Ebbesen, "Light in tiny holes", *Nature*, vol. 445, no. 7123, pp. 39–46, 2007.

C. Genet, M. P. van Exter, et J. Woerdman, "Fano-type interpretation of red shifts and red tails in hole array transmission spectra", *Optics Communications*, vol. 225, no. 4, pp. 331–336, 2003.

H. Ghaemi, T. Thio, D. Grupp, T. W. Ebbesen, et H. Lezec, "Surface plasmons enhance optical transmission through subwavelength holes", *Physical review B*, vol. 58, no. 11, p. 6779, 1998.

R. Gordon et A. G. Brolo, "Increased cut-off wavelength for a subwavelength hole in a real metal", *Optics Express*, vol. 13, no. 6, pp. 1933–1938, 2005.

R. Gordon, D. Sinton, K. L. Kavanagh, et A. G. Brolo, "A new generation of sensors based on extraordinary optical transmission", *Accounts of chemical research*, vol. 41, no. 8, pp. 1049–1057, 2008.

D. K. Gramotnev et S. I. Bozhevolnyi, "Plasmonics beyond the diffraction limit", *Nature photonics*, vol. 4, no. 2, pp. 83–91, 2010.

L. Guyot, A. Blanchard-Dionne, S. Patskovsky, et M. Meunier, "Integrated silicon-based nanoplasmonic sensor", *Optics express*, vol. 19, no. 10, pp. 9962–9967, 2011.

G. M. Hale et M. R. Querry, "Optical constants of water in the 200-nm to 200-μm wavelength region", *Applied optics*, vol. 12, no. 3, pp. 555–563, 1973.

J. Henzie, M. H. Lee, et T. W. Odom, "Multiscale patterning of plasmonic metamaterials", *Nature nanotechnology*, vol. 2, no. 9, pp. 549–554, 2007.

M. T. Hill, M. Marell, E. S. Leong, B. Smalbrugge, Y. Zhu, M. Sun, P. J. Van Veldhoven, E. J. Geluk, F. Karouta, Y.-S. Oei *et al.*, "Lasing in metal-insulator-metal sub-wavelength plasmonic waveguides", *Optics express*, vol. 17, no. 13, pp. 11 107–11 112, 2009.

J. Homola, “Surface plasmon resonance sensors for detection of chemical and biological species”, *Chemical reviews*, vol. 108, no. 2, pp. 462–493, 2008.

J. Homola, I. Koudela, et S. S. Yee, “Surface plasmon resonance sensors based on diffraction gratings and prism couplers : sensitivity comparison”, *Sensors and Actuators B : Chemical*, vol. 54, no. 1, pp. 16–24, 1999.

A. Hoole, M. Welland, et A. Broers, “Negative pmma as a high-resolution resist-the limits and possibilities”, *Semiconductor science and technology*, vol. 12, no. 9, p. 1166, 1997.

M. Huang, B. C. Galarreta, A. E. Cetin, et H. Altug, “Actively transporting virus like analytes with optofluidics for rapid and ultrasensitive biodetection”, *Lab on a Chip*, vol. 13, no. 24, pp. 4841–4847, 2013.

G. M. Hwang, L. Pang, E. H. Mullen, et Y. Fainman, “Plasmonic sensing of biological analytes through nanoholes”, *IEEE sensors journal*, vol. 8, no. 12, pp. 2074–2079, 2008.

H. Im, A. Lesuffleur, N. C. Lindquist, et S.-H. Oh, “Plasmonic nanoholes in a multichannel microarray format for parallel kinetic assays and differential sensing”, *Analytical chemistry*, vol. 81, no. 8, pp. 2854–2859, 2009.

H. Im, S. H. Lee, N. J. Wittenberg, T. W. Johnson, N. C. Lindquist, P. Nagpal, D. J. Norris, et S.-H. Oh, “Template-stripped smooth ag nanohole arrays with silica shells for surface plasmon resonance biosensing”, *ACS nano*, vol. 5, no. 8, pp. 6244–6253, 2011.

H. Im, H. Shao, Y. I. Park, V. M. Peterson, C. M. Castro, R. Weissleder, et H. Lee, “Label-free detection and molecular profiling of exosomes with a nano-plasmonic sensor”, *Nature biotechnology*, vol. 32, no. 5, p. 490, 2014.

J. Ji, J. G. O’Connell, D. J. Carter, et D. N. Larson, “High-throughput nanohole array based system to monitor multiple binding events in real time”, *Analytical chemistry*, vol. 80, no. 7, pp. 2491–2498, 2008.

P. Jia, H. Jiang, J. Sabarinathan, et J. Yang, “Plasmonic nanohole array sensors fabricated by template transfer with improved optical performance”, *Nanotechnology*, vol. 24, no. 19, p. 195501, 2013.

P. B. Johnson et R.-W. Christy, “Optical constants of the noble metals”, *Physical review B*, vol. 6, no. 12, p. 4370, 1972.

K. K. Koerkamp, S. Enoch, F. Segerink, N. Van Hulst, et L. Kuipers, “Strong influence of hole shape on extraordinary transmission through periodic arrays of subwavelength holes”, *Physical Review Letters*, vol. 92, no. 18, p. 183901, 2004.

H. Ku et L. Scala, “Polymeric electron beam resists”, *Journal of The Electrochemical Society*, vol. 116, no. 7, pp. 980–985, 1969.

Y. Kurokawa et H. T. Miyazaki, “Metal-insulator-metal plasmon nanocavities : Analysis of optical properties”, *Physical Review B*, vol. 75, no. 3, p. 035411, 2007.

E.-S. Kwak, J. Henzie, S.-H. Chang, S. K. Gray, G. C. Schatz, et T. W. Odom, “Surface plasmon standing waves in large-area subwavelength hole arrays”, *Nano Letters*, vol. 5, no. 10, pp. 1963–1967, 2005.

P. Lalanne, C. Sauvan, J. Hugonin, J. Rodier, et P. Chavel, “Perturbative approach for surface plasmon effects on flat interfaces periodically corrugated by subwavelength apertures”, *Physical Review B*, vol. 68, no. 12, p. 125404, 2003.

P. Lalanne, J. Hugonin, et J. Rodier, “Theory of surface plasmon generation at nanoslit apertures”, *Physical review letters*, vol. 95, no. 26, p. 263902, 2005.

P. Lalanne, J. Rodier, et J. Hugonin, “Surface plasmons of metallic surfaces perforated by nanohole arrays”, *Journal of Optics A : Pure and Applied Optics*, vol. 7, no. 8, p. 422, 2005.

E. Laux, C. Genet, et T. Ebbesen, “Enhanced optical transmission at the cutoff transition”, *Optics express*, vol. 17, no. 9, pp. 6920–6930, 2009.

K.-L. Lee et P.-K. Wei, “Enhancing surface plasmon detection using ultrasmall nanoslits and a multispectral integration method”, *Small*, vol. 6, no. 17, pp. 1900–1907, 2010.

K.-L. Lee, S.-H. Wu, et P.-K. Wei, “Intensity sensitivity of gold nanostructures and its application for high-throughput biosensing”, *Optics express*, vol. 17, no. 25, pp. 23 104–23 113, 2009.

K.-L. Lee, P.-W. Chen, S.-H. Wu, J.-B. Huang, S.-Y. Yang, et P.-K. Wei, “Enhancing surface plasmon detection using template-stripped gold nanoslit arrays on plastic films”, *Acs Nano*, vol. 6, no. 4, pp. 2931–2939, 2012.

A. Lesuffleur, H. Im, N. C. Lindquist, et S.-H. Oh, “Periodic nanohole arrays with shape-enhanced plasmon resonance as real-time biosensors”, *Applied Physics Letters*, vol. 90, no. 24, p. 243110, 2007.

A. Lesuffleur, H. Im, N. C. Lindquist, K. S. Lim, et S.-H. Oh, “Laser-illuminated nanohole arrays for multiplex plasmonic microarray sensing”, *Optics express*, vol. 16, no. 1, pp. 219–224, 2008.

X. Li, M. Soler, C. I. Özdemir, A. Belushkin, F. Yesilkoy, et H. Altug, “Plasmonic nanohole array biosensor for label-free and real-time analysis of live cell secretion”, *Lab on a Chip*, 2017.

L. Lin et A. Roberts, “Light transmission through nanostructured metallic films : coupling between surface waves and localized resonances”, *Optics express*, vol. 19, no. 3, pp. 2626–2633, 2011.

N. C. Lindquist, A. Lesuffleur, H. Im, et S.-H. Oh, “Sub-micron resolution surface plasmon resonance imaging enabled by nanohole arrays with surrounding bragg mirrors for enhanced sensitivity and isolation”, *Lab on a Chip*, vol. 9, no. 3, pp. 382–387, 2009.

H. Liu et P. Lalanne, “Microscopic theory of the extraordinary optical transmission”, *Nature*, vol. 452, no. 7188, pp. 728–731, 2008.

H. Lochbihler et R. A. Depine, “Properties of tm resonances on metallic slit gratings”, *Applied optics*, vol. 51, no. 11, pp. 1729–1741, 2012.

S. A. Maier, M. L. Brongersma, P. G. Kik, S. Meltzer, A. A. Requicha, et H. A. Atwater, “Plasmonics—a route to nanoscale optical devices”, *Advanced Materials*, vol. 13, no. 19, pp. 1501–1505, 2001.

V. Malyarchuk, F. Hua, N. H. Mack, V. T. Velasquez, J. O. White, R. G. Nuzzo, et J. A. Rogers, “High performance plasmonic crystal sensor formed by soft nanoimprint lithography”, *Optics Express*, vol. 13, no. 15, pp. 5669–5675, 2005.

V. R. Manfrinato, L. Zhang, D. Su, H. Duan, R. G. Hobbs, E. A. Stach, et K. K. Berggren, “Resolution limits of electron-beam lithography toward the atomic scale”, *Nano letters*, vol. 13, no. 4, pp. 1555–1558, 2013.

F. Marquier, J.-J. Greffet, S. Collin, F. Pardo, et J. Pelouard, “Resonant transmission through a metallic film due to coupled modes”, *Optics express*, vol. 13, no. 1, pp. 70–76, 2005.

L. Martín-Moreno et F. García-Vidal, “Minimal model for optical transmission through holey metal films”, *Journal of Physics : Condensed Matter*, vol. 20, no. 30, p. 304214, 2008.

L. Martin-Moreno, F. Garcia-Vidal, H. Lezec, K. Pellerin, T. Thio, J. Pendry, et T. Ebbesen, "Theory of extraordinary optical transmission through subwavelength hole arrays", *Physical review letters*, vol. 86, no. 6, p. 1114, 2001.

MicroChem, "Pmma data sheet", 2001. En ligne : `http://microchem.com/pdf/PMMA_Data_Sheet.pdf`

J. P. Monteiro, J. H. de Oliveira, E. Radovanovic, A. G. Brolo, et E. M. Girotto, "Microfluidic plasmonic biosensor for breast cancer antigen detection", *Plasmonics*, vol. 11, no. 1, pp. 45–51, 2016.

K. Okamoto, I. Niki, A. Shvartser, Y. Narukawa, T. Mukai, et A. Scherer, "Surface-plasmon-enhanced light emitters based on ingan quantum wells", *Nature materials*, vol. 3, no. 9, pp. 601–605, 2004.

R. F. Oulton, V. J. Sorger, D. Genov, D. Pile, et X. Zhang, "A hybrid plasmonic waveguide for subwavelength confinement and long-range propagation", *Nature Photonics*, vol. 2, no. 8, pp. 496–500, 2008.

Y. Pang, C. Genet, et T. Ebbesen, "Optical transmission through subwavelength slit apertures in metallic films", *Optics Communications*, vol. 280, no. 1, pp. 10–15, 2007.

J. Pendry, L. Martin-Moreno, et F. Garcia-Vidal, "Mimicking surface plasmons with structured surfaces", *Science*, vol. 305, no. 5685, pp. 847–848, 2004.

O. Piciu, M. Docter, M. van der Krogt, Y. Garini, I. Young, P. Sarro, et A. Bossche, "Fabrication and optical characterization of nano-hole arrays in gold and gold/palladium films on glass", *Proceedings of the Institution of Mechanical Engineers, Part N : Journal of Nanomaterials, Nanoengineering and Nanosystems*, vol. 221, no. 3, pp. 107–114, 2007.

M. Piliarik et J. Homola, "Spr sensor instrumentation", *Surface Plasmon Resonance Based Sensors*, pp. 95–116, 2006.

——, "Surface plasmon resonance (spr) sensors : approaching their limits ?" *Optics express*, vol. 17, no. 19, pp. 16 505–16 517, 2009.

F. Przybilla, A. Degiron, C. Genet, T. Ebbesen, F. de Léon-Pérez, J. Bravo-Abad, F. García-Vidal, et L. Martín-Moreno, "Efficiency and finite size effects in enhanced transmission through subwavelength apertures", *Optics express*, vol. 16, no. 13, pp. 9571–9579, 2008.

L. Rayleigh, “Iii. note on the remarkable case of diffraction spectra described by prof. wood”, *The London, Edinburgh, and Dublin Philosophical Magazine and Journal of Science*, vol. 14, no. 79, pp. 60–65, 1907.

J. Rheims, J. Köser, et T. Wriedt, “Refractive-index measurements in the near-ir using an abbe refractometer”, *Measurement Science and Technology*, vol. 8, no. 6, p. 601, 1997.

M. Rommel, B. Nilsson, P. Jedrasik, V. Bonanni, A. Dmitriev, et J. Weis, “Sub-10nm resolution after lift-off using hsq/pmma double layer resist”, *Microelectronic Engineering*, vol. 110, pp. 123–125, 2013.

J. A. Schuller, E. S. Barnard, W. Cai, Y. C. Jun, J. S. White, et M. L. Brongersma, “Plasmonics for extreme light concentration and manipulation”, *Nature materials*, vol. 9, no. 3, pp. 193–204, 2010.

S. T. Seiler, I. S. Rich, et N. C. Lindquist, “Direct spectral imaging of plasmonic nanohole arrays for real-time sensing”, *Nanotechnology*, vol. 27, no. 18, p. 184001, 2016.

J. C. Sharpe, J. S. Mitchell, L. Lin, N. Sedoglavich, et R. J. Blaikie, “Gold nanohole array substrates as immunobiosensors”, *Analytical chemistry*, vol. 80, no. 6, pp. 2244–2249, 2008.

J.-T. Shen, P. B. Catrysse, et S. Fan, “Mechanism for designing metallic metamaterials with a high index of refraction”, *Physical review letters*, vol. 94, no. 19, p. 197401, 2005.

D. Sinton, R. Gordon, et A. G. Brolo, “Nanohole arrays in metal films as optofluidic elements : progress and potential”, *Microfluidics and Nanofluidics*, vol. 4, no. 1, pp. 107–116, 2008.

J. L. Skinner, L. L. Hunter, A. A. Talin, J. Provine, et D. A. Horsley, “Large-area subwavelength aperture arrays fabricated using nanoimprint lithography”, *IEEE Transactions on Nanotechnology*, vol. 7, no. 5, pp. 527–531, 2008.

M. Soler, A. Belushkin, A. Cavallini, C. Kebbi-Beghdadi, G. Greub, et H. Altug, “Multiplexed nanoplasmonic biosensor for one-step simultaneous detection of chlamydia trachomatis and neisseria gonorrhoeae in urine”, *Biosensors and Bioelectronics*, vol. 94, pp. 560–567, 2017.

W. Teh, C.-T. Liang, M. Graham, et C. G. Smith, “Cross-linked pmma as a low-dimensional dielectric sacrificial layer”, *Journal of microelectromechanical systems*, vol. 12, no. 5, pp. 641–648, 2003.

G. A. C. Tellez, R. N. Tait, P. Berini, R. Gordon *et al.*, "Atomically flat symmetric elliptical nanohole arrays in a gold film for ultrasensitive refractive index sensing", *Lab on a Chip*, vol. 13, no. 13, pp. 2541–2546, 2013.

K. A. Tetz, L. Pang, et Y. Fainman, "High-resolution surface plasmon resonance sensor based on linewidth-optimized nanohole array transmittance", *Optics Letters*, vol. 31, no. 10, pp. 1528–1530, 2006.

I. Utke, P. Hoffmann, et J. Melngailis, "Gas-assisted focused electron beam and ion beam processing and fabrication", *Journal of Vacuum Science & Technology B : Microelectronics and Nanometer Structures Processing, Measurement, and Phenomena*, vol. 26, no. 4, pp. 1197–1276, 2008.

F. C. van Delft, J. P. Weterings, A. K. van Langen-Suurling, et H. Romijn, "Hydrogen silsesquioxane/novolak bilayer resist for high aspect ratio nanoscale electron-beam lithography", *Journal of Vacuum Science & Technology B : Microelectronics and Nanometer Structures Processing, Measurement, and Phenomena*, vol. 18, no. 6, pp. 3419–3423, 2000.

C. Vieu, F. Carcenac, A. Pepin, Y. Chen, M. Mejias, A. Lebib, L. Manin-Ferlazzo, L. Couraud, et H. Launois, "Electron beam lithography : resolution limits and applications", *Applied Surface Science*, vol. 164, no. 1, pp. 111–117, 2000.

Y. Wang, A. Kar, A. Paterson, K. Kourentzi, H. Le, P. Ruchhoeft, R. Willson, et J. Bao, "Transmissive nanohole arrays for massively-parallel optical biosensing", *ACS photonics*, vol. 1, no. 3, pp. 241–245, 2014.

K. A. Willets et R. P. Van Duyne, "Localized surface plasmon resonance spectroscopy and sensing", *Annu. Rev. Phys. Chem*, vol. 58, pp. 267–97, 2007.

N. J. Wittenberg, H. Im, X. Xu, B. Wootla, J. Watzlawik, A. E. Warrington, M. Rodriguez, et S.-H. Oh, "High-affinity binding of remyelinating natural autoantibodies to myelin-mimicking lipid bilayers revealed by nanohole surface plasmon resonance", *Analytical chemistry*, vol. 84, no. 14, pp. 6031–6039, 2012.

R. W. Wood, "Xlii. on a remarkable case of uneven distribution of light in a diffraction grating spectrum", *The London, Edinburgh, and Dublin Philosophical Magazine and Journal of Science*, vol. 4, no. 21, pp. 396–402, 1902.

J. B. Wright, K. N. Cicotte, G. Subramania, S. M. Dirk, et I. Brener, "Chemoselective gas sensors based on plasmonic nanohole arrays", *Optical Materials Express*, vol. 2, no. 11, pp.

1655–1662, 2012.

W. Wu, D. Dey, O. G. Memis, A. Katsnelson, et H. Mohseni, “Fabrication of large area periodic nanostructures using nanosphere photolithography”, *Nanoscale Research Letters*, vol. 3, no. 10, p. 351, 2008.

Y. Xie, A. R. Zakharian, J. V. Moloney, et M. Mansuripur, “Transmission of light through a periodic array of slits in a thick metallic film”, *Optics Express*, vol. 13, no. 12, pp. 4485–4491, 2005.

H. Yang, A. Jin, Q. Luo, J. Li, C. Gu, et Z. Cui, “Electron beam lithography of hsq/pmma bilayer resists for negative tone lift-off process”, *Microelectronic Engineering*, vol. 85, no. 5, pp. 814–817, 2008.

J. Yang, H. Giessen, et P. Lalanne, “Simple analytical expression for the peak-frequency shifts of plasmonic resonances for sensing”, *Nano letters*, vol. 15, no. 5, pp. 3439–3444, 2015.

J.-C. Yang, J. Ji, J. M. Hogle, et D. N. Larson, “Metallic nanohole arrays on fluoropolymer substrates as small label-free real-time bioprobes”, *Nano letters*, vol. 8, no. 9, pp. 2718–2724, 2008.

——, “Multiplexed plasmonic sensing based on small-dimension nanohole arrays and intensity interrogation”, *Biosensors and Bioelectronics*, vol. 24, no. 8, pp. 2334–2338, 2009.

A. A. Yanik, M. Huang, A. Artar, T.-Y. Chang, et H. Altug, “Integrated nanoplasmonic-nanofluidic biosensors with targeted delivery of analytes”, *Applied physics letters*, vol. 96, no. 2, p. 021101, 2010.

J. W. Yoon, J. H. Lee, S. H. Song, et R. Magnusson, “Unified theory of surface-plasmonic enhancement and extinction of light transmission through metallic nanoslit arrays”, *Scientific reports*, vol. 4, 2014.

I. Zailer, J. Frost, V. Chabasseur-Molyneux, C. Ford, et M. Pepper, “Crosslinked pmma as a high-resolution negative resist for electron beam lithography and applications for physics of low-dimensional structures”, *Semiconductor science and technology*, vol. 11, no. 8, p. 1235, 1996.

J. Zhang, M. Irannejad, M. Yavuz, et B. Cui, “Gold nanohole array with sub-1 nm roughness by annealing for sensitivity enhancement of extraordinary optical transmission biosensor”, *Nanoscale research letters*, vol. 10, no. 1, p. 1, 2015.

Z. J. Zhou, “Electron beam lithography”, *Handbook of Microscopy for Nanotechnology*, pp. 287–321, 2005.

ANNEXE A Guide Matlab CMT pour les réseaux de nano-indentations

Un guide Matlab a été conçu afin de modéliser la transmission et réflection ainsi que la distribution de champs électrique pour les structures considérées dans cette thèse. Il est publié sur internet sur le site de partage de publication multimédia *figshare* :

1-D Nanoslit and 2-D Squarehole periodic array optical properties - Coupled Mode Theory - Matlab GUI (Blanchard-Dionne, 2017a)

https ://doi.org/10.6084/m9.figshare.5131519.v2

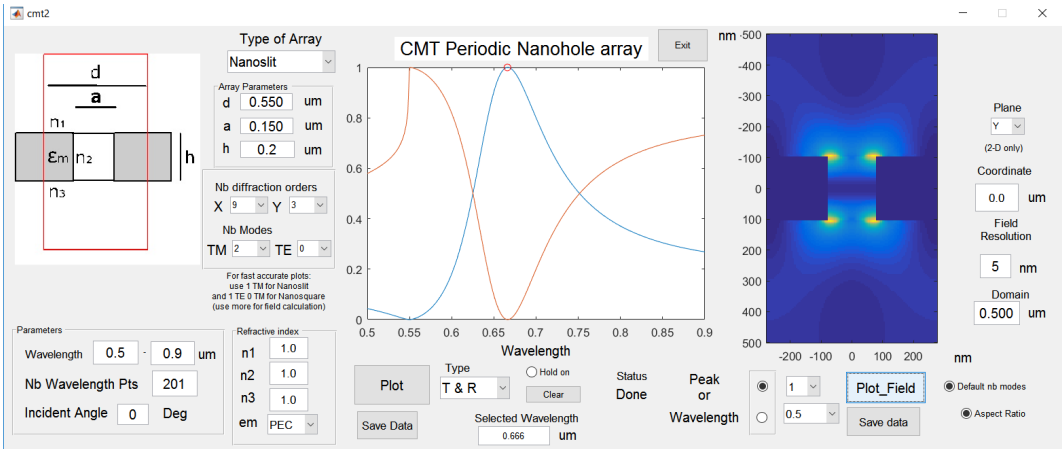


Figure A.1 Interface utilisateur Matlab pour obtenir les spectres de transmission et de réflexion de réseaux de nanotrous périodiquespour nimporte quelle dimension et indice de réfraction pour la structure. La distribution de champ électrique est aussi incluse

La GUI Matlab peut aussi être télécharger en application automnome (sans le logiciel Matlab), mais il sera accompagné de l'installation du Runtime Matlab :

1-D Nanoslit and 2-D Squarehole periodic array optical properties - Coupled Mode Theory - Standalone application (Blanchard-Dionne, 2017b)

https ://doi.org/10.6084/m9.figshare.5131564.v2

ANNEXE B Code Matlab pour les structures 1-D Nanoslit Metal-Insulator-Metal

Un code Matlab est disponible pour les propriétés optique des Nanostructures périodiques 1-D sur Metal-Insulator-Metal

MIM Periodic 1-D Slit Nanostructures - Couped Mode Theory (Blanchard-Dionne, 2017c)

https ://doi.org/10.6084/m9.figshare.5131576.v1

ANNEXE C Publications et Conférence

1. **A-P. Blanchard-Dionne** and M. Meunier, *Multiperiodic Nanohole Array For High Precision Multiplexed Sensing*, submitted to ACS Photonics. Manuscript available at : `https://www.dropbox.com/s/a48apkby7iizmpw/achemso-demo.pdf?dl=0`
2. **A-P. Blanchard-Dionne** and M. Meunier, *Sensing With Periodic Nanohole Arrays*, *Invited Paper* for Advances in Optics and Photonics, *Under Review*. manuscript available at : `https://www.dropbox.com/s/s8e19urojz8kd7w/OSA-journal-template.pdf?dl=0`
3. A. Attiaoui, S. Wirth, **A-P. Blanchard-Dionne**, M. Meunier, J.M. Hartmann, D. Buca and O. Moutanabir, *Enhanced IR Light Absorption in Group IV-SiGeSn Core-Shell Nanowires*, arXiv preprint, Vol 19, No 16, 15041-15046.
4. **A-P. Blanchard-Dionne** and M. Meunier, *Optical transmission theory for metal-insulator-metal periodic nanostructures*, Nanophotonics, Vol 6, No 1, 349-355.
5. C. Boutopoulos, A. Dagallier, M. Sansone, **A-P. Blanchard-Dionne**, É. Lecavalier-Hustibise, É. Boulais and M. Meunier, *Photon-induced generation and spatial control of extreme pressure at the nanoscale with a gold bowtie nano-antenna platform*, Nanoscale, 2016, Vol 8, No 39, 17196-17203.
6. S. Patskovsky, A.-M. Dallaire, **A-P. Blanchard-Dionne**, A. Vallée-Bélisle and M. Meunier, *Electrochemical structure-switching sensing using nanoplasmonic devices*, Annalen der Physik, 2015, Vol 527, No 11-12, 806-813.
7. **A-P. Blanchard-Dionne** and M. Meunier, *Electron beam lithography using a PMMA/P (MMA 8.5 MAA) bilayer for negative tone lift-off process*, Journal of Vaccuum, Vol 6, No 1, 349-355.
8. **A.-P. Blanchard-Dionne**, L. Guyot, S. Patskovsky, R. Gordon and M. Meunier, *Intensity based surface plasmon resonance sensor using a nanohole rectangular array*, Optics Express, 2011, Vol 19, No 16, 15041-15046.
9. L. Guyot, **A.-P. Blanchard-Dionne**, S. Patskovsky and M. Meunier, *Integrated silicon-based nanoplasmonic sensor*, Optics Express, 2011, Vol 19, No 10, 9962-9967.
10. M. Maisonneuve, O. d'Allivy Kelly, **A-P. Blanchard-Dionne**, S. Patskovsky and M. Meunier, *Phase sensitive sensor on plasmonic nanograting structures*, Optics Express, 2011, Vol 19, No 17, 26318-26324
11. S. Patskovsky, **A-P Blanchard-Dionne**, N. Rousset and M. Meunier, *Double peak nanoplasmonic sensor for multiple biosensing*, NSTI-Nanotech, 2011, Vol 3, 83-85

Conferences :

1. **A.-P. Blanchard-Dionne**, M. Meunier, *Theoretical Guide For Sensing with 1-D and 2-D Nanohole Array : Sensitivity, Resolution and Field Distribution*, Surface Plasmon Photonics 8, 2017
2. **A.-P. Blanchard-Dionne**, M. Maisonneuve, M. Meunier, *Polarization modulation for multiplexed biosensing using nanohole rectangular arrays on free standing Film*, Surface Plasmon Photonics 6, 2013
3. **A.-P. Blanchard-Dionne**, M. Maisonneuve, A. Bouchard-Saindon, M. Meunier, *Flow-through Nanohole array sensor*, Photonics North, 2012
4. **A.-P. Blanchard-Dionne**, Laurent Guyot, In-Hyouk Song, Sergiy Paskovsky, Michel Meunier *Propriétés optiques de nanostructures plasmoniques et application comme biocapteurs*, Colloque Optique guidée et photonique IX, ACFAS 2010

Online Modelling Tools

1. **A.-P. Blanchard-Dionne**, *MIM Periodic 1-D Slit Nanostructures - Couped Mode Theory*, `https://doi.org/10.6084/m9.figshare.5131576.v1`, 2017
2. **A.-P. Blanchard-Dionne**, *1-D Nanoslit and 2-D Squarehole periodic array optical properties - Coupled Mode Theory - Standalone application*, `https://doi.org/10.6084/m9.figshare.5131564.v2`, 2017
3. **A.-P. Blanchard-Dionne**, *1-D Nanoslit and 2-D Squarehole periodic array optical properties - Coupled Mode Theory - Matab GUI*, `https://doi.org/10.6084/m9.figshare.5131519.v2`, 2017

ANNEXE D Performances des capteurs

Cet annexe a pour but de clarifier les notions utilisées dans la littérature ainsi que dans cette thèse au sujet des notions de performances des capteurs basé sur un changement d'indice de réfraction (RIU). En effet, des précisions doivent être amenées afin d'évaluer les performances des capteurs sur une base commune. Tout d'abord, la sensibilité d'un capteur est son taux de variation du changement de la position de résonance en fonction du changement d'indice de réfraction.

$$S = \frac{d\lambda}{dn} \tag{D.1}$$

Dans cette analyse de la performance du capteur, nous supposons que le signal de détection est donné par la position du maximum de la résonance. Nous pouvons ainsi introduire la notion de résolution, qui sera relative au plus petit changement de la position spectrale du maximum qui peut être détectée. La performance du capteur est donc donnée par la limite de détection, définie par :

$$LD = R/S \tag{D.2}$$

ou LD signifie la limite de détection, R est la résolution du système, et S la sensibilité. La résolution dépend à la fois de la capacité du système de déterminer la métrique de détection, dans ce cas si la position spectrale, et du niveau de bruit du système.Elle est déterminée expérimentalement. La résolution spectrale dépend à la fois de la précision des appareils de mesure et du facteur de qualité de la résonance. Le bruit de détection est relatif au shot-noise de la caméra, au bruit de la source ainsi qu'au bruit électronique du système. On peut aussi inclure le bruit de stabilité thermique du système, qui fait varier la position spectrale et donc réduit la précision. Tout ces facteurs